Nuclear Probes for Materials
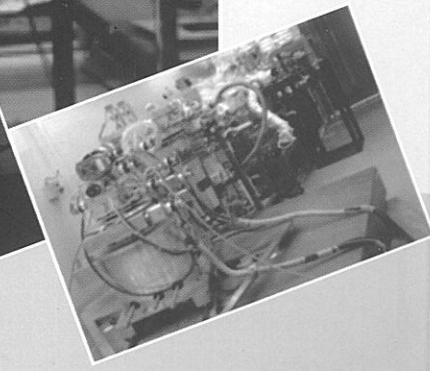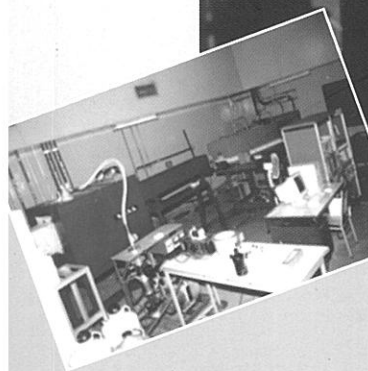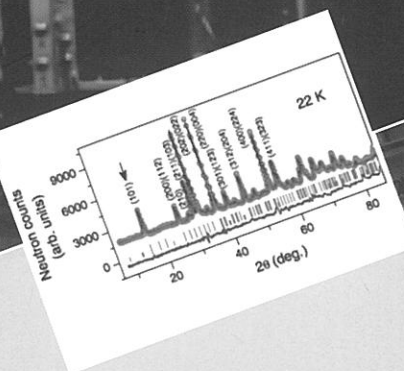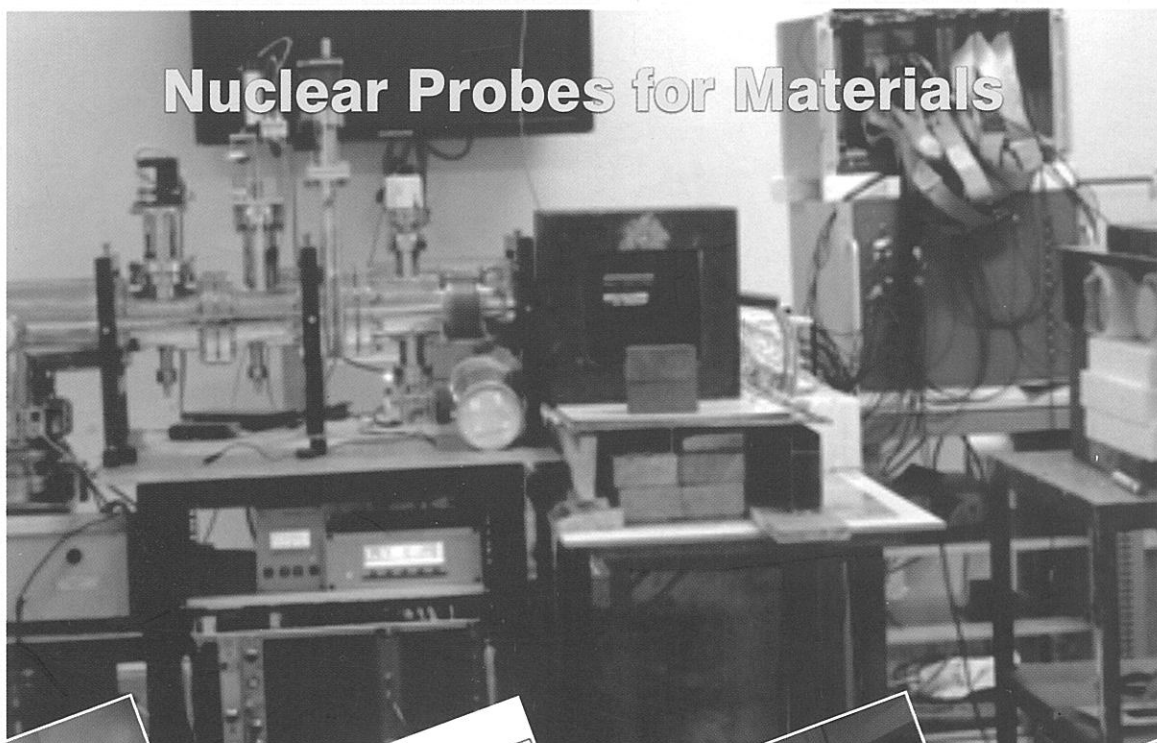
Editorial

Elegant techniques, based on the use of nuclear particles and ionising radiation as probes, have been extensively investigated and deployed for materials characterisation and development. The range comprises relatively simpler techniques of neutron activation analysis (NAA) and X-ray fluorescence (XRF) at one end, to advanced approaches of positron annihilation spectroscopy (PAS) and Extended X-ray Absorption Fine Structure (EXAFS) at the other end. The Department of Atomic Energy through its various Units, such as, BARC, IGCAR, RRCAT, and others, has made pioneering efforts across the above entire range receiving global recognition. In view of this, the Editorial Team of IANCAS desired the preparation of a thematic Bulletin to capture typical cases of success stories of deployment of such probes and probing techniques. Dr. P.K. Pujari, Radiochemistry Division, BARC, accepted to take on the task and the resultant product is in your hands now. The initial emphasis on success story first, the technique per se be the next, could not be entirely accomplished, but that hardly matters.

The use of X-rays and neutrons as 'intrusive probes' has been a long-standing tradition at DAE laboratories, while the more extensive use of positron-based techniques has been a later development. The research reactors at Trombay have been the nucleus for a large quantum of R&D endeavours (by both DAE teams and researchers from non-DAE centres) based on neutron beam facilities and allied systems. A visit to the Dhruva reactor hall on any day will show the variety of researchers' equipment installed and operated there. In parallel, the emergence of synchrotron radiation based facilities at RRCAT has synergistically strengthened the scope for development and practice of other sophisticated techniques making use of the wide range of energy and intensity of X-rays. Taken together, these probing techniques support far greater understanding of materials at both macroscopic and microscopic scales, as well as aid the development of advanced materials. The Bulletin covers some of the efforts and achievements on magnetic materials, bio- and nano- materials, all of which form a group of innovative materials attracting much attention for applications in diverse fields of technological and societal importance.

Accordingly, the current issue contains two articles that underpin the versatility and high utility of SANS in developing materials of technological importance and potential applications. The articles on X-ray absorption spectroscopy (EXAFS) using the Indus facility at RRCAT and on positron annihilation spectroscopy (PAS) show the might of these complementary probes. The successful demonstration by a team of researchers of BARC, using

CONTENTS

Probing Structure and Interaction of Bio- and Nano-Materials by Small-Angle Neutron Scattering

V.K. Aswal

Solid State Physics Division, Bhabha Atomic Research Centre, Mumbai 400 085; E-mail: vkaswal@barc.gov.in

Abstract

Bio- and nano-materials possess a specific shape and charge, which regulate and control their functionality and stability. The particles (biomolecules and/or nanoparticles) in aqueous solution are known to interact through different interaction forces. Different phases in any of these systems are preceded and followed by structural changes among them, which can be induced simply by varying temperature or neutralizing the charge on the particle by salt or breaking the water structure by urea. We have used small-angle neutron scattering (SANS) technique for studying the evolution of structure and interaction in different phases of biological and nanomaterial systems.

Introduction

Small-angle neutron scattering (SANS) is a powerful technique in the study of biological and nanostructured systems as for most of these systems their 3D structure have a length scale in the range 1 - 100 nm [1]. The major advantage of the method lies in its ability to provide structural information about partially or completely disordered systems. SANS allows to study the structure of native particles in near physiological environments and to analyze structural changes in response to variations in external conditions. Both structure as well as interaction in these systems can be determined by SANS [2]. The applications cover extensive studies of different types of biomolecules (e.g. proteins, lipids, nucleic acids, macromolecular complexes and polyelectrolytes) and nanomaterials (e.g. nanoparticles, fullerenes, dendrimers and composites) as well as their conjugates. The contrast variation SANS either by deuterating the particle or solvent is widely used in such multi-constituents systems. This article presents some of our recent results.

SANS is elastic scattering experiment involving scattering of a monochromatic beam of neutrons from the sample and measuring the scattered neutron intensity as a function of the scattering angle. The magnitude of wave vector transfer Q ($= 4\pi\sin\theta/\lambda$, where λ is the incident neutron wavelength and 2θ is the scattering angle) in these experiments is small, typically in the range of 10^{-2} to 1.0 Å^{-1}. The wavelength of neutrons used for these experiments usually being $4 - 10$ Å. An indigenously built SANS instrument [3] has been operating at Dhruva reactor, BARC (Fig. 1), and is being regularly used for in-house research and by many university researchers.

In SANS experiment one measures the coherent differential scattering cross-section ($d\Sigma/d\Omega$) as a function of Q. For a system of particles, it is given by [4]

$$\frac{d\Sigma}{d\Omega}(Q) = n(\rho_p - \rho_s)^2 \, V^2 P(Q)S(Q) \qquad (1)$$

where n is the number density of the particles, ρ_p and ρ_s are, respectively, the scattering length densities of the particle and the solvent, and V is the volume of the particle. $P(Q)$ is the intraparticle structure factor and is decided by the shape and size of the particle. $S(Q)$ is the interparticle structure factor, which depends on the spatial arrangement of particles and is thereby sensitive to interparticle interactions. In case of dilute solutions, interparticle interference effects are negligible, and $S(Q) \sim 1$. The typical plots of $P(Q)$ and $S(Q)$ are given in Fig. 2a.

Fig. 1a A photograph of the SANS facility at Dhruva reactor, BARC
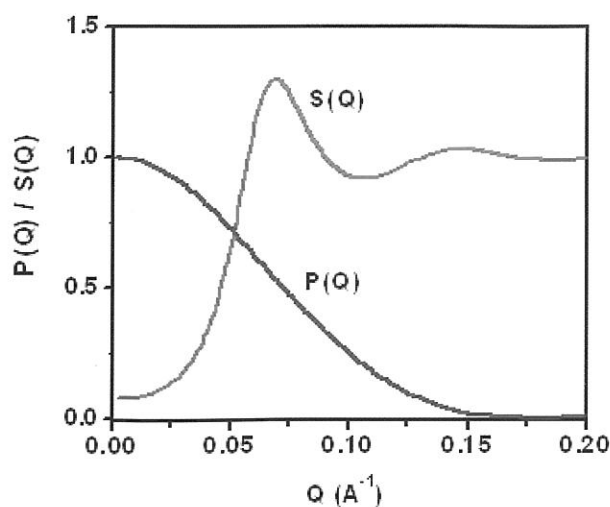
SANS Instrument at BARC
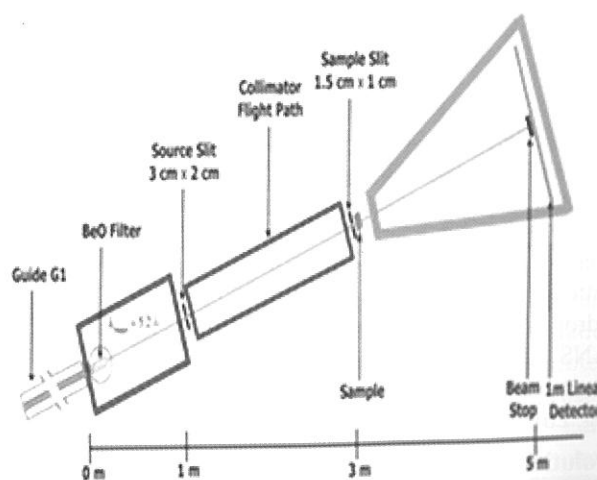
Fig. 1b A layout of the SANS facility at Dhruva reactor, BARC

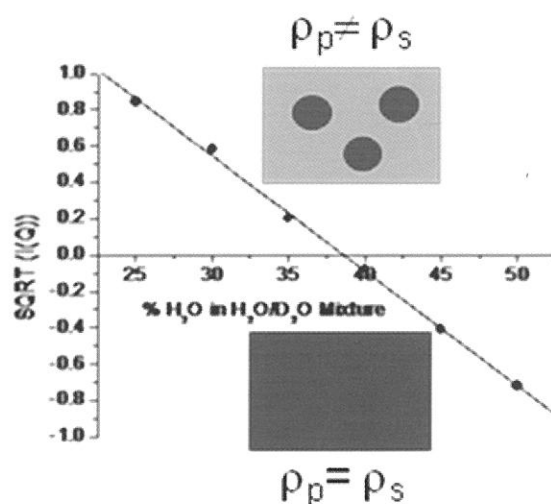*Fig. 2a Typical P(Q) and S(Q) curves in SANS data.*

Fig. 2b Contrast variation technique in SANS to make system components visible or invisible.

Scattered neutron intensity in the SANS experiment depends on $(\rho_p - \rho_s)^2$ - the square of the difference between the average scattering length density of the particle and the average scattering length density of the solvent. This term is referred to as contrast factor. Due to the fact that the scattering length is negative (= - 0.3723×10^{-12} cm) for hydrogen and positive (= 0.6674×10^{-12} cm) for deuterium, SANS is an ideal technique for studying the structural aspects of hydrogenous materials such as biological systems (Fig. 2b).

Evolution of Structure and Interaction in Protein Solutions

Proteins are macromolecules made of amino acids perform structural, transport, catalytic, sensory and many other important biological functions. In solutions, they are known to exhibit rich phase behavior. It is believed that many of these phases of protein solutions can be explained by the interaction combining short-range attraction along with the long-range repulsion [5]. The tuning of these two
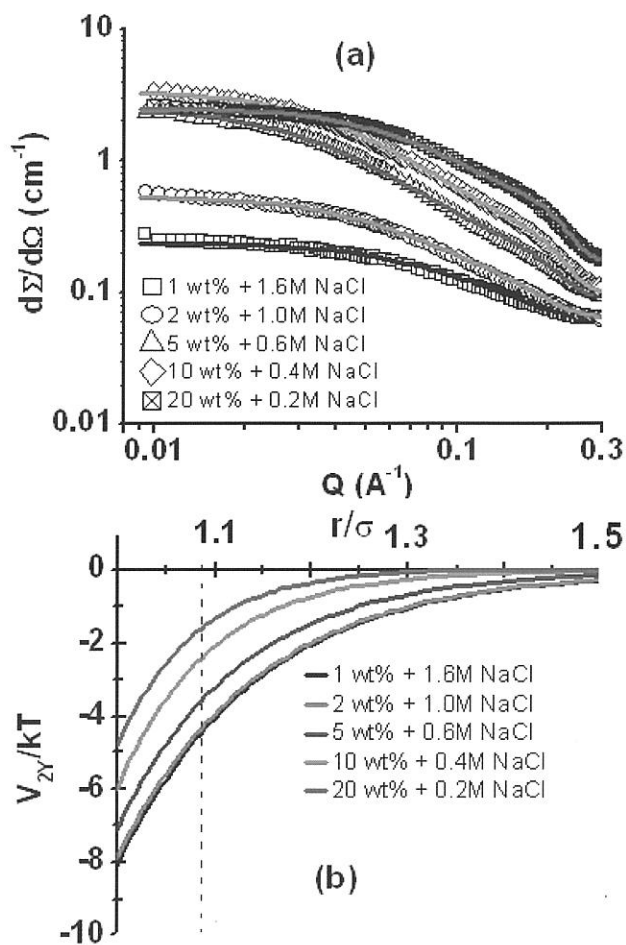

Fig. 3 The correlation of (a) SANS data and (b) total potential for different protein concentrations in presence of salt on approaching LLPT.

interaction components can lead to different phase transitions including liquid-liquid phase transition (LLPT). In LLPT, the protein solution gets divided into two phases one rich in protein while the other protein deficient. The liquid-liquid phase is one of the important phases that can enhance solid phase such as crystallization. The LLPT in aqueous salt solutions of lysozyme protein has been studied by SANS (Fig. 3a). Measurements were carried out on fixed protein concentration with varying salt concentration approaching LLPT [6]. The data are fitted considering protein interaction by two Yukawa (2Y) potential which combines short-range attraction and long-range repulsion. We showed that LLPT arises because of enhancement of non-DLVO short-range attraction without any conformational structural change of the protein. This attractive interaction is believed to be arising from entropy driven dehydration induced by the hydrated salt ions. The salt concentration required for LLPT as well as corresponding short-range attraction decrease significantly with increase in protein concentration (Fig. 3b).

Proteins function depends absolutely on its three-dimensional folded structure. Proteins can undergo
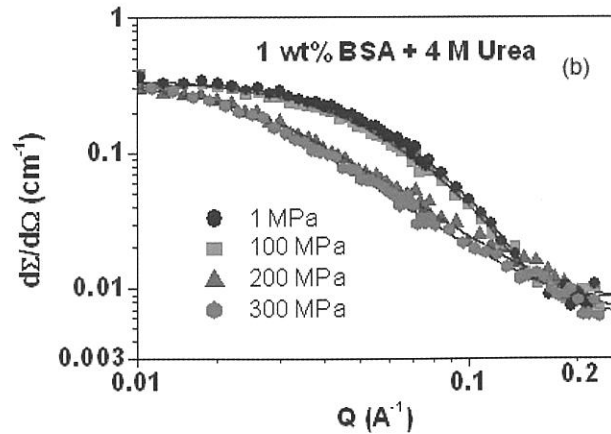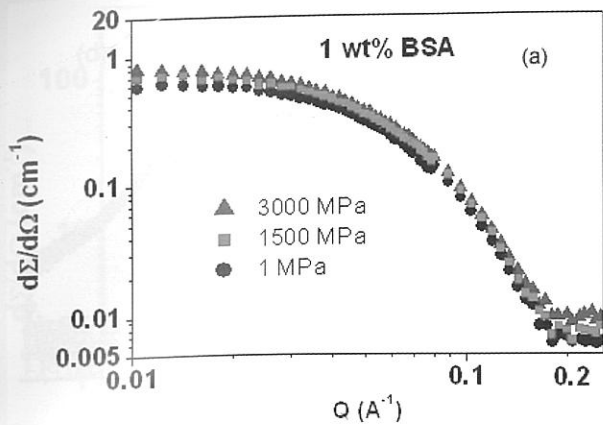
Fig. 4 SANS data (a) 1 wt% BSA and (b)1 wt% BSA + 4 M Urea as a function of pressure
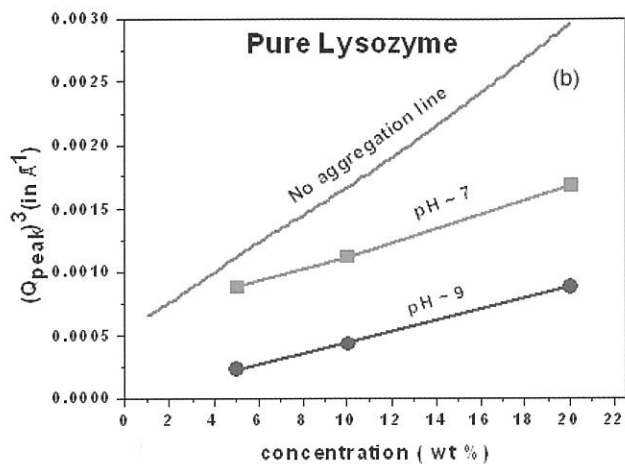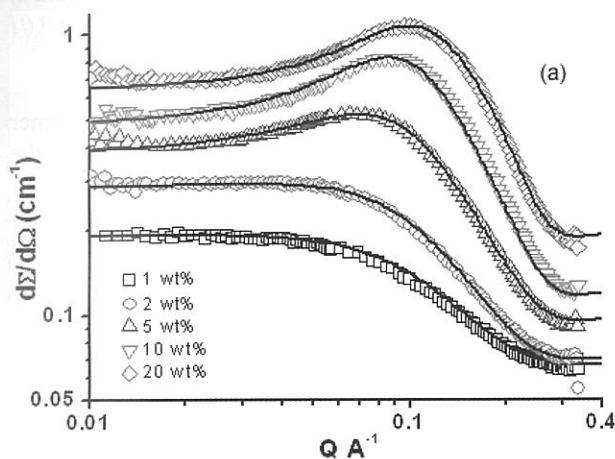

Fig. 5 (a) SANS data with varying protein concentrations at pH 7. (b) Comparison of expected and experimental values of peak positions $(Q_p)^3$ with protein concentration.

unfolding/refolding transitions in presence of denaturants such as urea, surfactant and pressure. Protein unfolding process involves the disruption of H-bonds, disulphide bonds, salt bridges and hydrophobic interactions, leading to its successive alteration of quaternary, tertiary, and secondary structure [7]. We have used SANS to study protein unfolding and refolding if any in protein bovine serum albumin (BSA) due to perturbation in its native structure as induced by different protein denaturing agents [8]. BSA protein unfolds for urea concentrations greater than 4 M and is observed to be independent of protein concentration. The addition of surfactant unfolds the protein by the formation of micelle-like clusters of surfactants along the unfolded polypeptide chains of the protein and depends on the ratio of surfactant to protein concentration. We used the dilution method to show the refolding of unfolded protein in presence of urea and surfactant. BSA does not show any protein unfolding up to the pressure of 450 MPa. The presence of urea and surfactant (for concentrations prior to inducing their own unfolding) has been used to examine pressure-induced unfolding of the protein at lower pressure. The protein unfolds at 200 MPa pressure in presence of urea, however no unfolding is observed with surfactant (Fig. 4).

The protein unfolding is shown to be reversible in all these denaturating methods.

Recently, the existence of protein clusters has been reported in concentrated lysozyme protein solutions [9]. SANS data in these systems did not show any change in the correlation peak and were interpreted that all the monomers undergo to form clusters whose aggregation number increases with protein concentration. However, later SANS experiments have contradicted to the presence of any clusters in these systems [10]. In this case the correlation peak shifts to higher Q values with increase in protein concentration as expected for the repulsive protein monomers in the system. Further, recent Spin Echo measurements have suggested the existence of dynamic clusters with monomers [11]. Our SANS measurements showed the co-existence of monomers with large clusters as a function of protein concentration and pH [12]. Fig. 5a shows the SANS data for 1, 2, 5, 10 and 20 wt% lysozyme protein solution at pH 7. The overall increase in intensity with protein concentration is a result of increase in number density of protein molecules. The shift in peak position towards high Q region with protein concentration indicates decrease in the average distance between the protein
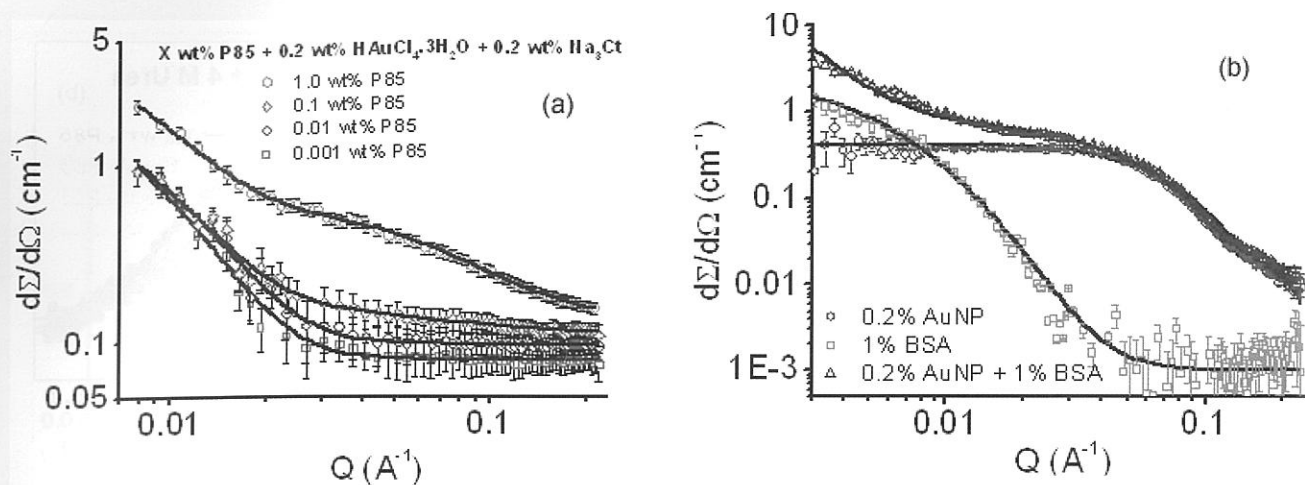
Fig. 6   (a) SANS data of varying P85 concentration for 0.2 wt% $HAuCl_4.3H_2O$ with 0.2 wt% Na_3Ct at 15^oC. (b) SANS data of gold nanoparticles and BSA and their conjugates. The gold nanoparticles in all these studies are prepared using 0.01 wt% P85 + 0.2 wt% $HAuCl_4.3H_2O$ + 0.2 wt% Na_3Ct system. The pH for BSA in all the samples is kept at 7.

molecules. The correlation peak (Q_p) in SANS arises because of the peak in S(Q) and it occurs at $Q_p \sim 2\pi/d$, where d is the distance between the protein molecules. The variation of correlation peak $(Q_p)^3$ as a function of protein concentration is plotted in Fig. 5b. The figure also show the variation of Q_p (α $C^{1/3}$) when no particle aggregation is considered over the whole concentration range. It is clear that Q_p dependence is very different for measured data at pH 7 and 9 than the case of no aggregation. The values of Q_p are found to be significantly smaller than that of no aggregation. The decrease in the values of Q_p at a given concentration suggests the decrease in the number density of monomers coexisting with clusters. The difference of Q_p from that of no aggregation increases with the increase in pH value relates to higher propensity of clustering as the net charge on the protein decreases approaching pI. Figure 5 also suggests that clustering is favored at higher proteins concentrations. These clusters are believed to much larger than those expected from the equilibrium clusters as no significant scattering from them in the Q range of measurement is observed.

Synthesis and Characterization of Nanoparticles

An economical, environmentally benign and fast synthesis methodology for gold nanoparticles using block copolymer has been developed [13]. In this synthesis, block copolymer plays the dual role of reducing agent as well as stabilizing agent. The formation of gold nanoparticles comprises three main steps, reduction of $AuCl_4^-$ by the block copolymers in the solution and formation of gold clusters, adsorption of block copolymers on gold clusters and reduction of $AuCl_4^-$ ions on the surfaces of these gold clusters for the growth of gold particles in steps and finally its stabilization by block copolymers. The control over these three different steps decides the output of the synthesis of gold nanoparticles. We have looked into the role of different components and optimization of concentrations to enhance the yield of the synthesis. This method usually has a very limited yield which does not simply increase with the increase in the gold salt concentration. We showed that the

yield can be enhanced by increasing the block copolymer concentration but is limited to the factor by which the concentration is increased [14]. On the other hand, the presence of an additional reductant (trisodium citrate) in 1:1 molar ratio with gold salt enhances the yield by manyfold (Fig. 6a). In this case (with additional reductant), the stable and high-yield nanoparticles having size about 14 nm can be synthesized at very low block copolymer concentrations. These nanoparticles thus can be efficiently used for their application such as for adsorption of proteins (Fig. 6b).

Nanoparticle dispersions are known to show rich phase behavior and find numerous applications. Many of these phases can be explained by DLVO theory governed by the competition of short-range van der Waals attraction and a long-range electrostatic repulsion among the particles [15]. However, there are numerous cases where DLVO theory fails and non-DLVO contributions (e.g. hydration and depletion interactions etc.) are required to explain the system behavior. The depletion force arises in a system consisting of two significantly different sizes of structures (e.g. nanoparticles, micelles, polymers) due to the exclusion of a non-adsorbed smaller structure from the gap region between larger structures. The resulting concentration difference produces an osmotic pressure imbalance between the gap and bulk, resulting in a net attractive force. The depletion interaction has been mostly considered as short-range attraction and found applicable to the systems which are sterically stabilized as hard sphere potential as repulsive part. SANS has been carried out to examine block copolymer induced depletion interaction of charged silica nanoparticles in aqueous solution (Fig. 7a) [16]. The measurements were performed on anionic Ludox silica nanoparticles in the presence of 0.1 M NaCl and varying concentration of polyethylene oxide-polypropylene oxide-polyethylene oxide (PEO-PPO-PEO) P85 $[(EO)_{26}(PO)_{39}(EO)_{26}]$ block copolymer. The depletion interaction is found to be long-range attraction whose magnitude and range increase with block copolymer concentration (Fig. 7b). The depletion
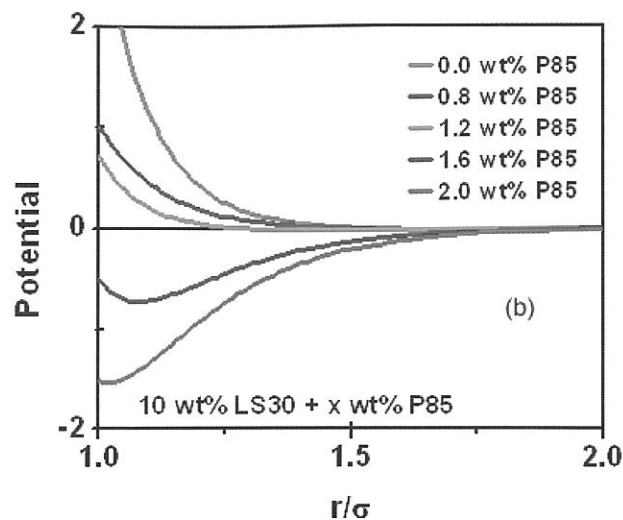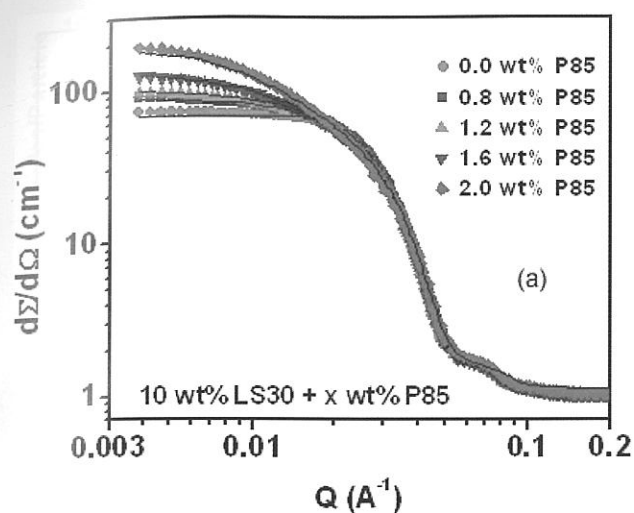
Fig. 7   (a) SANS data of 10 wt% LS30 silica nanoparticles with varying concentration of P85 block copolymer at 20 °C. Inset highlights the variation in low Q data. (b) Total interaction potential for 10 wt% LS30 silica nanoparticles with varying concentration of P85 block copolymer.

interaction is further enhanced by tuning the self-assembly of block copolymer through the variation of temperature. The increase of depletion interaction ultimately leads to clustering of nanoparticles and is confirmed by the presence of a Bragg peak in the SANS data. The positioning of Bragg peak suggests simple cubic type packing of particles within the clusters. The scattering from the clusters in the low Q region is governed by the Porod scattering indicating clusters are quite large (order of micron). The depletion interaction is also found to be strongly dependent on the size of the nanoparticles.

The charged nanoparticles in presence of wide range polymer concentration show an interesting re-entrant phase behavior where nanoparticles undergo from one-phase to two-phase system and back to one-phase system as a function of polymer concentration (Fig. 8a) [17]. The evolution of interaction and structure responsible for this phase behavior has been studied by SANS by contrast matching the polymer. The phase behavior is found to be governed by the interplay of different interactions (i) electrostatic repulsion between nanoparticles, (ii) polymer-induced attractive depletion between nanoparticles and (iii) repulsive polymer-polymer interaction present in the system [18]. At low polymer concentrations, the stability of this one-phase system is dictated by the dominance of electrostatic repulsion over the depletion attraction. On further addition of polymer, depletion attraction between nanoparticles sufficiently increases to give rise clustering of nanoparticles in two-phase system. The re-entrant phase is driven by the reduction in depletion attraction as a result of polymer-polymer repulsion at higher polymer concentrations. Both the magnitude and range of depletion interaction increase in going from one-phase to two-phase system, whereas decrease back in the re-entrant of one-phase system (Fig. 8b). The two-phase system is characterized by the nanoparticle clusters having surface fractal morphology.

The role of varying electrostatic repulsion by ionic strength and depletion attraction by molecular weight of polymer has also been studied. The combination of these parameters (ionic strength and molecular weight of polymer) with polymer concentration decides the interaction and structure, which can be used to tune the re-entrant phase behavior in nanoparticle-polymer systems.

Interaction and Resultant Structure of Nanoparticle and Protein Complexes

The nanoparticles, being small, can interact with cellular machinery in biological applications. For example, nanoparticle-protein systems are extensively utilized in drug delivery, catalysis, biological imaging, biosensors and bio fuel cell [19]. Silica nanoparticles are one of the most commonly used model inorganic nanoparticles, which are non-toxic and biocompatible. The globular proteins (e.g. BSA and lysozyme) are known to be highly stable and easily soluble in water. We have examined the differences in the interaction and structural evolution of colloidal silica nanoparticles for their interaction over a wide range of concentration of lysozyme and BSA proteins at physiological conditions [20]. It is found that despite of having different nature (opposite charge) both the proteins can render to the same kind of aggregation of silica nanoparticles. However, the concentration regions over which the aggregation is observed are widely different for the two proteins. The lysozyme with very small amount (e.g. 0.01 wt. %) leads to the aggregation of silica nanoparticles. On the other hand, silica nanoparticles coexist with BSA as independent entities at low protein concentrations and turn to aggregates at high protein concentrations (> 1 wt. %). In the case of lysozyme, the charge neutralization by protein on the nanoparticles gives rise to the protein-mediated aggregation of nanoparticles [21]. The nanoparticle aggregates coexist with unaggregated nanoparticles at low protein concentrations whereas with free protein at higher protein
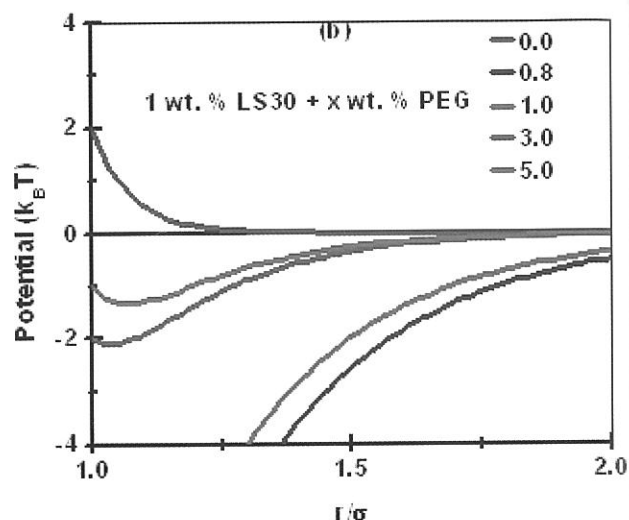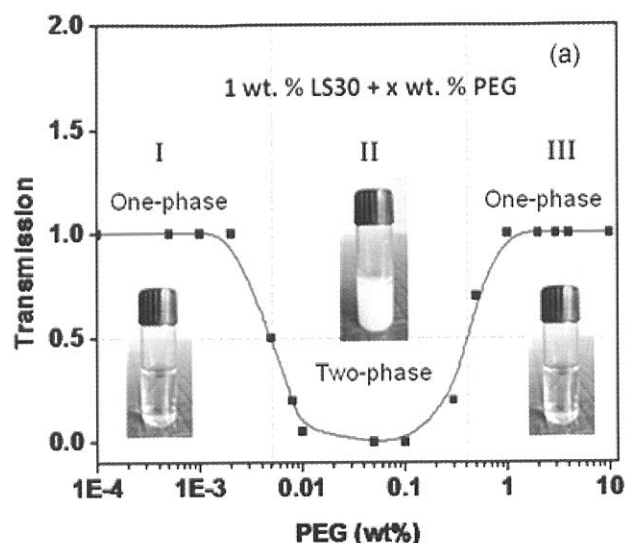
Fig. 8   (a) Phase behavior of 1 wt. % LS30 silica nanoparticles with varying PEG concentration in presence of 0.2 M NaCl in H₂O and (b) Total interaction potential for 1 wt. % LS30 silica nanoparticles with varying PEG concentration (0.8 to 5.0 wt. %).
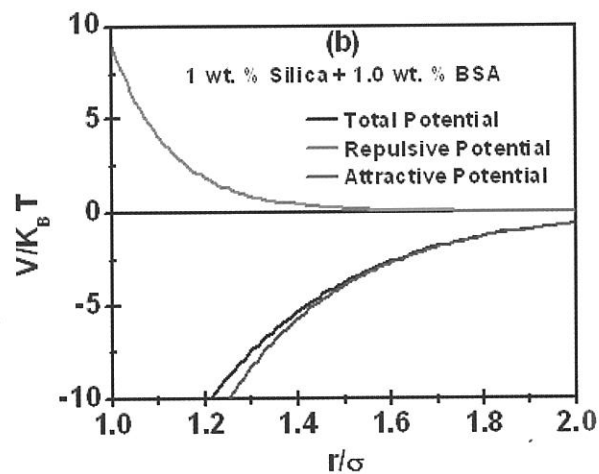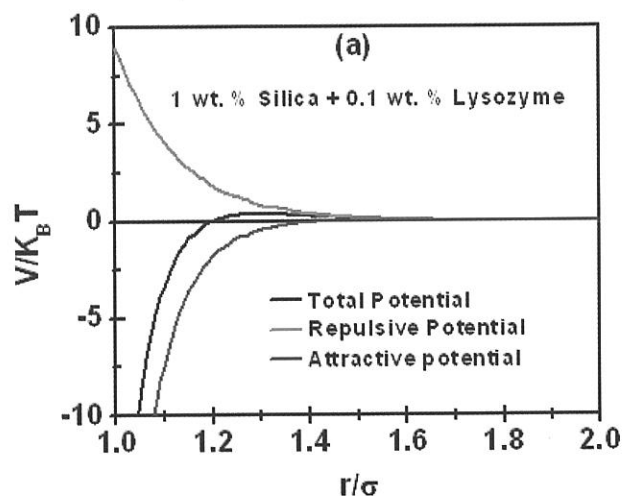

Fig. 9   The calculated interaction potentials from SANS data responsible for aggregation of silica nanoparticles in presence of (a) Lysozyme and (b) BSA proteins.

concentrations. For BSA, the non-adsorbing nature of protein produces the depletion force that causes the aggregation of nanoparticles at higher protein concentrations. The nanoparticle agg(a) Phase behavior of 1 wt. % LS30 silica nanoparticles with varying PEG concentration in presence of 0.2 M NaCl in H₂O and (b) Total interaction potential for 1 wt. % LS30 silica nanoparticles with varying PEG concentration (0.8 to 5.0 wt. %).regation is found to be governed by the short-range attraction for lysozyme and long-range attraction for BSA (Fig. 9). The aggregates are characterized by diffusion limited aggregate type of mass fractal morphology.

SANS has also been used to study resultant structures formed from lysozyme protein adsorption on different sized silica nanoparticles [22]. The studies were carried out on the nanoparticle systems having sizes much larger than the protein size. The protein adsorption on nanoparticle shows an exponential behavior with adsorption coefficient and saturation values increasing with the size of the nanoparticle. The adsorption of protein leads to the aggregation of nanoparticles which are characterized by the fractal structure. The nanoparticle aggregates coexist with un-aggregated particles at low protein concentrations whereas at high protein concentrations the excess free proteins are found with the nanoparticle aggregates. It is also found that the native protein structure is disturbed on their adsorption on nanoparticles. We have also examined the interaction and resultant structures of different sized silica nanoparticles and lysozyme protein in aqueous solution [23]. The measurements were performed at dilute samples (1 wt %) of three different sized silica nanoparticles (8, 16 and 26 nm) over a wide concentration range of protein (0-10 wt %) at three different pH values (5, 7 and 9). The adsorption curve as irrespective of nanoparticle size shows exponential
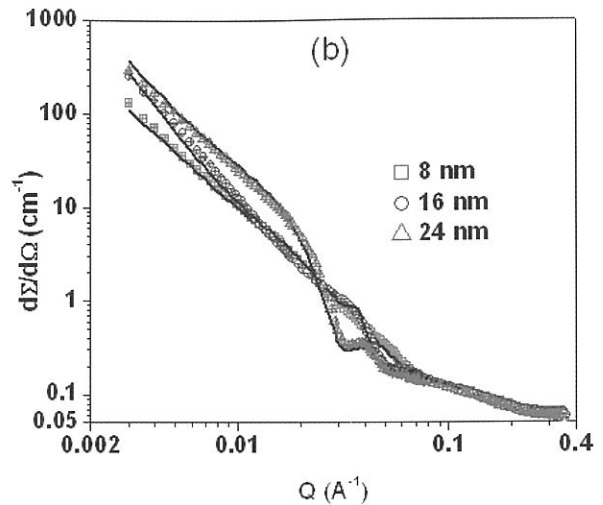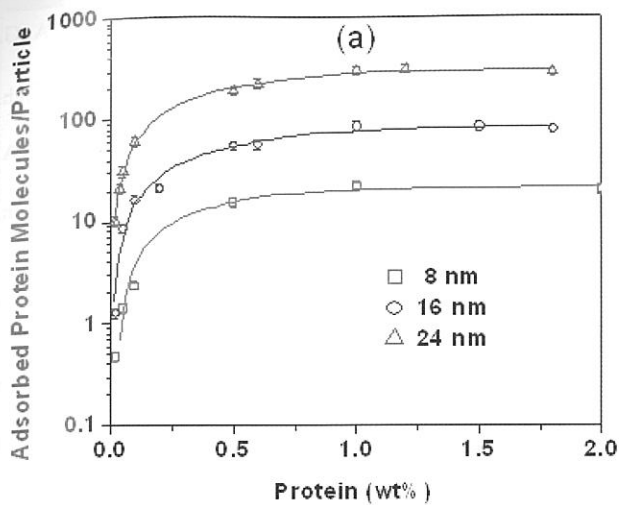
Fig. 10 (a) Lysozyme protein adsorption curve for 1 wt% different sized silica nanoparticles at pH 7. The overall adsorption of protein molecules increases with increase in particle size. (b) SANS data of 1 wt% protein with 1 wt% different silica nanoparticles at pH7. The data clearly show that size of the nanoparticle strongly influence the interaction of protein with nanoparticles.
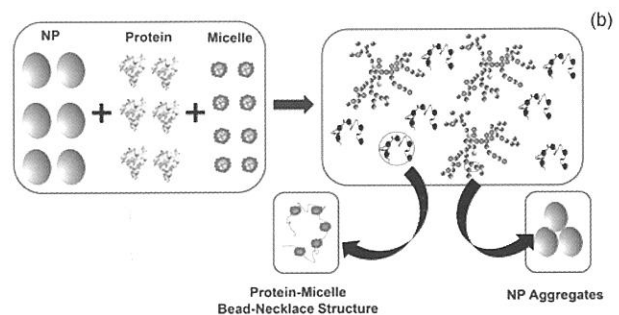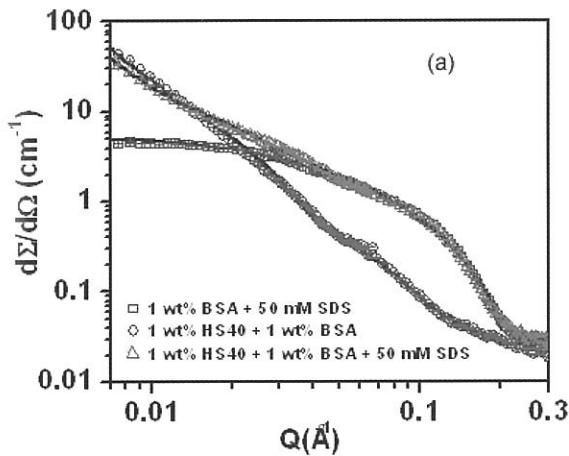

Fig. 11 (a) Data of three-component (nanoparticle-protein-surfactant) system are fitted by the sum of the scattering model of two-component systems of protein-surfactant and nanoparticle-protein. (b) Schematic of structures of nanoparticle-protein-surfactant complexes

behavior of protein adsorption on nanoparticles (Fig. 10a). The electrostatic interaction enhanced by decrease in the pH between nanoparticle and protein (iso-electric point ~ 11.4) increases the adsorption coefficient on nanoparticles but decreases the overall amount protein adsorbed whereas opposite of this behavior is observed with increase in nanoparticle size. The adsorption of protein leads to the protein-mediated aggregation of nanoparticles. These aggregates are found to be surface fractals at pH 5 which change to mass fractals with increase in pH and/or decrease in nanoparticle size (Fig. 10b). The two different concentration regimes of interaction of nanoparticles with protein have been observed: (i) un-aggregated nanoparticles coexisting with aggregated nanoparticles at low protein concentrations and (ii) free protein coexisting with aggregated nanoparticles at higher protein concentrations.

These concentration regimes are found to be strongly depending on both nanoparticle size and pH.

The interaction of the three-component system nanoparticle-protein-surfactant has been looked into based on the interactions of two component systems (nanoparticle-protein and protein-surfactant) [24, 25]. Fig. 11a shows the SANS data of three-component system of 1 wt% HS40 mixed with 1 wt% BSA and 50 mM SDS along with two-component systems of 1 wt% HS40 with 1 wt% BSA and 1 wt% BSA with 50 mM SDS. It is interesting to note that the scattering behavior of the three-component system is the cumulative effect of two component systems corresponding to protein-surfactant interaction as seen in the higher Q region and nanoparticle-protein in the lower Q region (Fig. 11a). The fact that both the protein and surfactant micelles show non-adsorption on silica nanoparticles, they can interact with each other and thus the

bead-necklace structures of their interaction are formed (Fig. 11b). This structure of protein-surfactant complex is found showing similar features with and without the presence of nanoparticles. The low Q behavior of scattering of the three-component system is similar to that observed in the two-component system of nanoparticle-protein but unlike the case of the nanoparticle-surfactant system. This suggests that the protein-surfactant complex behaves more like that of protein but unlike surfactant in interaction with nanoparticles. This is possible as the surface charge density of surfactant micelles is expected to decrease on the formation of the protein-surfactant complex, which makes the complex to behave more like that of nanoparticle-protein (depletion induced nanoparticle aggregation) than nanoparticle-surfactant (non-aggregation of particles).

Summary

SANS is an ideal technique for investigating the phase behavior of bio- and nanomaterials. We have extensively used this technique in protein and nanoparticle solutions as well as their complexes. Our results show that the phase behavior in these systems is governed by the delicate interplay of short-range/long-range repulsive and attractive interactions followed by formation of structures from nano to micron length scales.

Acknowledgement

References

[1]   D. Svergun and M.H.J. Koch, Rep. Prog. Phys. 66, 1735 (2003)

[2]   S. Chodankar and V.K. Aswal, Phys. Rev. E 72, 041931 (2005)

[3]   V.K. Aswal and P.S. Goyal, Curr. Sci. 79, 947 (2000)

[4]   J. S. Pedersen, Adv. Colloid Interface Sci. 70, 171 (1997).

[5]   A. Stradner, H. Sedgwick, F. Cardinaux, W.C.K. Poon, S.U. Egelhaaf, and P. Schurtenberger, Nature 32, 492 (2004)

[6]   A. J. Chinchalikar, V. K. Aswal, J. Kohlbrecher and A. G. Wagh, Phys. Rev. E 87, 062708 (2013)

[7]   S. Chodankar, V.K. Aswal, P.A. Hassan and A.G. Wagh, Physica B 398, 112 (2007).

[8]   V. K. Aswal, S. Chodankar, J. Kohlbrecher, R. Vavrin and A. G. Wagh, Phys. Rev. E 80, 011924 (2009)

[9]   Y. Liu, E. Fratini, P. Baglioni, W.R. Chen and S.H. Chen, Phys. Rev. Lett. 95, 118102 (2005).

[10] A.Shukla, E. Mylonas, E. D. Cola, S. Finet, P. Timmins, T. Narayanan and Dmitri I. Svergun, Proc. Natl. Acad. Sci. USA 105, 5075 (2008)

[11] L. Porcar, P. Falus, W.-R. Chen, A. Faraone, E. Fratini, K. Hong, P. Baglioni and Y. Liu J. Phys. Chem. Lett. 1, 126 (2010)

[12] A.J. Chinchalikar, S. Kumar, V.K. Aswal, P. Callow and A.G. Wagh, AIP Conf. Proc. 1447, 161 (2012)

[13] D Ray, V. K. Aswal and D. Srivastava, Nanosci. Nanotechnol. 10, 6356 (2010).

[14] D. Ray, V. K. Aswal and J. Kohlbrecher, Langmuir 27, 4048 (2011)

[15] A.J. Chinchalikar, V.K. Aswal, J. Kohlbrecher and A.G. Wagh, Chem. Phys. Lett. 542, 74 (2012).

[16] S. Kumar, M.-J. Lee, V. K. Aswal and S.-M. Choi, Phys. Rev. E 87, 042315 (2013)

[17] S. Kumar, D. Ray, V.K. Aswal and J. Kohlbrecher, Phys. Rev. E (submitted)

[18] D. Ray and V.K. Aswal, J. Phys.: Condens. Matter 26, 035102 (2014)

[19] D. Ray and V. K. Aswal, J. Nanopart. Res. 14, 778 (2012)

[20] I. Yadav, S. Kumar, V. K. Aswal and J. Kohlbrecher, Phys. Rev. E 89, 032304 (2014)

[21] S. Kumar, V.K. Aswal and J. Kohlbrecher, Langmuir 27, 10167 (2011)

[22] A.J. Chinchalikar, V.K. Aswal, J. Kohlbrecher and A.G. Wagh, J. Nanofluids 2, 194 (2013)

[23] S. Kumar, V. K. Aswal and P. Callow, Langmuir 30, 1588 (2014)

[24] S. Mehan, A.J. Chinchalikar, S. Kumar, V.K. Aswal and R. Schweins, Langmuir 29, 11290 (2013)

[25] S. Mehan, V.K. Aswal and J. Kohlbrecher, Langmuir 30, 9941 (2014)

Dr. V.K. Aswal joined BARC in 1993 after post-graduation in Physics from IIT, Bombay. He obtained Ph.D. from Bombay University and did post-doctoral research at Paul Scherrer Institute, Switzerland. Dr. Aswal is an expert in the field of scattering techniques and their applications to soft matter and nanomaterials and has published more than 250 research papers. Dr. Aswal is the recipient of many Young Scientist Awards, which include IUMRS Young Research Award (1998), IPA Best Thesis Award (1999), Associate of the Indian Academy of Sciences (2000-2005), IPA Satyamurthy Young Scientist Award (2001), Scopus Young Scientist Award (2007), and DAE-SSPS-2007 Young Achiever Award. He is the recipient of DAE Scientific & Technical Excellence Award (2008), DAE Group Achievement Award (2009), DAE-SRC Outstanding Investigator Award (2012) and Homi Bhabha Science & Technology Award (2012).

Probing Technologically Important Magnetic Materials using Neutron Scattering

S. M. Yusuf

Solid State Physics Division, Bhabha Atomic Research Centre, Mumbai 400 085, INDIA; E-mail: smyusuf@barc.gov.in

Abstract

Neutron scattering is an important technique to investigate structural and magnetic properties of magnetic materials. We have employed this technique in investigating several classes of technologically important magnetic materials. In this article, we bring out the usefulness of neutron diffraction, neutron depolarization and polarized neutron small angle scattering techniques in investigating static structural and magnetic properties of various types of technologically important magnetic materials.

Magnetic materials are very useful in the advancement of scientific and industrial growth. Magnetic materials are the key components of many electronics devices for storage and retrieval of information, such as computer hard drives and video tapes. Such materials are also in high demand in power generation and transmission, non-polluting electric vehicles, medical science, telecommunication, etc. Due to wide technological applications of magnetic materials, there have always been quests for new magnetic materials. Presently, an intense level of research is dedicated to fabricate new magnetic material based electronic devices. Magnetism constitutes several contemporary topics of research in science, such as giant magnetoresistance (GMR) effect, colossal magnetoresistance (CMR) effect, magnetocaloric effect, magnetic exchange bias effect, magnetic proximity effect, low dimensional magnetism, magnetism in nanoparticles, magnetism in high T_C superconductors, spintronics, molecular magnetism, quantum magnetism, topological insulators, and spin seebeck effect. Thus, an understanding of various aspects of magnetism and the related phenomena is very much essential to fabricate new magnetic materials. Neutron scattering technique has played an extremely important role in revealing the nature and mechanism of magnetic ordering at microscopic as well as mesoscopic length scales. Thermal neutrons are suitable for probing the positional arrangement of atoms, ions or molecules in condensed matter as the de Broglie wavelengths (2.86 – 0.905 Å) of the neutrons with thermal energies (10 - 100 MeV) are comparable to inter atomic spacing in condensed matter. Zero electric charge of neutrons also helps them to penetrate high into matter and therefore, the study of bulk materials is possible. Neutron is a spin ½ particle with a magnetic moment of -1.913 μ_n where μ_n is nuclear magneton. Zero electric charge of neutrons along with a magnetic moment makes them a useful tool to detect atomic magnetic moments without any interference from coulomb interaction. Unlike x-ray scattering (where the scattering amplitude is proportional to number of electrons (Z) in atom/ion), neutron nuclear scattering cross section is governed by a short-range nuclear interaction, and it does not vary monotonically across the elements of the periodic table due to the presence of resonance scattering term. This allows one to locate lighter atoms in presence of heavier atoms, and two consecutive elements in the periodic table. Neutron nuclear scattering even allows one to detect various isotopes of an atom. Unlike X-ray magnetic scattering, the neutron magnetic scattering length is comparable to nuclear scattering length ($\sim 10^{-12}$ cm), and it makes neutron magnetic scattering a very powerful tool for magnetic studies. Neutron scattering research has made significant impacts in physics, chemistry, metallurgy, biology and other fields. In this article, we give several examples to bring out the usefulness of neutron diffraction, neutron depolarization and polarized neutron small angle scattering techniques in investigating static structural and magnetic properties of various types of technologically important magnetic materials.

Revealing Coexistence of Magnetic Phases in the Semi-Heusler Spintronics Alloys Cu$_{1-x}$Ni$_x$MnSb

The half metallic ferromagnets have gained a large interest due to their unique property of coexistence of metallic behaviour for one electron spin (spin up), and insulating behavior for the other (spin down), causing spin polarization at the Fermi level. Due to potential technological applications of half metallic ferromagnets in spin based electronic (spintronics) devices, efforts are being made in designing suitable half metallic ferromagnetic materials and tailoring their magnetic and electronic properties to achieve 100% spin polarization. In this context, Heusler alloys and half Heusler alloys [1-7] have been the subject of research interest, particularly their electronic and magnetic properties since the discovery of their half metallic ferromagnetism [7]. In this article, we present a rich magnetic phase diagram of the semi-Heusler alloys Cu$_{1-x}$Ni$_x$MnSb. Besides, we present the interesting magnetoresistance properties for such alloys [1,2].

Our neutron diffraction study shows that the system Cu$_{1-x}$Ni$_x$MnSb (x < 0.05) is in the antiferromagnetic state (Fig. 1) with a moment of 3.14(3) μ_B per Mn (for x = 0.03) aligned perpendicular to the (111) planes. It is found that Ni does not carry any ordered moment. The present neutron diffraction and depolarization results suggest an electronic phase separation in the $0.05 \leq x \leq 0.2$ region where both antiferromagnetic and ferromagnetic phases coexist below ~50 K (Figs. 1-3). For x < 0.05, Cu$_{1-x}$Ni$_x$MnSb is mainly in the antiferromagnetic state (Fig. 1). For higher (x > 0.2) Ni substitution, the system fully transforms to the ferromagnetic phase (Fig. 1).
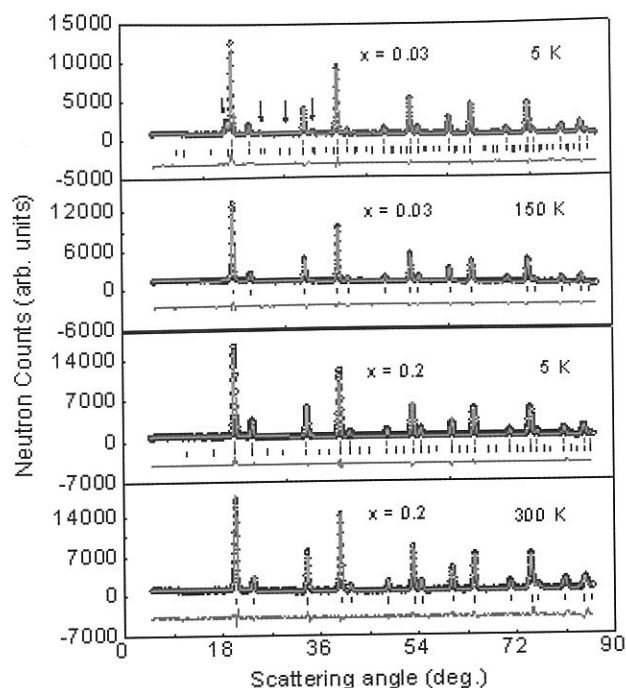
Fig. 1 *Rietveld refined neutron diffraction patterns for Cu₁₋ₓNiₓMnSb samples with x = 0.03 and 0.2 at temperatures above and below the magnetic ordering temperatures. For the x = 0.03 sample, the arrows show the antiferromagnetic Bragg peaks. For the x = 0.2 sample, the magnetic scattering at 5 K is fitted using the ferromagnetic ordering [1].*
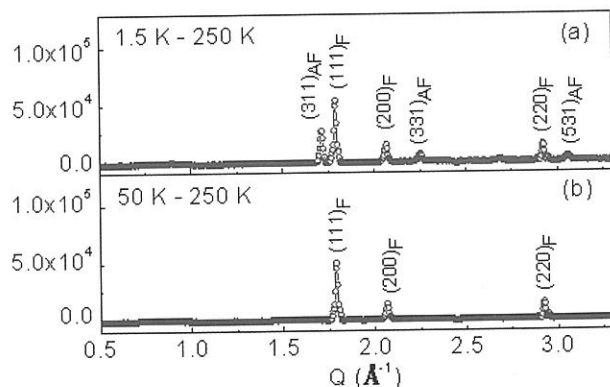

Fig. 2 *Difference neutron diffraction patterns for x = 0.15 sample at 1.5 K (a), and 50 K (b), obtained by subtraction of the neutron diffraction pattern at 250 K showing ferromagnetic (F) phase at 50 K, and coexistence of antiferromagnetic (AF) and F phases at 1.5 K [1].*

The present neutron depolarization study (Fig. 3) gives a quantitative estimate of magnetic inhomogenies (e.g., ferromagnetic clusters/domains in the antiferromagnetic matrix) on a mesoscopic length scale. The x = 0.03 sample does not show any depolarization down to the lowest measured temperature as the sample is in its antiferromagnetic phase. On the other hand, the x= 0.05,
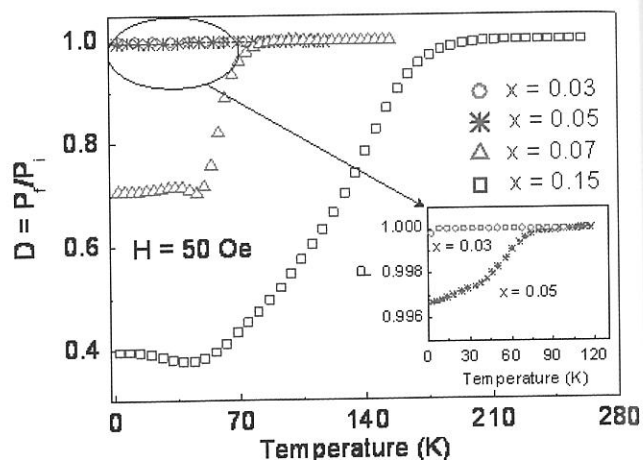

Fig. 3 *Temperature dependence of the neutron depolarization coefficient (D) at an applied field of 50 Oe for Cu₁₋ₓNiₓMnSb samples with x = 0.03, 0.05, 0.07, and 0.15 [1].*

0.07 and 0.15 samples show depolarization due the presence of ferromagnetic clusters or domains. The values of antiferromagnetic and ferromagnetic phase fractions along with the ferromagnetic domain/cluster size, derived from the neutron diffraction and neutron depolarization measurements, are presented in Table 1. A magnetic phase diagram (Fig. 4) for the Cu₁₋ₓNiₓMnSb series in the region x < 0.3 has been proposed by us [1].

TABLE 1. Magnetic phase fractions and ferromagnetic cluster size for Cu₁₋ₓNiₓMnSb

Ni conc. (x)	Volume phase fraction (%)		Ferromagnetic cluster/ domain size (nm)
	Antiferro-magnetc	Ferro-magnetic	
0.03	100	0	-
0.05	89.2	10.8	50
0.07	84.02	15.98	700
0.15	40.72	59.28	1300
0.20	11.75	88.25	~15000

The magnetoresistance (MR), the percentage change of resistivity due to applied magnetic field, is defined as $[\rho(H) - \rho(0)]/ \rho(0) \times 100$. We have investigated the MR properties for the alloy Cu₀.₈₅Ni₀.₁₅MnSb that shows a co-existence of long-ranged ferromagnetic and antiferromagnetic phases (Fig. 5). MR attains a maximum (negative) value of 6% for a field of 90 kOe at 100 K. In the ferromagnetic region, the change in MR with magnetic field is found to be more pronounced. In the low temperature region (below 45 K), where antiferromagnetic and ferromagnetic phases coexist,
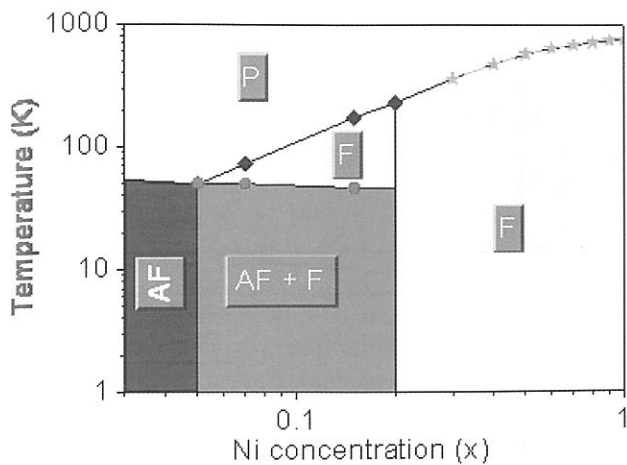
Fig. 4 Magnetic phase diagram of the $Cu_{1-x}Ni_xMnSb$ Heusler alloys. AF, F, and P denote antiferromagnetic, ferromagnetic and paramagnetic regions, respectively [1].
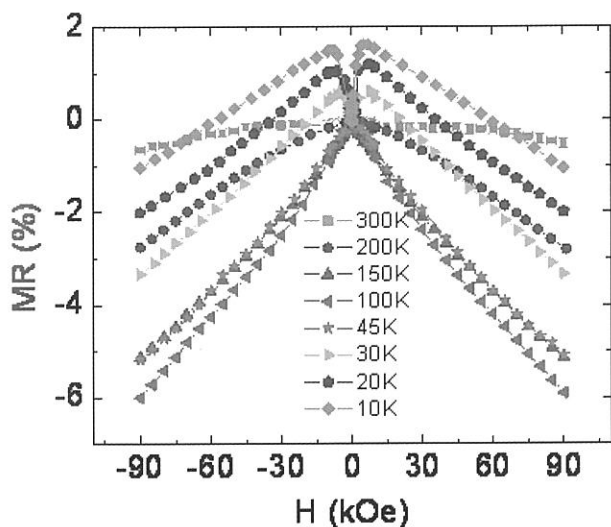

Fig. 5 Field dependence of magneto-resistance (MR) at various temperatures for $Cu_{0.85}Ni_{0.15}MnSb$ [2].

the MR is positive in low fields and becomes negative in high fields. At temperature below 45 K, since the sample has mixed ferromagnetic and antiferromagnetic phases, the antiferromagnetic phase causes the positive MR at low fields, and negative MR at high fields (due to the suppression of the antiferromagnetic spin fluctuations). On the other hand, the FM phase leads to a negative MR, thus resulting in a small positive MR in the low field and low temperature regime. The results presented here for such half-metallic type semi Heusler alloys are important to fabricate spin based electronic devices.

Rare Earth Based High Magnetocaloric Effect Material $TbCo_{2-x}Fe_x$

Materials showing large magnetocaloric effect (MCE), i.e., a large change in temperature of a material upon a moderate change of an external magnetic field under adiabatic condition, have attracted a lot of attention in recent years, due to their practical application in magnetic
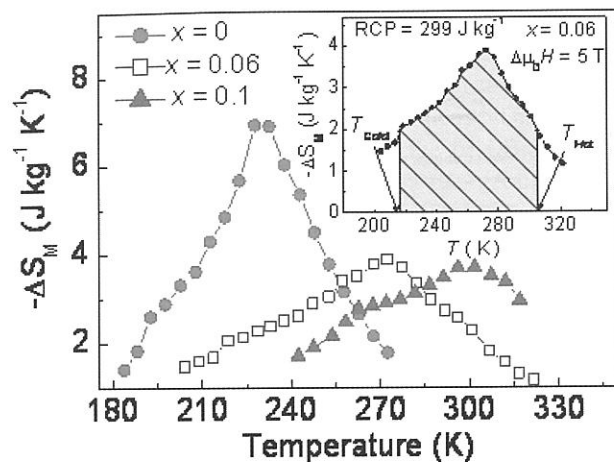

Fig. 6 Magnetic entropy change $-\Delta S_M$ vs T for $\Delta\mu_0H = 5$ T for the x = 0, 0.06 and 0.1 samples. The inset shows the $-\Delta S_M$ vs T curve under $\Delta\mu_0H = 5$ Tesla for x = 0.06 sample. The shaded area corresponds to the relative cooling power (RCP) [8].

refrigeration [8-14]. We present here our recent experimental results elucidating that the cubic Laves phase type compounds RCo_2, (R is a rare earth) are potential candidates for magnetic refrigeration applications as they show a large change in magnetic entropy (ΔS_M) around their magnetic ordering temperatures [8]. In the present study, we also show that an appropriate (Fe) chemical substitution not only tunes the paramagnetic to ferrimagnetic transition temperature to around room temperature but also increases the operating temperature range of magnetic refrigeration without significant reduction in the ΔS_M value.

We show in Fig. 6 the temperature dependence of ΔS_M for $TbCo_{2-x}Fe_x$ alloys [8]. The neutron diffraction experiments have been carried out to investigate the magnetostructural coupling which is important to gain a microscopic understanding of the observed high magnetocaloric effect across the magnetic phase transition in these rare earth- and transition metal-based alloys. From the analysis of the diffraction patterns measured at various temperatures we find that near the magnetic transition temperature T_C, there is also a structural phase transition. The low temperature phase is rhombohedral with a space group $R\bar{3}m$, and the higher temperature phase is cubic with a space group $Fd\bar{3}m$. There is an increase in the a-axis lattice parameter and, a decrease in the c-axis lattice parameter with increasing temperature [Fig. 7]. A relatively larger change in the lattice parameters is found near the magnetic transition temperature, indicating that the structural phase transition is coupled with the magnetic transition. For the Fe substituted samples, the structural transition also shifts towards a higher temperature along with the magnetic transition temperature indicating that there is a strong magneto-elastic coupling. A quantitative phase analysis of the rhombohedral and cubic phases has been made as a function of temperature across the structural/magnetic (magnetostructural) phase transition for both x = 0 and 0.1 samples, and the derived phase fractions
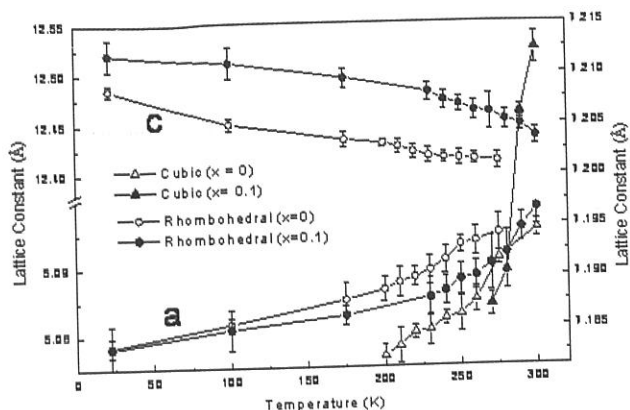
Fig. 7 *Temperature dependence of lattice constants of the rhombohedral (equivalent to cubic lattice) (y-axis: left) and cubic phases (y-axis: right) for the x = 0 and 0.1 samples. The error bars are within the symbols [8].*

Fig. 9 *Temperature dependence of magnetic moments (per ion) of (a) Tb and Co in $TbCo_2$ and (b) Tb, Co and Fe in $TbCo_{1.9}Fe_{0.1}$ along the c-axis. The net ordered moment values per formula unit of $TbCo_2$ and $TbCo_{1.9}Fe_{0.1}$ are also plotted [8].*

Fig. 8 *Rhombohedral and cubic phases across the magnetostructural phase transition. The dashed line above 300 K is the extrapolation of the data obtained below 300 K [8].*
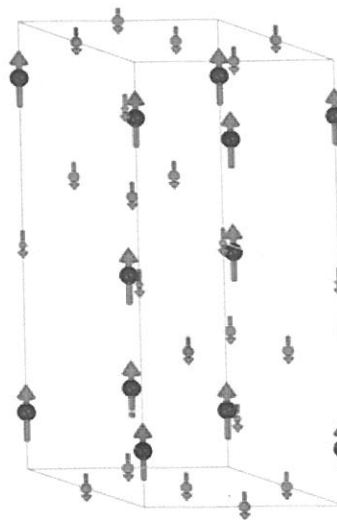
Fig. 10 *Ferrimagnetic ordering of Tb (up) and Fe/Co (down) moments for the rhombohedral phase in $TbCo_{2-x}Fe_x$.*

are plotted in Fig. 8. The refinement of the neutron diffraction patterns shows that magnetic ordering takes place only for the rhombohedral phase (ferrimagnetic ordering of the Tb and Co moments along the c-axis of the rhombohedral structure) (Fig. 9). The ferrimagnetic structure of the rhombohedral phase is shown in Fig. 10.

Reverse Monte Carlo simulation of Neutron Diffraction Data of Molecular Magnets

Molecular magnets of transition metal cyanides, known as Prussian blue analogues (PBAs) form a unique class of materials because of their interesting multifunctional properties, which make them suitable for possible technological applications in memory storage, ion sensing, hydrogen storage, biomedical, and photo switching based electronic devices, etc. We have investigated various molecular magnetic compounds [15-37] mainly belonging to the PBA [18-37] type compounds. The compounds of PBAs are represented by a common formula, $X_jA_k[B(CN)_6]_l \cdot mH_2O$ in which A and B are 3d transition metal ions which are periodically arranged in a cubic structure, and X is an alkali metal ion, such as K^+ or Rb^+. The transition metal A and B ions are located at the 4a (0, 0, 0) and 4b(½, ½, ½)

crystallographic positions, respectively, in a face centered cubic (fcc) structure. as shown in Fig. 11. The alkali metal ions and water molecules occupy the interstitial sites. Two types of water molecules i.e. coordinated and non-coordinated are generally present in PBA compounds depending on their stoichiometry (ratio k/l). The stoichiometry decides the $B(CN)_6$ vacancies and the water content. The presence of water molecules and $[B^{III}(CN)_6]$ vacancies causes structural disorder in the compounds and thus affects their magnetic properties. It is, therefore, very important to make a quantitative investigation of the structural disorder in such compounds.

We have used reverse Monte Carlo (RMC) simulation method on the neutron diffraction data to correlate magnetic properties of PBAs with their structural disorder [21,22,24,26,29,36]. Here we describe one specific example. For $Fe_{1.5}[Cr(CN)_6] \cdot zH_2O$ [36], the F(Q), the sum of the scattering amplitudes from all the atoms in the reciprocal space at a given scattering vector (Q) value is plotted in Fig. 12 (left). It is interesting to note that the first Bragg peak (100) is forbidden under Fm3m space group. Also, modulations in the background of the diffraction data show a large amount of diffuse scattering present in the compound. The forbidden B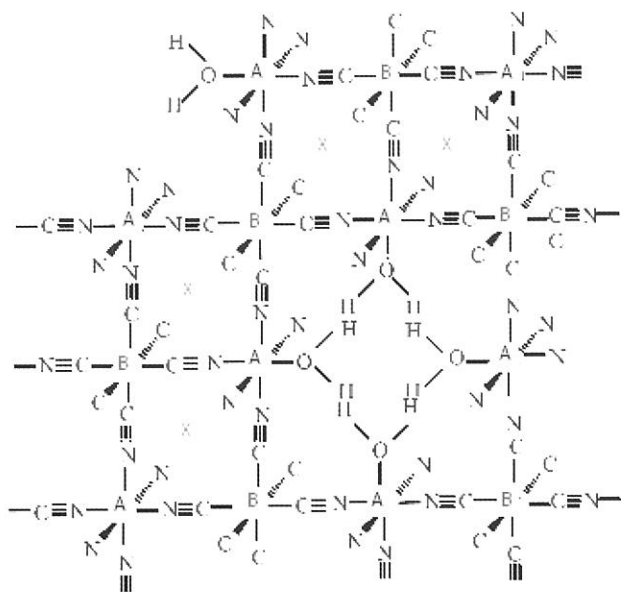ragg peak (100) in the neutron diffraction pattern has been fitted well using the RMC simulation; suggesting that this peak is related to an inherent structural disorder present in the compound. The distribution of oxygen atoms in the two dimensional plots is shown in the right panel of Fig. 12. The clustering (size ~ 3–4 Å) of the non-coordinated oxygen atoms around the coordinated oxygen atoms in the compound has been observed. Our RMC analysis shows that the oxygen clustering is mainly responsible for the structural disorder and reduction of T_C [36].

Investigation of Magnetic Field Driven Phase Transitions in Molecular Magnets:

We have observed an external magnetic field driven transition from an antiferromagnetic (AFM) ground state to a ferrimagnetic (FIM) state in $Rb_{0.19}Ba_{0.3}Mn_{1.1}[Fe(CN)_6] \cdot 0.48H_2O$ Prussian blue analogue [32]. In the presence of an external dc magnetic field, a decrease in AFM ordering temperature, and an appearance of a FIM phase is evident (Fig. 13). With increasing H, the AFM phase shrinks, and the FIM phase grows, and for H > 4□T, the AFM phase disappears completely and the system transforms to the FIM phase. An H-T phase diagram for the system is shown in Fig. 14. The results are significant in tuning magnetic properties under external weak perturbation.

Magnetic Correlations in 2-Dimensional Spin System with Anisotropic Properties

Low dimensional magnetic materials are in lime light as they show novel structural, magnetic, and electronic

Fig. 11 Crystal structure of PBAs with general formula of $X_j A_k [B(CN)_6]_l \cdot mH_2O$. The alkali metal ions (X) reside at interstitial positions.
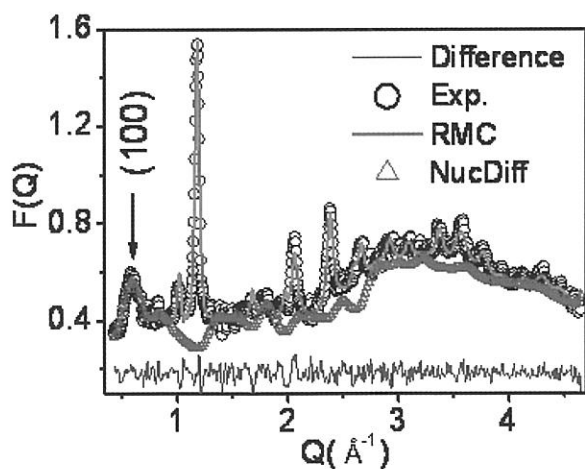
Fig. 12 (Left) The room temperature neutron diffraction patterns and the corresponding RMC simulated curves recorded for $Fe_{1.5}[Cr(CN)_6] \cdot zH_2O$. (Right) Contour plot shows the distribution and clustering of oxygen atoms after the RMC analysis [36].
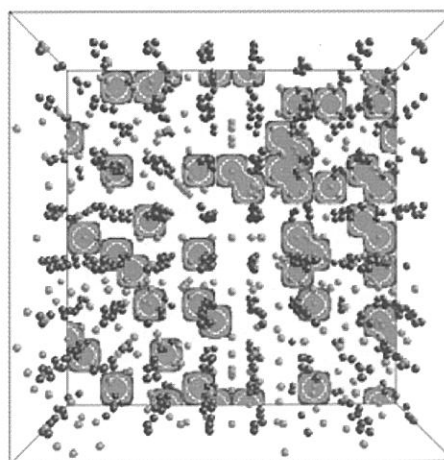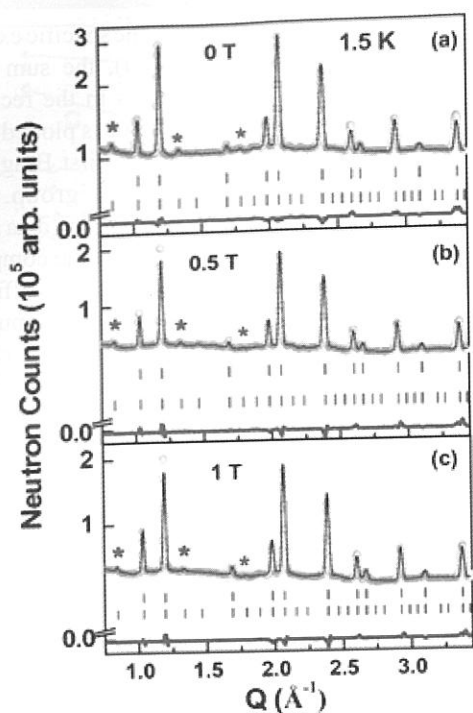
Fig. 13 Rietveld refined neutron-diffraction patterns for $Rb_{0.19}Ba_{0.3}Mn_{1.1}[Fe(CN)_6]0.48H_2O$ at 1.5 K. Solid line at the bottom shows the difference between observed and calculated patterns. (a) Vertical bars indicate the Bragg peaks position for nuclear (top row) and antiferromagnetic (bottom row) phase. (b) and (c), Bars indicate the allowed Bragg peaks position for nuclear and ferrimagnetic (top row), and antiferromagnetic (bottom row) phases. Asterisks mark the antiferromagnetic Bragg peaks [32].

Fig. 14 Magnetic phase diagram for the $Rb_{0.19}Ba_{0.3}Mn_{1.1}[Fe(CN)_6] \cdot 0.48H_2O$ PBA system in the temperature-magnetic field plane [32].
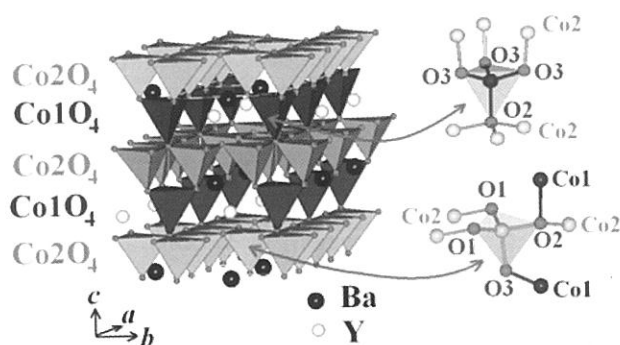
Fig. 15 Crystal structure of the geometrically frustrated layered compound $YBaCo_4O_7$

properties which are of importance in modern nanotechnology. We have employed neutron diffraction technique to investigate magnetic correlation in a large variety of low dimensional spin systems [38-59] which are quite important for their anisotropic physical properties. Layered cobaltites ($RBaCo_4O_{7+\delta}$, R = rare-earth ion) are a new class of geometrically frustrated magnets that have attracted a lot of attention [44] due to their unusual physical properties. The peculiar crystal structure, which contains Kagomé and triangular types of geometrical arrangements of the magnetic ions in the alternating layers, leads to the spin frustration within the Co layers in the ab-plane. We have investigated structural and magnetic correlations in the layered compound $YBaCo_4O_7$ by neutron diffraction. A hexagonal crystal structure (space group $P6_3mc$) with alternating tetrahedral layers of Kagomé and triangular types along the c axis has been found and is depicted in Fig.15. The neutron diffraction patterns (Fig. 16) show the presence of a short-range antiferromagnetic ordering (below $T_N \sim 110$ K) in the form of an addition broad peak (at $2\theta \sim 15$ deg.). The observed magnetic Bragg intensity (at 22 K) shows an asymmetric peak profile (saw tooth type), with a sharp rise in the intensity at the Bragg scattering angle and then a slow fall

at higher scattering angles. This kind of asymmetric peak shape is expected when the effective magnetic exchange is confined in a plane (2D ordering) and is absent (very weak) perpendicular to the plane. We have successfully fitted the observed magnetic Bragg intensity (at $2\theta \sim 15$ deg.), indexed with only two Miller indices, using the Warren function [44],

$$I_{hk}(2\theta) = C\left[\frac{\xi_{2D}}{(\lambda\sqrt{\pi})}\right]^{1/2} j_{hk}|F_{hk}|^2 \frac{(1+\cos^2 2\theta)}{2(\sin^{1/2}\theta)} F(a) .$$

where, C is a scale factor, ξ_{2D} is the 2D spin-spin correlation length within the 2D layer, λ is the wavelength of the incident neutrons, j_{hk} is the multiplicity of the 2D reflection (hk) with 2D magnetic structure factor F_{hk}, and 2θ is the scattering angle. The observed and fitted profiles along with variation of derived 2D (ξ_{2D}) magnetic correlations length are plotted in Fig. 17. The Kagomé layers have staggered chiral $(\sqrt{3} \times \sqrt{3})$ type spin structure which are uncoupled by triangular layer along the c axis.
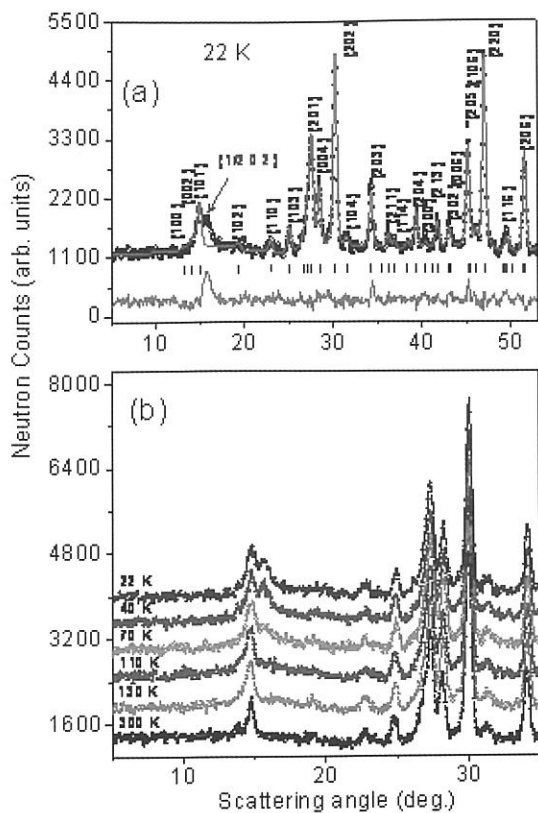
Fig. 16 (a) The observed, and calculated (nuclear phase only) neutron diffraction patterns at 22 K. (b) Diffraction patterns showing the growth of the intensity of (1/2 0 2) peak below 110 K [44].

Fig. 17 The magnetic peak profile at 22 K, after subtraction of nuclear background, and the fitted profile with Warren function. The inset shows the variation of 2D correlation length with temperature [44].
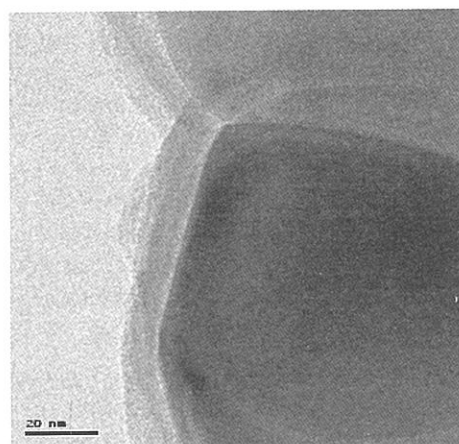
Fig. 18 The TEM images of the $BiFeO_3/NiFe_2O_4$ nanoparticles, showing the formation of a core-shell structure [63].

Investigation of Magnetic Nanoparticles with Core and Shell Structures

Magnetic nanoparticles (size range of 1-100 nm) can have wide technological applications in high density storage, spintronics, biological applications such as therapeutic drugs, gene and radionuclide delivery, radionuclide separation, contrast-enhancement agents for magnetic resonance imaging (MRI), etc. We have investigated a large variety of magnetic nanoparticle systems which are of technological importance [60-89]. Multiferroic-based core-shell nanoparticles have gained a considerable interest in recent years, because of their much higher magnetoelectric coupling, which make them suitable for designing spin-valve based magneto-electric random access memory (MERAM) [63, 67]. The operational principle of a MERAM is dependent on the phenomenon of exchange bias between two components of a composite system (mutiferroic, and ferro or ferrimagnet). In our recent study we have reported the presence of the desired exchange bias property in the multiferroic and ferrimagnetic based $BiFeO_3$ core/$NiFe_2O_4$ shell nanoparticle-system [63]. Here we show the usefulness of neutron diffraction in investigating structural and magnetic properties of the $BiFeO_3$ core/$NiFe_2O_4$ shell nanoparticle-system.

The identification of a core-shell structure of the present nanoparticle system $BiFeO_3$ core/$NiFe_2O_4$ was carried out with the aid of transmission electron microscopy (TEM) measurements. The TEM images [Fig. 18] of the nanoparticles show the presence of a core-shell structure, with a core-diameter of 60-70 nm and a shell thickness of 5-10 nm.

The microscopic nature of magnetic ordering in the present core-shell nanoparticle system has been determined from a low temperature neutron diffraction study. Here neutron diffraction is an effective technique to study the shell as well as core as the charge less neutrons can penetrate deep into the matter. Fig. 19 shows the Rietveld-refined neutron diffraction patterns of the core/shell nanoparticles, measured at 6 and 300 K. It can be noted here that the main magnetic peaks of $BiFeO_3$ [(003) and (101)] and $NiFe_2O_4$ [(111)] do not vanish at room temperature, which signifies that both these phases are magnetic even at room temperature. The results of the Rietveld refinement show that the $BiFeO_3$ core part orders antiferromagnetically in a G-type collinear structure, with Fe^{3+} magnetic moments oriented along the
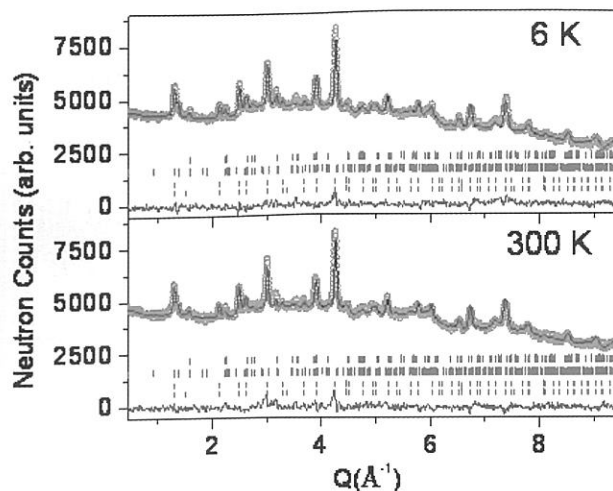
Fig. 19 The Rietveld-refined neutron diffraction patterns, of the BiFeO₃ core/NiFe₂O₄ shell nanoparticles, vs. Q [= (4π/λ) sinθ], where λ is the wavelength of the neutrons, and 2θ is the scattering angle. The solid line at the bottom shows the difference between observed and calculated patterns. The first (top most) and second arrays of the vertical lines show the positions of the BiFeO₃ nuclear and magnetic peaks, respectively. The third and fourth arrays of the vertical lines show the positions of the NiFe₂O₄ nuclear and magnetic peaks, respectively [63].

Fig. 20 The Rietveld-refined neutron diffraction pattern of the $La_{0.2}Ce_{0.8}CrO_3$ nanoparticles. The main antiferromagnetic peak has been marked by an arrow [66].

crystallographic c-axis. The analysis further shows that the nature of magnetic ordering of the $NiFe_2O_4$ shell is ferrimagnetic, where the Fe^{3+} and Ni^{2+} magnetic moments are found to orient along the crystallographic ±a-axis. At 6 K, the derived values of the Fe^{3+} magnetic moments are found to be 3.8(2) μ_B for $BiFeO_3$, 4.8(3) (tetrahedral A-site) and 4.6(4) μ_B (octahedral B-site) for $NiFe_2O_4$. At 300 K, these values decrease to 3.0(3) μ_B for $BiFeO_3$, 4.1(2) (A-site) and 3.8(2) μ_B (B-site) for $NiFe_2O_4$, which can be attributed to an increase in the thermal vibrations of the ions at 300 K. In $NiFe_2O_4$, the Ni ion also carries an ordered magnetic moment, which turns out to be 1.7 and 1.9 μ_B for A and B sites, respectively, at 6 K. At 300 K, the ordered Ni-moments reduce to 1.2 (for A-site) and 1.4 (for B-site) μ_B. The derived results are important in tuning the structural and magnetic properties of the core-shell nano-structured system for their possible application in MERAM.

Now we show that polarized neutron small angle scattering technique can serve an important role to investigate a core-shell magnetic structure in a "bare" nanoparticle sysem. The core and shell of a "bare" nanoparticle-system, remain magnetically coupled, and thus the magnetization contributions of core and shell become indistinguishable. In such cases, polarized neutron small angle scattering technique can be effective to reveal a core–shell structure. Here we present the results of the core–shell structure of a "bare" antiferromagnetic nanoparticle system $La_{0.2}Ce_{0.8}CrO_3$ [66] . The neutron

diffraction study establishes that the core of the present nanoparticles are antiferromagnetic in nature (Fig. 20) [66]. From the polarized neutron small angle scattering study we establish that these nanoparticles are core–shell type, where the magnetic scattering arises from the spin-disordered shell.

In a polarized neutron small angle scattering experiment, the difference between scattering cross sections of the (incident) two neutron polarization states gives a magnetic-nuclear cross term, $4F_N F_M \sin^2\alpha S(Q)$, where $F_N(Q)$ and $F_M(Q)$ are the scattering amplitudes for nuclear and magnetic scattering, respectively; α is the azimuthal angle made by the scattering vector Q with the external magnetic field, and S(Q) is the interparticle structure factor arising from the interaction between nanoparticles. The polarized neutron small angle scattering data at 2.5 K under a 3.5-T magnetic field show the presence of an asymmetric scattering [Fig. 21] in the iso-intensity plot of the $4F_N F_M \sin^2\alpha.S(Q)$ on the x–y detector. The observed asymmetry signifies the presence of a strong interference between nuclear and magnetic scattering amplitudes. The asymmetry observed in Fig. 21 is an indication of the $\sin^2\alpha$ behavior. A detailed analysis of the polarized neutron small angle scattering data shows a mean core diameter of 12.3±1.1 nm of an antiferromagnetic nature, and a shell thickness of 2.8 ±0.4 nm with a net magnetic moment.

Investigation of Magnetic Clusters in the CMR perovskite $(La/Dy)_{0.7}Ca_{0.3}MnO_3$

Manganite perovskites are important magnetic materials as they show colossal magnetoresistance (CMR) effect, an extremely important magnetotransport phenomenon that can be useful in magnetic recording industry. We have investigated a large varieties of such perovskites [90-105]. In one of our studies, we could tune magnetic and CMR properties of $La_{0.7}Ca_{0.3}MnO_3$ (by substituting Dy ion at the La-site) due to the ionic size effect (ionic radii of 0.91 Å and 1.06 Å, respectively) which distorts the crystal structure [94,98,99,103]. In our study, the starting parent compound $La_{0.7}Ca_{0.3}MnO_3$ shows a paramagnetic to ferromagnetic phase transition at ~250K [Fig. 22]. With the Dy substitution, the magnetic ordering temperature

2.5 K, 3.5 T
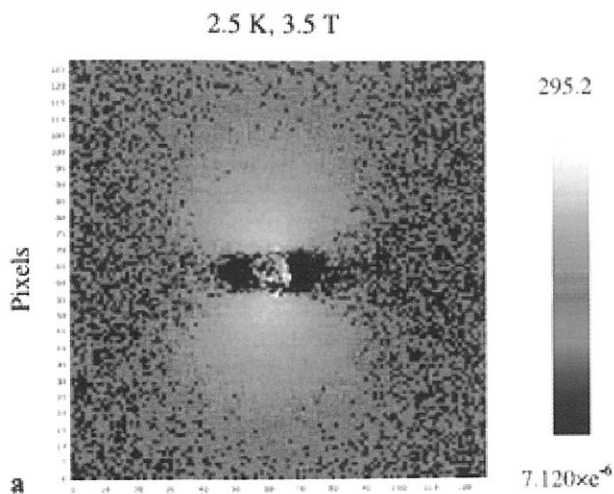
Fig. 21 The iso-intensity plots of $4F_N F_M sin^2 \alpha S(Q)$ patterns in the x–y detector measured at 2.5 K for $La_{0.2}Ce_{0.8}CrO_3$ under a horizontal field of 3.5 T, applied perpendicularly to the incident polarized neutron beam direction [66].
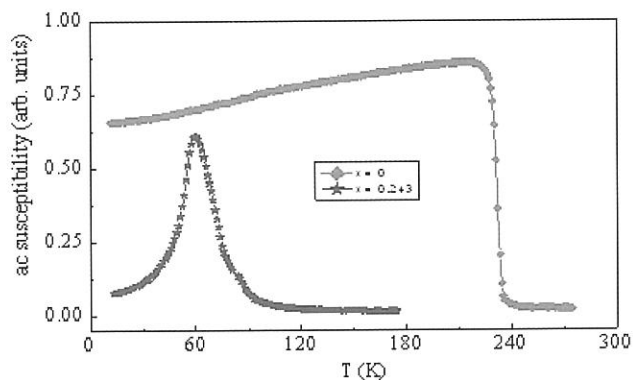
Fig. 22 Real part of ac susceptibility for $(La_{1.0-x}Dy_x)_{0.7}Ca_{0.3}MnO_3$ (x = 0 and 0.243) perovskites [98].

decreases, and a peak in χ_{ac} curve is found to occur at 60 K for the $(La_{1-x}Dy_x)_{0.7}Ca_{0.3}MnO_3$ with x =0.243 sample (Fig. 22). In order to understand the nature of magnetic ordering in the x = 0.243 sample we have used neutron small angle scattering.

Figure 23(a) depicts the Q-dependences of the background corrected small angle neutron scattering (SANS) signals at various applied fields for the x = 0.243 sample. For H = 0 and 2 kOe, we could analyze the observed SANS curves by considering the Lorentzian expression, $I_1/[Q^2 + \kappa^2]$, which implies that the magnetic correlations have the Ornstein-Zernike form $<M(0) . M(r)> \sim (1/r)$ exp(-κr) with κ as an inverse of the correlation length ξ. A finite correlation length ($\xi \approx 9$ Å) is found to exist at all higher temperatures in the paramagnetic state (Fig. 23(b)). With decreasing temperature, ξ starts to increase significantly at T ~ 75 K and a saturation behavior with $\xi \approx$ 16.5 Å is found at T ≤ 12 K. For H ≥ 6 kOe, the Q dependence
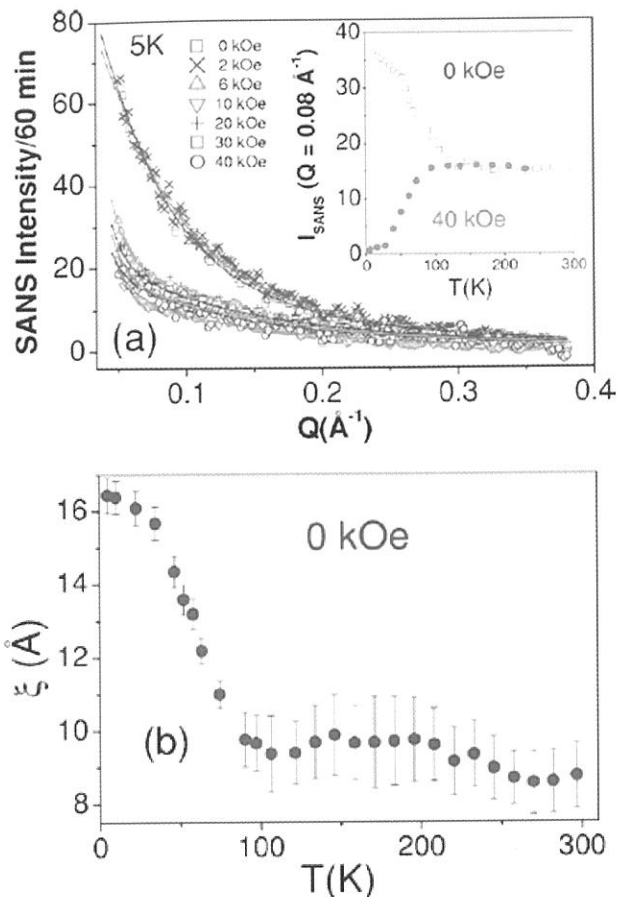
Fig. 23 (a) Small angle neutron scattering intensity as a function of Q for various H for $(La_{1-x}Dy_x)_{0.7}Ca_{0.3}MnO_3$ with x =0.243. The inset depicts the intensity at $Q = 0.08$ Å^{-1} vs T for 0 and 40 kOe. (b) Temperature evolution of correlation length ξ under H = 0 [103].

of SANS profile has been analyzed by considering the expression, $I_1/[Q^2 + \kappa^2] + I_2/Q^4$, where the second term (Porod law) is the tail part of the form factor of the spherical ferromagnetic domains, and dominates the "lower-Q" region of our measurements. The first term (Lorentzian term), originated from the short-range magnetic clusters, dominates the "higher-Q" region of our measurements. Under increasing applied field, the second term enhances at the expense of the first term. This indicates that the size of the smaller spin clusters grows under field, and these are transformed to large ferromagnetic domains. A decrease of SANS intensity at lower temperatures (below ~ 118 K) under 40 kOe, shown in the inset of Fig. 23(a), and the corresponding rise of magnetic Bragg intensity (not shown here) [103], support this argument. When field is applied, we demonstrate that the reduced spin fluctuations lead to the formation of a long-range ferromagnetic phase. The present example gives an understanding the role of an external magnetic field on such manganites which is extremely important in view of their CMR effect under magnetic field.

Summary and Conclusion

We have employed neutron scattering technique to investigate technologically important magnetic materials. In the present article, a broad overview of neutron diffraction, neutron depolarization and polarized neutron small angle scattering experimental investigations on several classes of technologically important magnetic materials is given. In particular, results from our recent studies on semi-Heusler spintronics alloys, rare earth based high magnetocaloric effect material, molecular magnets, layered spin system, core-shell type magnetic nanoparticles, and CMR perovskites have been presented. These materials have the potential for their use in information storage and processing, spintronics, drug delivery, cooling technology, etc. The usefulness of the neutron scattering technique to understand static structural and magnetic properties of various types of technologically important magnetic materials is brought out.

Acknowledgment

References

[1] M. Halder, S. M. Yusuf, A. Kumar, A. K. Nigam, and L. Keller, Phys. Rev. B 84, 094435 (2011).

[2] M. Halder, K.G.Suresh, M.D.Mukadam, and S.M.Yusuf, J. Magnetism and Magnetic Materials, 374, 75–79 (2015).

[3] M. D. Mukadam, S. M. Yusuf, and P. Bhatt, J App. Phys. 113, 173911 (2013).

[4] B. L. Ahuja, Alpa Dashora, H. S. Mund, K. R. Priolkar, S. M. Yusuf, M. Itou and Y. Sakurai Euro. Phy. Letts., 107, 27005 (2014).

[5] B. L. Ahuja, A. Dashora, S. Tiwari, H. S. Mund, M. Halder, S. M. Yusuf, M. Itou, and Y. Sakurai, J. App. Phys. 111, 033914 (2012).

[6] D. Serrate, J.M. De Teresa, R. Cordoba, and S.M. Yusuf, Solid State Communications 142, 363 (2007).

[7] R. A. de Groot, F. M. Mueller, P. G. van Engen, and K. H. J. Buschow, Phys. Rev. Lett. 50, 2024 (1983).

[8] M. Halder, S. M. Yusuf, M. D. Mukadam, and K. Shashikala, Phys. Rev. B 81, 174402 (2010).

[9] M. D. Mukadam and S. M. Yusuf, BARC NEWSLETTER 312, 28-31 (2010).

[10] S. M. Yusuf, M. Halder, A. K. Rajarajan, A. K. Nigam, and S. Banerjee, J App. Phys. 111, 093914 (2012).

[11] M. D. Mukadam and S. M. Yusuf, J. Appl. Phys. 105, 063910 (2009).

[12] S. M. Yusuf, A. Kumar, and J. V. Yakhmi, Appl. Phys. Lett. 95, 182506 (2009).

[13] M. D. Mukadam and S. M. Yusuf, Physica B 405, 686 (2010).

[14] M. Halder, S. M. Yusuf, and A. K. Nigam, J. Appl. Phys. 110, 113915 (2011).

[15] P. Bhatt and S.M. Yusuf, Surf. Sci. 605, 1861 (2011).

[16] P. Bhatt, N. Thakur, S. S. Meena, M. D. Mukadam, and S. M. Yusuf, J. Mat. Chem. C 1, 6637 (2013).

[17] P. Bhatt, N. Thakur, M. D. Mukadam, S. S. Meena, and S. M. Yusuf, J. Phys. Chem. C 118, 1864 (2014).

[18] A. Kumar, S.M. Yusuf, Pramana-J. Phys. 63,239 (2004).

[19] A. Kumar, S. M. Yusuf and L. Keller, Phys. Rev. B 71, 054414 (2005).

[20] A. Kumar and S. M. Yusuf, Physica B 362, 278 (2005).

[21] A. Kumar, S.M. Yusuf, L Keller, Physica B 385–386, 444 (2006).

[22] A. Kumar, S. M. Yusuf, L. Keller, J. V. Yakhmi, J. K. Srivastava, P. L. Paulose, Phys. Rev. B 75, 224419 (2007).

[23] M. D. Mukadam, A. Kumar, S. M. Yusuf, J. V. Yakhmi, R. Tewari, G. K. Dey, J. Appl. Phys. 103, 123902 (2008).

[24] A. Kumar, S. M. Yusuf, L. Keller, and J. V. Yakhmi, Phys. Rev. Lett. 101, 207206 (2008).

[25] S. M. Yusuf, A. Kumar, and J. V. Yakhmi, Appl. Phys. Lett. 95, 182506 (2009).

[26] S. M. Yusuf, N. Thakur, A. Kumar, and J. V. Yakhmi, J. Appl. Phys. 107, 053902 (2010).

[27] A. Kumar, S. M. Yusuf, and J. V. Yakhmi, Appl. Phys. A 99, 79 (2010).

[28] P. Bhatt, S. M. Yusuf, M. D. Mukadam, and J. V. Yakhmi, J. Appl. Phys. 108, 023916 (2010).

[29] N. Thakur, S. M. Yusuf and J. V. Yakhmi, Phys. Chem. Chem. Phys., 12, 12208 (2010).

[30] N. Thakur, S. M. Yusuf, A. Kumar, and J. V. Yakhmi, BARC Newsletter Oct, 413 (2011).

[31] V. K. Sharma, S. Mitra, A. Kumar, S. M. Yusuf, F. Juranyi, and R. Mukhopadhyay, J. Phys.: Condens. Matter 23, 446002 (2011).

[32] S. M. Yusuf, N. Thakur, M. Medarde, and L. Keller, J. Appl. Phys. 112, 093903 (2012).

[33] N. Thakur, S. M. Yusuf, P. L. Paulose, and L. Keller, J. Appl. Phys. 111, 063908 (2012).

[34] P. Bhatt, S. M. Yusuf, R. Bhatt and G. Schuetz, Appl. Phys. A 109, 459, (2012).

[35] A. Kumar, BARC Newsletter, Special issue, 190 -193, October 2013.

[36] P. Bhatt, N. Thakur, M. D Mukadam, S. S. Meena, and S. M. Yusuf, J. Phys. Chem. C 117, 2676 (2013)

[37] P. Bhatt, S. M. Yusuf, R. Bhatt, and G. Schuetz J. Solid State Electrochem. 17, 1285 (2013).

[38] A. Jain, S. M. Yusuf, S. S. Meena, and C. Ritter, Phys. Rev. B 87, 094411 (2013).

[39] C. Mondal, M. Ganguly, P. K. Manna, S. M. Yusuf, and T. Pal, Langmuir 29, 9179 (2013).

[40] S. M. Yusuf, A. Jain, and L. Keller, J. Phys.: Conden. Matt. 25, 146001 (2013).

[41] C. Ritter, S. M. Yusuf, A. K. Bera, Y. Goto, C. Tassel, H. Kageyama, A. M. Ar´evalo-L´opez and J. P. Attfield, Phys. Rev. B 88, 104401 (2013).

[42] A. Jain, P. Y. Portnichenko, Hoyoung Jang, G. Jackeli, G. Friemel, A. Ivanov, A. Piovano, S. M. Yusuf, B. Keimer, and D. S. Inosov, Phys. Rev. B 88, 224403 (2013).

[43] S M Yusuf and A K Bera, J. Korean Physical Society 62, 1393, (2013).

[44] A. K. Bera , S. M. Yusuf , and S. Banerjee, Solid State Sciences 16, 57 (2013).

[45] A. K. Bera and S. M. Yusuf, Phys. Rev. B 86, 024408 (2012).

[46] Anil Jain and S.M. Yusuf, Phys. Rev. B 83, 184425 (2011).

[47] S. M. Yusuf, A. K. Bera, C. Ritter, Y. Tsujimoto, Y. Ajiro, H. Kageyama, J. P. Attfield, , Phys. Rev. B. 84, 064407 (2011).

[48] S. S. Shinde, Sher Singh Meena, S. M. Yusuf, and K. Y. Rajpure, J. Phys. Chem. C 115, 3731 (2011).

[49] A. K.Bera, S. M. Yusuf, and I.Mirebeau, J. Phys.: Condens. Matter 23, 426005 (2011).

[50] S. M. Yusuf, A. K. Bera, N. S. Kini, I Mirebeau, and S. Petit, Phys. Rev. B. 82, 094412 (2010).

[51] A. K. Bera and S. M. Yusuf, J. Appl. Phys. 107, 013911 (2010).

[52] A. Jain, S. M. Yusuf, J. Campo and L. Keller, Phys. Rev. B 79, 184428 (2009).

[53] I. Nowik, A. Jain, S. M. Yusuf and J. V. Yakhmi, Phys. Rev. B 77, 054403 (2008).

[54] A. K. Bera, S. M. Yusuf, A. Jain, Pramana- J. Phys. 71, 917 (2008).

[55] A. Jain, S. M. Yusuf, S. Singh, Pramana- J. Phys. 71, 923 (2008).

[56] A. Jain, S. Singh, and S.M. Yusuf, Phys. Rev. B. 74, 174419(2006).

[57] S. M. Yusuf, J. M. De Teresa, P. A. Algarabel, M. D. Mukadam, M. J. Mignot, and I. Mirebeau, C. Marquina, and R. M. Ibarra, Phys. Rev. B 74, 184409 (2006).

[58] M. K. Mukhopadhyay, M. K. Sanyal, M. D. Mukadam, S. M. Yusuf and J.K. Basu, Phys. Rev. B 68, 174427 (2003).

[59] T. Charlton, D. Lederman, S.M. Yusuf, and G.P. Felcher, J. Appl. Phys. 85, 4436 (1999).

[60] P.K. Manna, and S.M. Yusuf, Physics Reports 535, 61–99 (2014).

[61] S.K. Giri, S. M. Yusuf, M.D. Mukadam, T.K. Nath, J. Alloys and Compounds 591, 181–187(2014).

[62] S. K. Giri, S. M. Yusuf, M. D. Mukadam, and T. K. Nath, J. Appl. Phys. 115, 093906 (2014).

[63] S. M. Yusuf, P. K. Manna, M. M. Shirolkar and S. K. Kulkarni, R. Tewari and G. K. Dey, J App. Phys. 113, 173906 (2013).

[64] S. M. Hossain, A. Mukherjee, S. Chakraborty, S. M. Yusuf, S. Basu, and M. Pal, Mater. Focus 2, 92 (2013).

[65] S. Kundu, M. D. Mukadam, S. M. Yusuf and M. Jayachandran, Cryst Eng Comm, 15, 482, (2013).

[66] P. K. Manna, S. M. Yusuf, M. D. Mukadam and J. Kohlbrecher, Appl Phys A 109, 385 (2012).

[67] P. K. Manna, S. M. Yusuf, R. Shukla and A. K. Tyagi, Phys. Rev. B 83, 184412 (2011).

[68] P. K. Manna, S. M. Yusuf, Mrinmoyee Basu and Tarasankar Pal, J. Phys.: Condens. Matter 23, 506004 (2011).

[69] P. K. Manna, S. M. Yusuf, R. Shukla, and A. K. Tyagi , Appl. Phys. Lett. 96, 242508 (2010).

[70] T. Sarkar, A. K. Raychaudhuri, A. K. Bera, and S. M. Yusuf, New J. Phys. 12 123026 (2010).

[71] M. Basu, A.K. Sinha, S. Sarkar, M. Pradhan, S. M. Yusuf, Y. Negishi, and T. Pal, Langumuir 26, 5836 (2010).

[72] S. Sarkar, S. Pande, S. Jana, A. K. Sinha, M. Pradhan, M. Basu, S. Saha, S. M. Yusuf, T. Pal, J. Phys. Chem. C 113, 6022 (2009).

[73] R. Shukla, Vinila. Bedekar, S.M. Yusuf, P. Srinivasu, A.Vinu and A.K. Tyagi, J. Nanoscience and Nanotechnology 9, 501 (2009).

[74] M. D. Mukadam, Amit Kumar, S. M. Yusuf, J. V. Yakhmi, R. Tewari and G. K. Dey, J. App. Phys 103, 123902, (2008).

[75] D. P. Dutta, Garima Sharma, P. K. Manna , A. K. Tyagi and S. M. Yusuf, Nanotechnology 19, 245609 (2008).

[76] P. Dey, T. K. Nath, P. K. Manna and S. M. Yusuf, J. Appl. Phys. 104, 103907 (2008).

[77] M. D. Mukadam and S. M. Yusuf, Physica B 403, 2602 (2008).

[78] Dimple P. Dutta, Garima Sharma, A.K. Rajarajan, S.M. Yusuf, G.K. Dey, Chem. Mater. 19, 1221 (2007).

[79] S. M. Yusuf, J. M. De Teresa, M. D. Mukadam, J. Kohlbrecher, M. R. Ibarra, J. Arbiol, P. Sharma, and S. K. Kulshreshtha, Phys. Rev. B. 74, 224428 (2006).

[80] M. D. Mukadam, S. M. Yusuf, R. Sasikala, and S. K. Kulshreshtha, J. Appl. Phys. 99, 034310 (2006).

[81] S. Karmakar, M. D. Mukadam, S. M. Yusuf, S. M. Sharma and A. K. Sood, J. Appl. Phys. Vol. 97, 054306 (2005).

[82] M. Mandal, S. Kundu, S. K. Ghosh, S. Panigrahi, T. K. Sau, S. M. Yusuf and T. Pal, J. Colloid and Interface Science, Vol. 286, 187 (2005).

[83] N. K. Prasad, D. Panda, S. Singh, M. D. Mukadam, S.M. Yusuf and D. Bahadur, J. Appl. Phys. Vol.97, 10Q903 (2005).

[84] M.D. Mukadam, S.M.Yusuf, P. Sharma, S.K. Kulshreshtha and G.K. Dey, Phys. Rev. B 72, 174408 (2005).

[85] A. Bharde, D. Rautaray, V. Bansal, A. Ahmad, I. Sarkar, S. M. Yusuf, M. K. Sanyal, M. Sastry, Small 2, 135 (2005).

[86] M. D. Mukadam, S. M. Yusuf, P. Sharma, and S. K. Kulshreshtha, J. Magn. Magn. Mater. Vol. 272, 1401 (2004).

[87] R. Vijayalakshmi, S.M. Yusuf and S.K. Kulshreshtha, J. Phys. & Chem. Solids Vol. 65, 975 (2004).

[88] M. Mandal, S. Kundu, S. K. Ghosh, T. K. Sau, S. M. Yusuf and T. Pal, J. Colloid Interface Science, 265, 23 (2003).

[89] M. Mandal, S. Kundu, T. K. Sau, S.M. Yusuf and T. Pal, Chem. Mater. 15, 3710 (2003).

[90] P. Sarkar, P. Mandal, K. Mydeen, A. K. Bera, S. M. Yusuf, S. Arumugam, C. Q. Jin, T. Ishida and S. Noguchi, Phys. Rev. B 79 (2009) 144431.

[91] P. Sarkar, P. Mandal, A. K. Bera, S. M. Yusuf, L. S. Sharath Chandra, and V. Ganesan, Phys. Rev. B 78 (2008) 012415.

[92] S. M. Yusuf, M. Sahana, M.S.Hegde, K.Dörr and K.-H. Müller, Phys. Rev. B 62, 1118 (2000).

[93] A. Das, M.Sahana, S.M. Yusuf, L.Madhav Rao, C.Shivakumara and M.S. Hegde, Mat. Res. Bull. 35, 651 (2000).

[94] S.M. Yusuf, R. Ganguly, K. Chakraborthy, P.K. Mishra, S.K. Paranjpe, J.V. Yakhmi and V.C. Sahni, J. Alloys & Compounds 326, 89 (2001).

[95] S.M. Yusuf, and M. Sahana, Ind. J. Phys. 75A, 357 (2001).

[96] S. M. Yusuf, M. Sahana, K. Dorr, U.K. Rößler and K. H. Müller, Phys. Rev. B 66, 064414 (2002).

[97] S.M. Yusuf, M. Sahana, K. Dorr and K. H. Mueller, Appl. Phys. A 74, S622 (2002).

[98] S. M.Yusuf, K. Chakraborty, S.K. Paranjpe, R. Ganguly, P.K. Mishra, J.V. Yakhmi and V.C. Sahni, Phys Rev B 68, 104421(2003).

[99] S. M. Yusuf, K. R. Chakraborty, R. Ganguly, P. K. Mishra, S. K. Paranjpe, J. V. Yakhmi and V. C. Sahni, J. Magn. Magn. Mater. 272-276, 1288 (2004).

[100] S. M. Yusuf, Pramana J. Phys. 63, 133 (2004).

[101] J. S. Srikiran and S.M. Yusuf, J. Alloys & Compounds 390, 26 (2005).

[102] J. S. Srikiran, A. Kumar and S.M. Yusuf, J. Magn. Magn. Mater. 295, 168 (2005).

[103] S. M. Yusuf, J. M. De Teresa, C. Ritter, D. Serrate, M. R. Ibarra, J. V. Yakhmi, and V. C. Sahni, Phys. Rev. B 74, 144427 (2006).

[104] S.M. Yusuf, J.M. De Teresa, P.A. Algarabel, J. Blasco, M.R. Ibarra, Amit Kumar and C. Ritter, Physica B 385–386, 401 (2006).

[105] J.M. De Teresa, C. Ritter, P.A. Algarabel, S.M. Yusuf, J. Blasco, Amit Kumar, C. Marquina and M.R. Ibarra, Phys. Rev. B 74, 224442 (2006).

Dr. S.M. Yusuf *is currently the Head of the Magnetism Section in Solid State Physics Division of BARC, and Professor, HBNI, Mumbai. He was a post-doctoral fellow at Argonne National Laboratory, USA, and a visiting scientist in the Institute of Materials Science, Spain. He is a specialist in the area of magnetic materials and neutron scattering. He has nearly 200 research publications, one international patent, several book chapters, and review articles to his credit. He has guided 8 Ph. D students and delivered more than 120 invited talks in various forums. He is a Fellow of the National Academy of Sciences, India and a referee of the Nature publishing Group, Physical Review Letters, and Physical Review B. Dr. Yusuf is the recipient of Dr. P. K. Iyenger memorial award, DAE Homi Bhabha Science & Technology Award, DAE SRC outstanding research investigator award, MRSI Medal and Indian physical society's best young physicist award.*

Development of Associated Particle Imaging Technique for Explosives Detection

Amar Sinha, Tushar Roy, P.S. Sarkar, Tarun Patel

Neutron & X-ray Physics Division, Bhabha Atomic Research Centre, Trombay, Mumbai 400 085;
E-mail: image@barc.gov.in

Abstract

Neutron based explosive detection is used as confirmatory sensor for characterizing elements used in explosives. There are several neutron based technique which are used for such purpose. However, there are major issues of signal to noise ratio as the size of object to be inspected increases. In order to improve upon this ratio, Associated Particle Imaging(API) method which is also called tagged neutron technique is being developed. We report on this development and work carried out in our lab.

Introduction

Explosive materials are normally composed for hydrogen, nitrogen, oxygen, carbon. Many of these elements are also present in several non-explosive materials such as plastic, cotton, food items etc. The main challenge is to distinguish explosive from non-explosive. X-ray based systems show only shapes and sizes and cannot distinguish explosives from other similar benign materials.

In contrast, neutron based detection techniques have shown to be very promising candidates for detection and identification of hazardous and illicit materials. The principal elemental constituents of narcotic and explosive substances (H, C, N and O) differ strongly from one-another in their interactions with neutrons and can thus be characterized via these differences. It can be seen from table 1 that explosives are distinguished by relatively high proportions of nitrogen and oxygen and relatively low proportions of carbon and hydrogen. On the other hand, illicit drugs are generally rich in hydrogen and carbon and poor in nitrogen and oxygen. These features may be utilized to identify the presence of explosives and illicit drugs hidden amongst other materials inside a vehicle or cargo. As neutrons have better penetration capabilities, threat materials can be detected even if they are hidden under a large thickness of organic or metallic structure.

Neutron based techniques are based on detecting gamma which is emitted through inelastic and/or neutron capture reactions. The emitted gamma rays have distinct energies which are characteristic of the elements from which they are emitted. These can be used as finger prints for precisely identifying the elements and finally deciphering the chemical composition of the hidden elements. There are a variety of neutron based techniques such as Thermal neutron Activation (TNA), Fast Neutron Analysis (FNA), Pulsed Fast-Thermal Neutron Analysis (PFTNA), Neutron resonance radiography, Pulsed Fast Neutron Analysis (PFNA) and Associated Particle Imaging (API), which can be employed for detection and identification of these materials. In particular, the Associated Particle Technique for detection of explosives gives additional information on localization of explosive material. This method is also known as tagged neutron technique or nanosecond analysis(NNA) technique. API technique uses inelastic gamma signature as compared to capture gamma which are generally used in TNA method. One of the main advantage of API technique is that it uses neutron gamma coincidence to localize volume of interest and looks for signature of elements in specified voxel. This results in significant improvement in signal to noise ratio as background signal from rest of the voxel and surrounding is not counted.

Associated Particle Imaging (API)

In this technique, suspect volume under investigation is irradiated with fast neutrons (14 MeV in D-T reaction). In $D(T,n)\alpha$ reaction, each neutron is emitted almost back to back with the alpha particle. The detection of alpha by a position sensitive detector determines the direction of the alpha particle and thus the direction of the outgoing neutron

TABLE 1: Elemental densities or ratios of three classes of substances

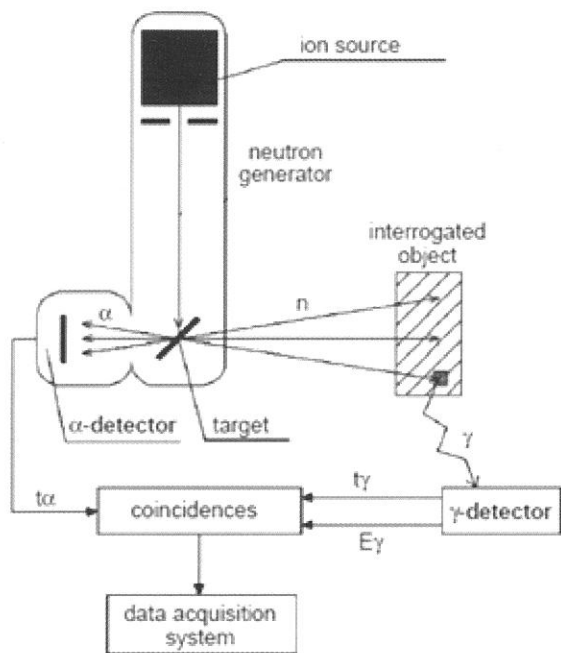| Density or Ratio	H	C	N	O	Cl	C/O	C/N	Cl/O
Explosives	Low-Medium	Medium	High	Very High	Medium to None	Low, <1	Low, <1	Low
Narcotics	High	High	Low	Low	Medium	High, >3	High	Very High
Plastics	Medium-High	High	High to Low	Medium	Medium to None	Medium	Very High	-

Fig. 1   Schematic of Associated Particle Imaging

(Fig.1). This "tagged" neutron undergoes inelastic scattering in the material of interest. The de-excitation γ-rays released from nuclei activated in fast neutron inelastic scattering events are detected by an array of detectors. Specific elements present in each volume element or "voxel" of the object are identified through the γ-ray spectra measured by each detector in coincidence with the tagged neutron. The main signatures used are derived from detecting the 4.43 MeV γ-ray from ^{12}C, the 5.12 MeV γ-rays from ^{14}N, and the 6.130 MeV γ-ray from ^{16}O.

The time difference between the detection of the alpha particle and the recording of the γ-ray by gamma detector is practically determined by the flight path of the neutron. In this way, it is also possible to determine the depth along the cone of neutrons where the reaction occurs. Using a two-dimensional position-sensitive detector, the transverse co-ordinates of reaction sites can be mapped. Merging these two information, a three dimensional image of the reaction points can be reconstructed. This feature is extremely important in the search for hidden objects.

Advantages of API

API has certain distinct advantages over other techniques

1. Improvement in the signal to background ratio in comparison with systems using fast neutrons

2. Possibility to inspect a precise element of volume (voxel) that has been identified as suspect by other techniques

3. The use of fan / cone beams allows the simultaneous measurement of gamma rays emitted also in neighboring voxels thus allowing the online subtraction of the background from the suspect item.
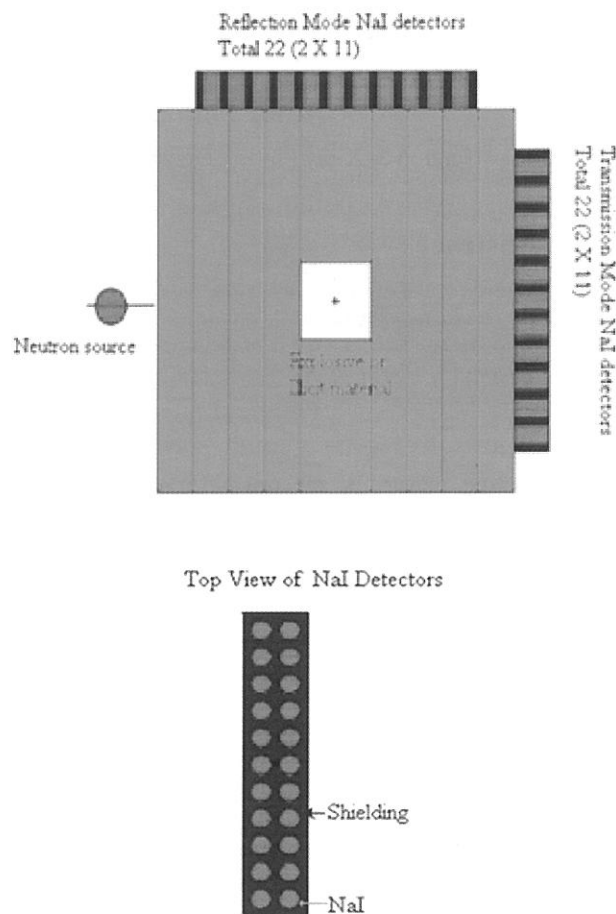
Fig. 2   Simulation model for API

Simulation Study of API

We have simulated a cargo container having different amount of explosives in a metallic matrix using Monte Carlo Technique. The dimension of cargo matrix was chosen to be 250(W) X 250(H) X 100(L) cm^3 for the simulation purpose. The cargo was assumed to be filled with uniform density of metallic/organic matrix and different quantities of explosive were placed at different locations. A typical sketch of the system under study is shown in Fig. 2.

NaI(Tl) detector of 5" diameter and 10" length with a total of 44 detector set were used for simulation purpose with 22 detectors each for the transmission and reflection mode. The detectors were put in front (transmission) and top (reflection) geometry in order to increase the efficiency of detection process. The NaI(Tl) detectors are kept in a matrix of lead which helps to protect the detectors from counting the unwanted scattered signal. Hence this helps to achieve not only the collimation but improves signal to background ratio.

Different explosive concentration was kept at the centre of the cargo and the sum of detectors in TOP array in coincidence gate was calculated. Figure 3 shows the coincidence gamma spectrum obtained. It can be seen that the signal from ^{12}C (4.43 MeV) and ^{16}O (6.13 MeV) are major lines which can be easily resolved while signal from
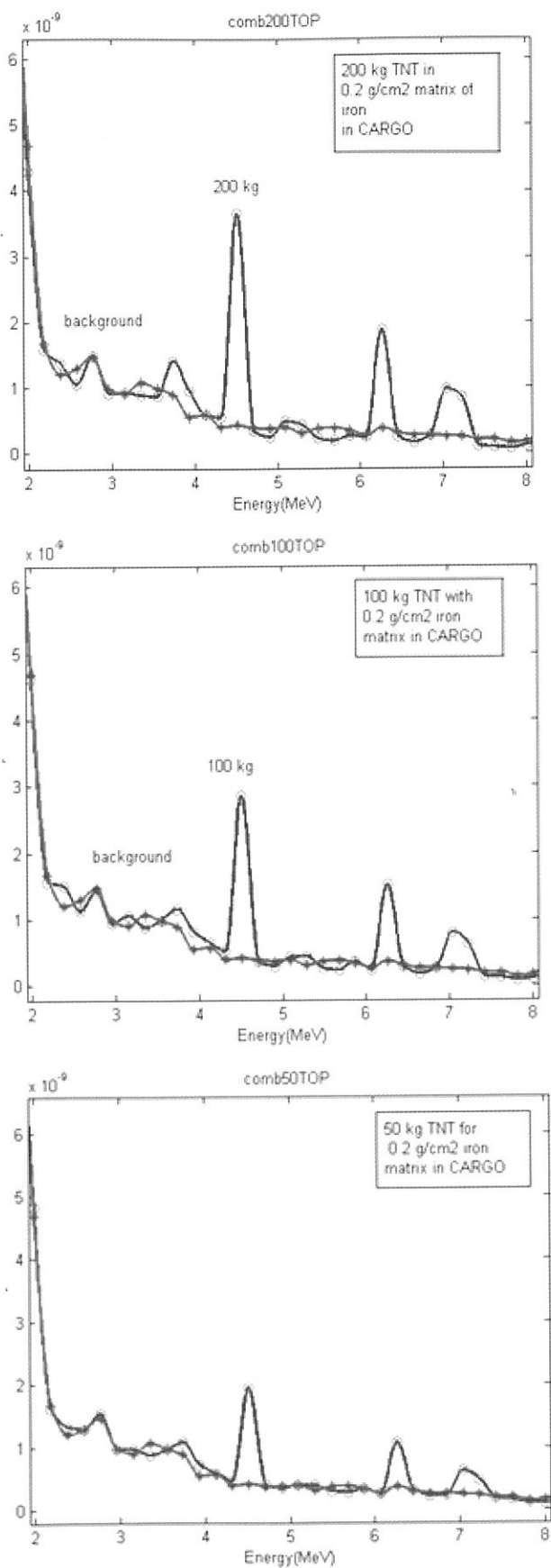
Fig. 3   Gamma spectrum (coincident) from TOP detectors for different amount of TNT explosive (a) 200 kg (b) 100 kg (c) 50 kg

[14]N (5.11 MeV) is weak. Moreover the tagged background is also small.

Work done on Explosive Detection at BARC

There are several steps before a API based technique can be implemented. These include development of detector system for measuring prompt gamma from inelastic reaction, suitable neutron generator development, integration of detector, electronics, data acquisition system for API.

Experiments with PGNAA

Elemental characterization of low Z elements (C, H, Cl, Fe) inside bulk materials were performed using PGNAA technique. Samples having elemental composition similar to explosives were used for such experimentations using moderated DT (14 MeV) neutrons. We could observe characteristic prompt capture gamma rays of hydrogen (2.224 MeV), nitrogen (10.83 MeV), also inelastic (n,n'γ) prompt gamma signal (4.43 MeV) of carbon. BGO detector has been used for gamma spectrum acquisition. These experimentations has been carried out for initial feasibility studies of detecting prompt gamma lines as a part of PGNAA technique based explosive detection system development.

Experimental System for API

An API based explosive detection system has been developed at BARC using D-T neutron generator and BGO detectors. The system is assembled such that it can be installed for scanning the suspect object in either a single-sided geometry or as portal and can be used to scan objects. For laboratory testing, the system has been coupled to a fixed D-T neutron generator. The neutron generator with API is shown in Fig.6.
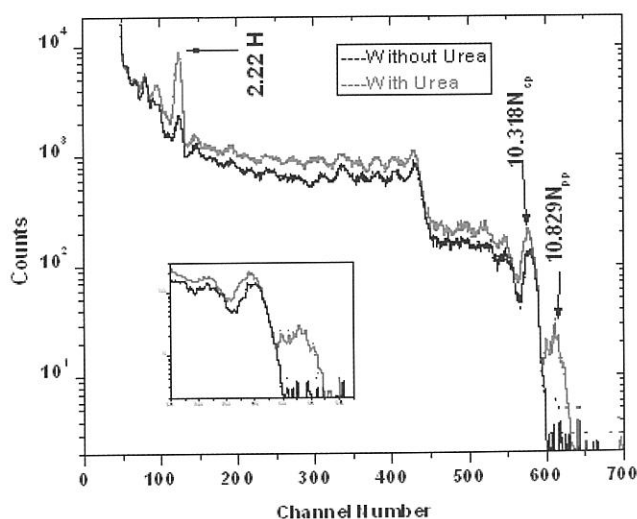
Fig. 4   Graph of Signal from urea and background data in terms of counts versus channel. The Hydrogen photopeak at 2.22 MeV and the nitrogen photopeak at 10.829 MeV are very clearly visible.
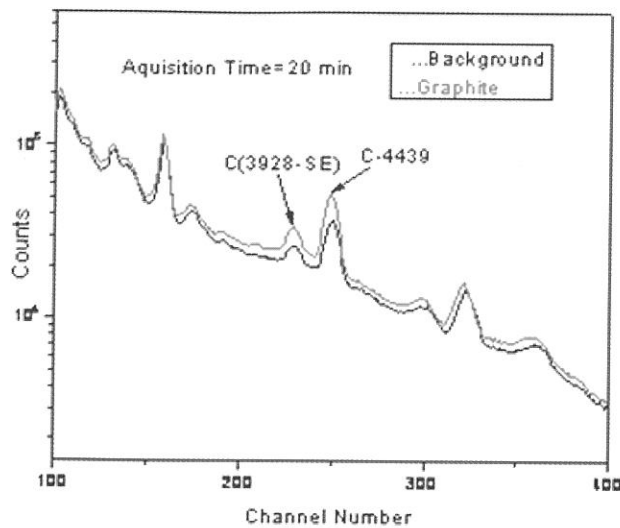
Fig. 5   *Carbon lines at 4.43 MeV and its single escape (3.9 MeV) from graphite sample irradiated with DT (14 MeV) Neutron*
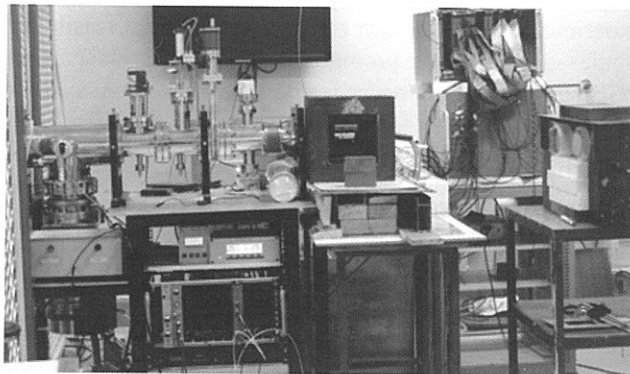
Fig. 6   *Neutron Generator for API*

Experimental Results for API

Test experiments on different benign materials and some explosive simulants have been carried out using this system to deduce their chemical compositions. The experimental results are briefly discussed here.

Figure 7 shows the gamma spectrum obtained for graphite and water samples which give elemental signature of carbon and oxygen respectively. Fig.8 shows the gamma spectrum obtained for explosive simulant melamine ($C_3H_6N_6$)

Conclusion

An experimental program to design neutron based explosive detection system using API technique has been describes. Results of initial experiments and simulation are presented. Several feasibility experiments have been carried out.

Acknowledgement
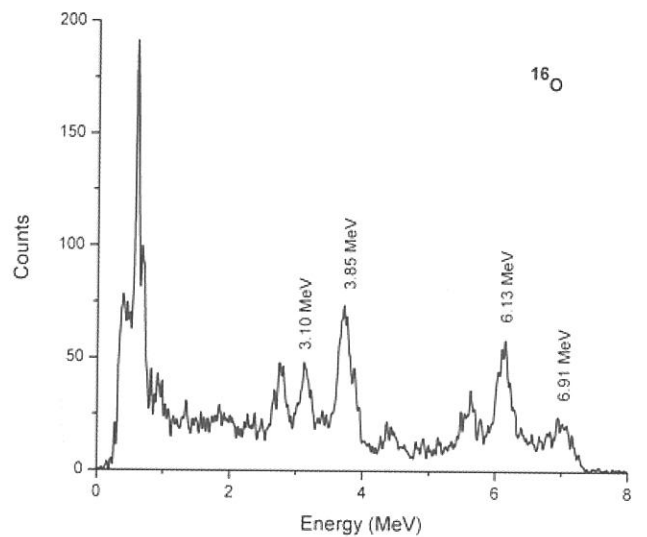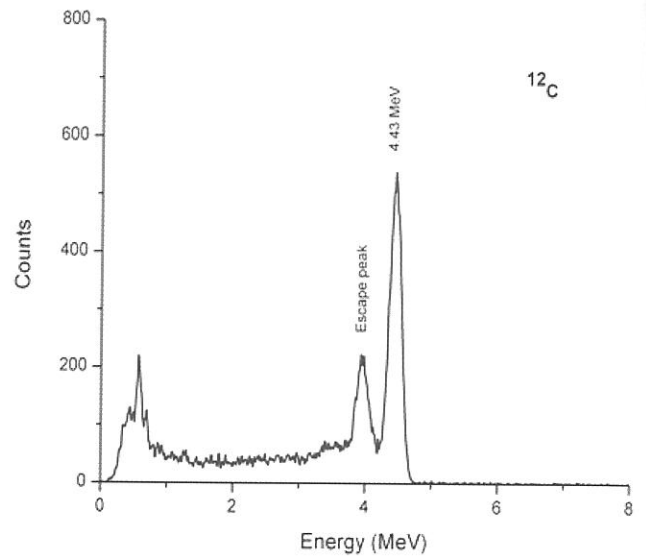
Fig. 7   *Gamma signatures of carbon (graphite) and oxygen (water)*
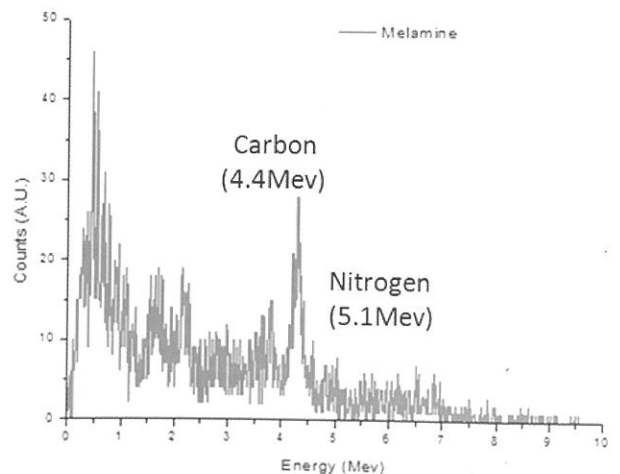
Fig. 8   *Gamma spectrum for Melamine ($C_3H_6N_6$)*

References

[1] Andy Buffler, "Contraband detection with fast neutrons", Radiation Physics and Chemistry71 (2004) 853–861

[2] Gozani, T., "Novel applications of fast neutron interrogation methods", Nucl. Instrum. Methods A353 (1994), 635–640.

[3] Gozani, T., "Neutron based non-intrusive inspection techniques", Proc. Int. Soc. Opt. Eng.2867(1997) 174–181.

[4] Vourvopoulos, G.,"Accelerator based techniques for contraband detection", Nucl. Instrum. Methods B89(1994) 388–393.

[5] W.V. Nunes et al, Applied Radiation and Isotopes56 (2002) 937-943

[6] Lunardon, M., Nebbia, G., Pesente, S., Romagnoli, G.M., Viesti, G.,Barbui, M., Cinausero, M., Fioretto, E., Prete, G., D'Erasmo, G.,Palomba, M., Pantaleo, A., "A large area scanning system using14MeV neutron tagged beams for non-destructive assays", Nucl. Instrum. Methods B213 (2004) 544–547.

[7] Vourvopoulos, G., Womble, P.C., "Pulsed fast/thermal neutron analysis: a technique for explosives detection", Talanta54 (2001) 459–468

Dr. Amar Sinha joined BARC in 1977 after graduating from the 20th Batch of BARC Training School and is currently the Head of Neutron & X-ray Physics Division. He obtained his PhD degree from University of Mumbai and served as a Visiting Scientist at the Joint Research Centre of European Communities at ISPRA, Italy during 1986-87. He has worked extensively on neutron physics, spallation neutrons, radiation damage, application of neutron generator for detection of explosive and fissile material, and radiography, X-ray and neutron tomography. He has played a major role in the development of country's first zero power ADS. He is recipient of DAE Homi Bhabha Science and technology award (2011), Technical Excellence award (2005) and several group achievement awards.

Shri Tushar Roy is from the 48th batch of training school. His area of interest includes emission tomography, neutron radiography, phase contrast imaging and accelerator driven subcritical systems. He is currently working on applications of neutron generator for detection of explosives and contraband (associated particle imaging) and detection of fissile material (differential die-away).

Dr. P.S. Sarkar is a senior Scientific Officer in NXPD, BARC. He obtained his PhD degree in Physics from Mumbai University. He has been awarded with YAST Award by DAE in 2009. His areas of research are in X-ray and Neutron based imaging, micro and macro tomography, medical imaging, transient imaging, development of systems for active neutron based explosive and fissile material detection, development of miniature detectors for thermal and fast neutron detection. He has a number of publications in these areas.

Shri Tarun Patel is from 47th batch of BARC training school. He is currently working on development of neutron generators for sub-critical system, neutron radiography and explosive & fissile material detection applications. He has specialization in design and development of fixed type neutron generators for lab applications and compact size sources for field applications.

X-ray absorption Spectroscopy with Synchrotron Radiation

C. Nayak, A.K. Yadav, S. Basu, P. Rajput, A. Agrawal, A.K. Poswal, D. Bhattacharyya*, S.N. Jha and N.K. Sahoo

Atomic & Molecular Physics Division, Bhabha Atomic Research Centre, Mumbai 400 085; *E-mail: dibyendu@barc.gov.in

Introduction

X-ray absorption spectroscopy (XAS) generally deals with measurement of absorption coefficient as a function of X-ray photon energy around an X-ray absorption edge of an element in a material. X-ray absorption spectrum consists of two parts: (i) The spectrum near the absorption edge (viz., the X-ray near edge structure or the XANES part) gives information about the external perturbations in the valence states to which electrons make transitions from core levels upon absorption of X-ray photon energy and hence XANES can yield information regarding hybridization of orbitals in case of molecule or long range order existing in a crystalline sample apart from the oxidation states of the absorbing atom in the material. (ii) The second part of the spectrum which extends from 50 eV to ~700 eV above the absorption edge is generally called the Extended X-ray absorption fine structure (EXAFS) part which is generally characterized by the presence of fine structure oscillations and can give precise information regarding the short range order and local structure around the particular atomic species in the material. This determination is confined to a distance given by the mean free path of the photoelectron in the condensed matter, which is between 5-7 C radius from the element. The above charatersistic along with the fact that EXAFS is an element specific tool, makes EXAFS a powerful structural local probe. With the advent of modern bright Synchrotron radiation sources, this technique has emerged out to be the most powerful local structure determination technique which can be applied to any type of material viz. amorphous, polycrystalline, polymers, surfaces, solutions. Furthermore, EXAFS does not require any particular experimental conditions, such as high vacuum and hence samples of various physical forms can be adapted for measurements in the experimental stations [1,2].

Theoretical Formulation:

The X-ray absorption coefficient for an atom in the photon energy range of 1-100 keV is generally dominated by Photoelectric effect as shown in Fig.1, which is a monotonically decreasing function of energy with several discontinuities known as absorption edges. These discontinuities occur when the energy of the incident photons equals the binding energy of different core levels of the atom and are classified with capital letters (K,L, M...) according to the principal quantum number of the core level ground state ($n = 1, 2, 3...$). The edge energy is characteristic of each atom and in the case of an isolated atom (monatomic gas), the absorption coefficient decreases smoothly between two subsequent edges. However, in a real material the spectrum always shows oscillations as shown in the inset of figure 1 for Ge K edge. An incident photon is able to extract a
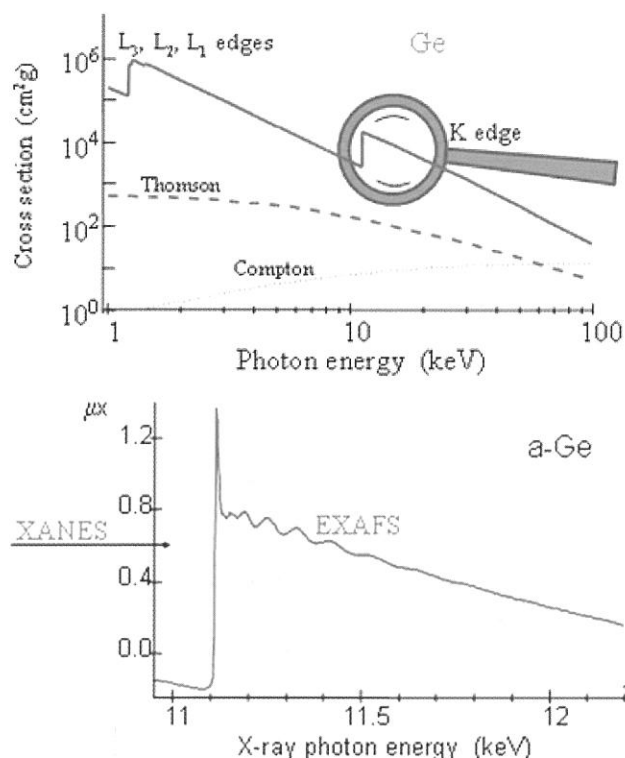
Fig. 1 K edge of Ge crystal with inset showing the fine structure oscillations

core electron (henceforth called as photoelectron) if its energy is equal to or greater than the edge energy. If the absorbing atom is isolated in space, the photoelectron propagates as an unperturbed isotropic wave, but in a real material since the absorber is surrounded by several neighbouring atoms, the photoelectron gets back-scattered and the final state of the photoelectron can be described by the superposition of the outgoing and back-scattered waves. This leads to an interference phenomenon that modifies the interaction probability between core electrons and incident photons and thus gives rise to the fine-structure oscillation in the X-ray absorption spectrum. Constructive interference increases while destructive interference decreases the absorption coefficient of the atom. This interference phenomenon, for a given energy of the photoelectron, depends on the distance between emitting and scattering atoms, their scattering strengths and coordination numbers or in other words, these local structure information can be derived from the EXAFS oscillations in the absorption spectra.

Since the oscillations in the absorption spectra are important, the experimentally obtained μ versus E data are

first plotted as $\chi(E)$ versus E, where $\chi(E)$ is defined as follows:

$$\chi(E) = \frac{\mu(E) - \mu_0(E)}{\Delta\mu_0(E_0)} \qquad (1)$$

where, E_0 is the absorption edge, $\mu_0(E)$ is the bare atom background and $\Delta\mu_0(E_0)$ is the step in the $\mu(E)$ value at the absorption edge. The energy scale is also converted to the wave number scale k, given by:

$$k = \sqrt{\frac{2m(E - E_0)}{\hbar^2}} \qquad (2)$$

$\chi(k)$ is weighted by k^2 to amplify the oscillations at high k and finally the $\chi(k)k^2$ versus k spectra is Fourier transformed to generate the $\chi(R)$ versus R spectra in terms of real distances from the centre of the absorbing atom.

Under the dipole approximation, an analytical expression of the EXAFS signal can be derived as follows [3]:

$$\chi(k) = \sum \frac{N_j f_j(k) e^{-2k^2\sigma_j^2} e^{-\frac{2R_j}{\lambda}}}{kR_j^2} \sin\left[2kR_j + \delta_j(k)\right] \qquad (3)$$

where, N_j is the number of jth neighbours of the absorbing atom sitting at a distance of R_j, having a scattering amplitude of f_j and creates a phase change of δ_j as the photoelectron get scattered by its potential. The term σ_j represents the fluctuation at the atomic positions (having both structural as well as thermal effect) and λ_j is the mean free path which determines the probability of the scattering photoelectron to come back at the absorber after being back scattered by the neighbour.

Different relevant local structure parameters from the EXAFS signal are determined by fitting the experimental EXAFS spectra with the above theoretical expression. The amplitude, distance, phase and degeneracy of the different contributions corresponding to different interactions (nearest neighbour and further interactions) are used as fitting parameters for fitting the experimental data. Different codes for EXAFS data analysis programme are available among which the IFEFFIT package is most commonly used [4].

Experimental Methods

The most important experimental requirement to carry out EXAFS measurements is that of a continuous X-ray source with high intensity and Synchrotron radiation sources only match with this criterion. EXAFS measurements with synchrotron radiation are generally carried out in two different modes viz., energy scanning mode and energy dispersive mode. In the energy scanning mode, the experimental arrangement (generally called a beamline) uses a Double-crystal–Monochromator (DCM) to select a particular energy from the incident white synchrotron beam, which is then made incident on the sample. The intensity of the transmitted beam passing through the sample or that of
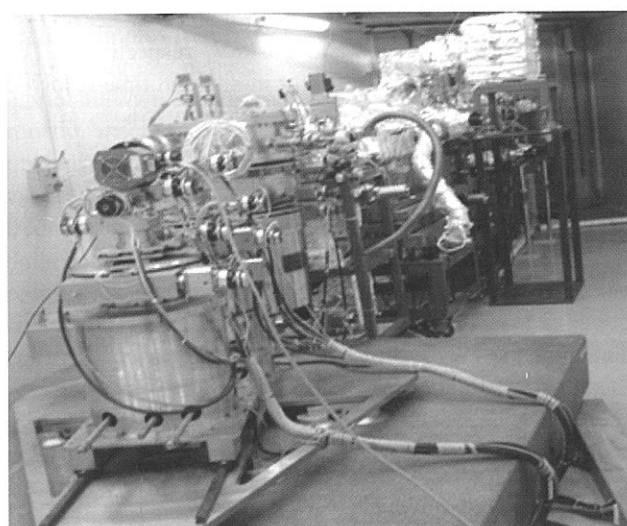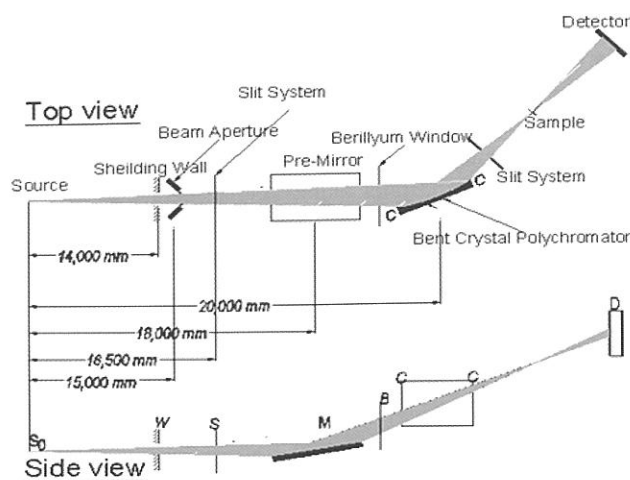
Fig. 2 (a) Schematic Optical Lay-out and (b) Photograph of the energy dispersive EXAFS Beamline

the fluorescence beam emerging out of the sample is recorded with suitable detectors along with the intensity of the incident beam at each energy and the whole spectrum is recorded by changing the Bragg angles of the DCM crystals and thereby scanning the energy. In the energy dispersive mode, on the other hand, a long bent crystal polychromator is used to select a band of energy from the white synchrotron beam which is horizontally dispersed and focused on the sample. The transmitted beam intensity from the sample is recorded on a position sensitive CCD detector, thus enabling recording of the whole EXAFS spectrum around an absorption edge in a single shot. At INDUS-2 Synchrotron radiation source at RRCAT, Indore both the above facilities are available, the energy dispersive EXAFS beamline (BL-08) had been operational since 2009, while the energy scanning EXAFS beamline (BL-09) has been commissioned in 2013.

The optical layout and the photograph of the energy dispersive EXAFS beamline (BL-08) at INDUS-2 are shown in Figs. 2(a) and (b). This beamline uses a 460 mm long Si (111) single crystal mounted on a mechanical

crystal bender which can bend the crystal to the shape of an elliptical cylinder in such a way that the source and the sample position are at the two foci of an ellipse. The crystal selects a particular band of energy from white synchrotron radiation depending on the grazing angle of incidence of the synchrotron beam (Bragg angle) and disperses as well as focuses the band on the sample. A Rh coated cylindrical pre-mirror with meridional curvature is used for rejection of higher harmonics and vertical focusing of the beam. The radiation transmitted through the sample is detected by a position sensitive CCD detector having 2048 x 2048 pixels. The whole absorption spectrum of the sample can be recorded simultaneously on the detector within fraction of a second. The beamline is designed to cover the photon energy range of 5-20 keV providing energy bandwidths of 0.3, 1.0 and 2.0 keV and with resolution of 0.5, 1 and 2 eV per pixel at photon energies of 5, 10 and 20 keV, respectively. The beamline is particularly useful for in-situ and time-resolved studies on samples in transmission geometry [5].

The energy scanning EXAFS beamline (BL-09), which has been commissioned recently, covers a photon energy range of 4-25 keV and has a resolution (E/ΔE) of 10^4 at 10 keV. The optical layout and the photograph of the beamline are shown in Figs. 3(a) and (b) respectively. The beamline uses a 1.3 m long meridional cylindrical mirror with a radius of curvature of 11.2 Kms coated with Rh/Pt as a collimator. This mirror is followed by a double crystal monochromator (DCM). The DCM consists of two Si (111) crystals with 2d = 6.2709Å and narrow Darwin width (~ 6 arcsec). 1st crystal is cooled by indirect water-cooled arrangement and temperature is stable within ± 0.1 deg C. The second crystal of the DCM is a sagittal cylinder with radius of curvature in the range 1.28-12.91 m which provides horizontal focusing to the beam. A post mirror with meridional curvature is used in face-down configuration for bending the beam path to horizontal direction again as well for focussing the beam vertically at the sample position. For measurements in the transmission mode, the sample is placed between two ionization chamber detectors. The first ionization chamber measures the incident flux (I_o) and the second ionization chamber measures the transmitted intensity (It). A third ionization chamber is also used at the end for measuring spectra of reference foils to carry out corrections in energy calibration of the monochromator. It is also possible to carry out measurement in fluorescence mode in this beamline and a Lytle-type ionization chamber based detector or a Si drift solid state detector is used for this purpose which is placed in front of the sample in a 45° geometry. This beamline is useful for measurement on dilute samples and on thin film materials deposited on thick substrates [6]. In both the above beamlines EXAFS measurements can be carried out over a wide temperature range from 10K to 1000K.

Results and Discussion

EXAFS has been applied to a wide variety of materials having important technological applications in various fields. For example, this technique has very effectively been
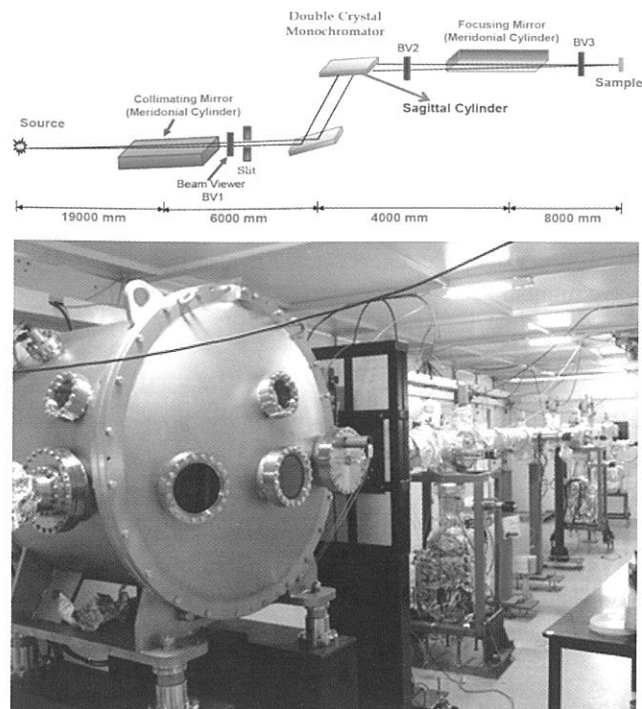
Fig. 3 (a) Schematic Optical Lay-out and (b) Photograph of the energy scanning EXAFS Beamline.

used in studying doping of trivalent atoms in ZrO_2 system and in monitoring creation of oxygen vacancies. ZrO_2 has catalytic applications, either as supports or as electrolytes, especially in solid oxide fuel cells (SOFCs). It exhibits high anionic conductivity when doped with aliovalent cations which facilitates the generation of oxygen ion vacancies for charge compensation. There are contradictions in the literature regarding the possible positions of oxygen vacancies created in ZrO_2 matrix when doped with trivalent ions. We have looked into the above issue using synchrotron based EXAFS technique, where measurements have been carried out on ZrO_2 samples doped with Gd, Nd and La. Data analysis from EXAFS measurements showed that maximum oxygen vacancies in ZrO_2 host matrix are created near the Zr site for Gd doping while Nd and La dopant atoms having relatively larger ionic radii compared to Zr ion, generate lesser number of oxygen vacancies that are located near the dopant cations. Subsequent experiments with ZrO samples having variable Gd doping concentration and simultaneous measurements at Gd and Zr edges confirmed that ~9% Gd doping is optimum for creation of vacancies near the Zr sites and hence for increasing its ionic conductivity [7,8].

Luminescent nanomaterials are another class of materials which have also been characterized very thoroughly by EXAFS technique in the above beamlines BL-08 and BL-09. For example, layered structure of highly crystalline orthorhombic GaOOH nanorods undergo significant lattice distortions leading to amorphisation even when very small amounts of Eu^{3+} ions (1 at.% or more) are present during its synthesis. However, interestingly EXAFS spectra of these samples measured at Ga edge indicate that

the local short range order around Ga^{3+} is unaffected by the incorporation of Eu^{3+} ions in the sample. The best fit results of EXAFS data also indicate that Eu^{3+} do not replace Ga^{3+} but the disorder factor increases appreciably even with the introduction of a small amount of Eu^{3+} (0.5%) and reaches a maximum for 1 at.% Eu^{3+} doping. Supporting information from vibrational studies reveal systematic appearance of new peaks which can be attributed to the bending vibrations of the OH groups associated with $Ga(OH)_3$ and $Eu(OH)_3$ phases which finally leads to the breakdown of the crystalline structure of the materials [9]. In case of Eu doped $SrSnO_3$, another luminescent material, however, Sr K-edge (16105 eV) EXAFS measurements show that the average Sr-O bond distance is higher for Eu^{3+} containing sample compared to the undoped $SrSnO_3$. The increase in bond length can be described in terms of the substitution of a larger cation (Sr^{2+}) by a smaller one (Eu^{3+}). There is a change in luminescent pattern of $SrSnO_3$ with increase in Eu doping concentration which could be correlated to the change in structural symmetry around Sr ions due to Eu doping as obtained from EXAFS measurements [10]. EXAFS measurements have also been carried out on Uranium doped pyrophosphate ($Sr_2P_2O_7$) system where time resolved photoluminescence measurements suggested the stabilization of the actinide ion in uranyl form at the two lattice positions of the two types of Sr ion. From the Sr-K edge EXAFS data it was observed that on doping with uranium, the average Sr-O and Sr-P bond lengths are increased confirming the incorporation of the actinide ion at regular lattice positions of Sr ion [11]. Another luminescent material viz., $CaWO_4$ nanoparticles synthesized at room temperature and subsequently heat-treated at different temperatures (300°C, 500°C, 700°C and 900°C) in air for 5 hours have been characterized by W L_1 edge XANES and W L_3 edge EXAFS measurements. It has been observed that the luminescence of the nanoparticles and associated lifetime increase with increase in the annealing temperature. As has been discussed above, emission in $CaWO_4$ is attributed by various authors to localized bands arising due to oxygen vacancy complexes or distorted WO_4 tetrahedra. The presence of the pre-edge peak of considerable intensity in all the samples confirms that W in $CaWO_4$ exists as WO_4 tetrahedra whereas EXAFS data analysis shows that oxygen coordination number decreases gradually for samples with increase in annealing temperatures. Thus from the above studies we could conclude that WO_4 tetrahedron is unaffected by annealing whereas oxygen vacancies are created in the lattice and these are responsible for the increase in luminescence intensity and associated increase in the lifetime values in the samples [12]. Another system which has recently been investigated by us is bulk and nanoparticles of $Y_2Sn_2O_7$ which is also a host material for doping luminescent lanthanide and transition metal ions. It has been observed that the luminescence from these materials strongly depends on the local environment surrounding the Ln^{3+} ions which in turn depends on the local environment around Y^{3+} and Sn^{4+} ions. X-ray diffraction technique, which acts on the principle of long range order, is not particularly suitable for nanoparticles, and hence EXAFS which basically probes the local order and does not depend on the long range order can yield better result so far as microscopic structural investigation is concerned. EXAFS measurements were carried out at Y K edge on the as-prepared $Y_2Sn_2O_7$ samples and samples heat treated at temperatures of 700°C, 900°C and 1300°C. From TEM studies it has been observed that the as-deposited samples are amorphous and upon heating at 700°C, $Y_2Sn_2O_7$ nanoparticles with size in the range of 2-5 nm is formed, the particle size increase with increasing the annealing temperature to 900°C and this phase gets converted to bulk $Y_2Sn_2O_7$ upon further heat treatment at 1300°C. It has been observed from EXAFS measurements that for the heat treated samples, the Y-O bond length of 2nd oxygen shell surrounding Y increases with increase in the annealing temperature which suggests that Y-O bond is more covalent in nanoparticles compared to bulk and such changes in the ionic or covalent character of Y-O bond also affects the nature of Sn-O bonds in the samples. From the Raman spectroscopic investigations also, it becomes clear that the electronic environment around Sn in nanoparticles is asymmetric compared to that in bulk and first principle calculations show that the electron density is symmetrically distributed around Y^{3+} and Sn^{4+} ions in case of bulk sample while the charge distribution is asymmetric and more diffused for nanoparticles [13].

Another interesting application of the EXAFS technique is to study transition metal (TM) doped dilute magnetic semiconductor (DMS) nanoparticles like ZnO where origin of ferromagnetism (FM) is still a fairly unresolved question. We have carried out a systematic local structure investigation of Co and Mn doped ZnO nanocrystals (NCs) by synchrotron-based EXAFS technique at both Zn K edge and dopant (Co, Mn) K edges at the above beamlines. The measurements have been carried out on samples prepared by different methods, viz., high temperature wet chemical method (WC samples), sol-gel route (SG samples) and the microwave-assisted (MW samples) method with TM dopant concentrations varying from 0-15% by weight. The EXAFS results presented here have been supported by XRD and magnetization measurements and are also confirmed by first principle calculation results. The findings indicate that doping levels of ≤10% of Co is optimum for efficient doping in ZnO lattice above which there is a possibility of Co clustering in the sample. XANES measurements at Co K-edge confirmed presence of Co^{2+} state in the lattice and ruled out the presence of any other secondary phase in the lattice which can give rise to the FM in the sample. The magnetic measurements indicate that, while WC and SG Co doped samples show ferromagnetism which increases in Co concentration, MW Co doped samples are not ferromagnetic. First principle calculations indicate that at high concentration, the dopants tend to cluster together to lower the energy or to increase the stability of the system. In case of Co clustering the system

can either be ferromagnetic or anti-ferromagnetic. Since the WC and MW Co doped samples show similar behaviour in EXAFS measurements, it establishes that FM in WC Co doped samples may be a consequence of charge redistribution due to the presence of organic capping molecules during synthesis. The SG Co doped samples exhibit weak ferromagnetism and EXAFS measurements suggest that oxygen vacancy-assisted bipolarons are responsible for the FM in this system. Mn edge XANES spectra revealed that Mn in WC samples is in +3 state showing presence of Mn_2O_3 phase whereas Mn in MW samples is in +2 state. A doping concentration of <10% for WC samples and <7% for MW samples are found to be optimum beyond which Mn clustering sets in. From magnetic measurements it has been found that WC Mn doped samples, show ferromagnetism which decreases with increase in Mn concentration and MW Mn doped samples demonstrate anti-ferromagnetic ordering. First principle calculations indicate Mn clusters preferentially assume anti-ferromagnetic ordering. The above studies conclusively establishes that a secondary Mn_2O_3 phase detected in WC Mn doped samples, is the reason of FM in these samples while the MW samples show anti-ferromagnetism due to Mn clustering. Hence the above comprehensive study has been able to throw some light regarding the origin of magnetism in TM doped DMSs and the different mechanisms (substitution and site-disorder) for the origin of magnetic properties [14,15].

Layered oxides of the series $InGaO_3(ZnO)_m$ (m=1-4) have interesting anisotropic structure with potential in many applications. X-ray diffraction studies have explained the structures as Zn/GaO_x polyhedra separated by InO_6 octahedral layers. However, there is not enough clarity regarding the exact geometries of Zn or Ga, since the above mentioned techniques provide an average structure. Understanding local environments of Zn and Ga is necessary for further enhancing the applicability of these materials. EXAFS studies point to a gradual shift in coordination from penta to tetra-coordination as we go across the series which indicates that the sandwich layer assumes the structure of ZnO with corner shared tetrahedra as the layer number increases pointing to a possibility of gallium oxide solubilising in this layer. It is possible that Ga which would otherwise be comfortable in penta coordination is now forced into a tetrahedral geometry. This also suggests that any possible doping in the sandwich layer can be made with ions which can readily assume tetrahedral geometry. Such doping strategies may further help in enhancing the generation and conduction of electrons and the concept of spatial separation. EXAFS measurements have also been carried out on structurally analogous compound of $InFeO_3(ZnO)_m$ which is found to be highly active in H_2 generation from water-methanol mixtures. EXAFS data analysis reveals that Zn coordination changes from penta-coordinated to tetrahedral geometry across the series whereas Fe geometry remains trigonal bipyramidal in all the compounds. This peculiar structure is conducive for a spatial separation of photogenerated charges reducing recombination losses. Band gap energies calculated from absorption spectra indicate potential visible light activity and this may be due to the orbital mixing of Fe3d and O2p as revealed by pre-edge features of the XANES spectra of the samples. Band positions are also advantageously placed for a visible light H_2 generation and is indeed found to be the case in methanol assisted water splitting with standardised hydrogen evolution of ~19.5 mmol $g^{-1}h^{-1}$ for all the catalysts [16,17].

References

[1] X-Ray Absorption Fine Structure (XAFS) Spectroscopy – A Review, A. Gaur, B. D. Srivastava and H. L. Nigam, Proc Indian Natn. Sci. Acad. 79 (2013) 921.

[2] The EXAFS family tree: a personal history of the development of extended X-ray absorption fine structure, F.W. Lytle, J Synchrotron Radiat. 6 (1999) 123.

[3] X-Ray Absorption: Principles, Applications, Techniques of EXAFS, SEXAFS and XANES, edited by D.C. Konigsberger and R. Prince (Wiley, New York, 1988).

[4] Analysis of multiple-scattering XAFS data using theoretical standards, M. Newville, B.Ravel, D. Haskel, J.J. Rehr, E.A. Stern, and Y. Yacoby, Physica B 208-209 (1995) 154.

[5] First Results from a Dispersive EXAFS beamline developed at INDUS-2 Synchrotron Source at RRCAT, Indore, India, D.Bhattacharyya, A.K. Poswal, S.N. Jha, Sangeeta and S.C. Sabharwal Nuclear Instruments Method. in Phys. Res. A 609 (2009) 286.

[6] A comprehensive facility for EXAFS measurements at the INDUS-2 synchrotron source at RRCAT, Indore, India, S. Basu, C. Nayak, A. K. Yadav, A. Agrawal, A. K. Poswal, D. Bhattacharyya, S. N. Jha and N. K. Sahoo, Journal of Physics: Conference Series 493 (2014) 012032.

[7] X-ray Absorption Spectroscopy of doped ZrO2 systems, S. Basu, Salil Varma, A. N. Shirsat, B.N. Wani, S. R. Bharadwaj, A. Chakrabarti, S.N. Jha and D. Bhattacharyya, J.Appl. Phys., 111 (2012) 053532.

[8] Extended X-ray Absorption Fine Structure (EXAFS) study of Gd doped ZrO_2 systems, S. Basu, Salil Varma, A. N. Shirsat, B.N. Wani, S. R. Bharadwaj, Aparna Chakrabarti, S.N. Jha and D. Bhattacharyya, J. Appl. Phys 113 (2013) 043508.

[9] Lanthanide ions assisted structural collapse of GaOOH nanorods: Probed through EXAFS and vibrational techniques, S. Basu, B. S. Naidu, M. Pandey, V. Sudarsan, S. N. Jha, D. Bhattacharyya, R. K.Vatsa, and R. J. Kshirsagar, Chem. Phys. Lett. 528 (2012) 21.

[10] Probing local environments in Eu3+ doped SrSnO3 nano-rods by luminescence and Sr K-edge EXAFS techniques, S. Basu, D. K. Patel, J. Nuwad, S. N. Jha, D.

Bhattacharyya, V. Sudarsan, R. K. Vatsa and S. K. Kulshreshtha, Chem. Phys. Lett. 561–562 (2013) 82.

[11] Local structural investigations and speciation of uranium in $Sr_2P_2O_7$ by time resolved emission spectroscopy and Sr K-edge EXAFS, Manoj Mohapatra, A. K. Yadav, S. N. Jha, D. Bhattacharyya, S. V. Godbole and V. Natarajan, Chem. Phys. Lett., 601 (2014) 81.

[12] Effect of oxygen coordination on the luminescence properties of $CaWO_4$ particles, S. Basu, Boddu Sanyasi Naidu, B. Viswanadh, V. Sudarsan, S.N. Jha, D. Bhattacharyya and R. K. Vatsa, RSC Adv. 4 (2014) 15606.

[13] Nano-size effects on the nature of bonding in $Y_2Sn_2O_7$: EXAFS and Raman spectroscopic investigations, C. Nayak, Sandeep Nigam, M. Pandey, V. Sudarsan, C. Majumder, S. N. Jha, D. Bhatacharyya, R. K. Vatsa and R. J. Kshirsagar, Chem. Phys. Lett. 597 (2014) 51.

[14] Structural, optical and magnetic properties of sol-gel derived ZnO:Co diluted magnetic semiconductor nanocrystals: An EXAFS study, Shiv Kumar, S. Basu, B. Rana, A. Barman, S.

Chatterjee, S.N. Jha, D. Bhattacharyya, N.K. Sahoo and Anup K. Ghosh, Journal of Mater. Chem. (C) 2 (2014) 481.

[15] Local Structure Investigation of Co and Mn Doped ZnO Nanocrystals and its Correlation with Magnetic Properties, S. Basu, D. Inamdar, S. Mahamuni, A. Chakrabarti, C. Kamal, G. Kumar, S.N. Jha and D. Bhattachharya, The Journal of Physical Chemistry, Part C 118 (2014) 9154.

[16] Investigations into variations in local cationic environment in layered oxide series $InGaO_3(ZnO)m$ (m=1-4), Soumya B. Narendranath, Ashok Kumar Yadav, T.G. Ajithkumar, Dibyendu Bhattacharyya, Shambu Nath Jha, Krishna K. Dey, Thirumalaiswamy Raja and R. Nandini Devi, Dalton Transaction 43 (2014) 2120.

[17] Photocatalytic H_2 evolution from water-methanol system by anisotropic $InFeO_3(ZnO)m$ oxides without cocatalyst in visible light, Narendranath, Soumya, Yadav Ashok, Bhattacharyya Dibyendu, Jha Shambu Nath, Devi R. Nandini, ACS Applied Materials & Interfaces 6 (2014) 12321.

Ms. Chandrani Nayak *joined the Atomic and Molecular Physics Division of BARC in 2012 after completion of her M. Sc. in Physics from IIT Bombay and one–year Orientation Programme at BARC Training School (55th Batch). She has been involved in the Extended X-ray Absorption Fine Structure (EXAFS) measurements of various technologically important materials using the Energy Dispersive and Energy Scanning EXAFS beamlines at INDUS-2 Synchrotron Radiation Source (SRS) at RRCAT, Indore.*

Shri Ashok Kumar Yadav *joined the Atomic and Molecular Physics Division of BARC in 2011 after completion of his M.Sc. in Physics from University of Delhi and one–year Orientation Programme at BARC Training School (54th Batch). He has been involved in installation and commissioning of energy scanning EXAFS beamline at INDUS-2 SRS at RRCAT, Indore. Presently he is actively involved in the EXAFS measurements of various technologically important materials using the EXAFS beamlines at INDUS-2 SRS.*

Ms. Sohini Basu *completed her Master's degree in Physics in 2009 from University of Calcutta. She did her PhD work in the area of X-ray Absorption Fine Structure spectroscopy (XAFS) under the supervision of Dr. D Bhattacharyya at the Atomic and Molecular Physics Division, BARC. Presently she is working as a Senior R&D Engineer in the Research and Modeling Group of UOP, A Honeywell Company in Gurgaon, Haryana.*

Dr. Parasmani Rajput *did her PhD from UGC-DAE Consortium for Scientific Research, Indore and worked as a post-doctoral scientist at the European Synchrotron Radiation facility (ESRF) in Grenoble, France and at Northwestern University, Evanston, IL, USA. In 2013, she joined Atomic and Molecular Physics Division of BARC and is working in the XAFS group stationed at RRCAT, Indore. Her present scientific interest includes interface study of thin films/magnetic multilayer of metals/oxides, corrosion study of noble metal alloys and Li-ion battery.*

Shri Ankur Agrawal *obtained B. Tech. in Electronics and Communication Engineering from SASTRA University, Thanjavur, in 2008 and joined the 52nd batch of BARC Training School at Mumbai. After his joining Atomic and Molecular Physics Division of BARC, he completed M.Tech. degree in Electronics Engineering from HBNI, Mumbai with specialization in Nuclear Engineering. Shri Agrawal is stationed at RRCAT, Indore since 2009 and is involved in the design, development and implementation of the control and data acquisition systems for various beamline components and their interfacing and synchronization.*

Shri Ashwini Kumar Poswal had joined Atomic and Molecular Physics Division of BARC after completing the one-year Orientation course of BARC Training School. He had been involved in the development, installation and commissioning of the Energy Dispersive and Energy Scanning EXAFS beamlines at INDUS-2 Synchrotron Radiation Source. He has been active in the development and implementation of various modules in the beamlines in order to achieve better data quality and resolution.

Dr. D. Bhattacharyya had joined the erstwhile Spectroscopy Division of BARC in 1997 after completing his PhD work from Indian Association for the Cultivation of Science, Kolkata and Post-doctoral work at the University of Northumbria, Newcastle Upon Tyne, U.K. He is presently heading the Synchrotron Science and Multilayer Physics Section of Atomic & Molecular Physics Division, BARC. Dr. Bhattacharyya has more than 105 publications in international journals. He is a recipient of DAE Scientific and Technical Excellence Award in 2009 and DAE–SRC Outstanding Investigator Award in 2012.

Dr. S.N. Jha had joined the erstwhile Spectroscopy Division of BARC in 1989 after completion of M.Sc. (Chemistry) from University of Delhi and one–year Orientation Programme at BARC Training School (32nd Batch). He obtained Ph.D degree from Mumbai University in 1999 in the field of X-ray spectroscopy and instrumentation. Dr. Jha is presently the Head of the Beamline Development and X-ray Application Section of Atomic and Molecular Physics Division, BARC. His current research interests include EXAFS and PES spectroscopy using synchrotron radiation source.

Dr. N.K Sahoo is presently heading the Atomic and Molecular Physics Division at BARC. He did his post-graduation from Utkal University and one-year Orientation programme of BARC Training school. He obtained Ph.D degree in Thin Film Physics from University of Mumbai and subsequently carried out post-doctoral research at NASA/Marshall Space Flight Center, Huntsville, USA. He has steered several important programmes of BARC-DAE, namely, (i) establishing spectroscopic synchrotron beamlines in Indus-1 and Indus-2 synchrotron radiation sources, (ii) thin film multilayer coating facilities for lasers and synchrotrons, (iii) development of optical and analytical instruments, (iv) establishing Optics, Photonics and (v) Thin film laboratory at BARC-Vizag. He has more than 200 publications in international journals and proceedings.

Positron Spectroscopy: From Nanostructures to Large Engineering Materials

P.K. Pujari

Radiochemistry Division, Bhabha Atomic Research Centre, Trombay, Mumbai 400 085; E-mail: pujari@barc.gov.in

Positron is an anti-particle of electron. It annihilates with an electron producing photons. If the positron and electron meet with their spins parallel, that is triplet interaction, three annihilation photons are emitted. Singlet or two photons mode is, however, most predominant and the photons (511 keV each) are emitted in opposite direction for conservation of spin and momentum. Direct information about electron momentum distribution and electron density can be obtained by monitoring these photons. In materials, positron has high propensity for open volume defects because it experiences less repulsion compared to bulk due to the absence of the positively charged nuclear core. This sensitivity of positrons to open volume defects has made it a very popular and powerful probe in characterizing defects, its sensitivity extending from as small as a monovacancy and to a few ppm concentrations. In molecular solids positron can form a quasi bound state with an electron producing Positronium (Ps) atom which has similarity with hydrogen atom. Depending upon the spin alignment, either parallel or antiparallel, two types of Ps atoms are formed, ortho-Ps (o-Ps) or Para-Ps (p-Ps), respectively. The latter is short lived (125 ps) while the o-Ps lives long enough (142 ns) to interact with its chemical surrounding and provides valuable physico-chemical information. This branch of science is known as Ps-chemistry.

Positrons can be obtained from radioactive sources (^{22}Na) or through pair production using high energy gamma-rays. Upon implantation into a material, positron thermalises in a few ps, short enough compared to its life-time of a few hundreds of picoseconds. Therefore, the momentum of the electron-positron pair during annihilation is primarily due to the electron. In order to conserve this momentum, following annihilation, the pair of annihilation photons deviates from anticollinearity (opposite direction) and the extent of deviation is a measure of the electron momentum. The technique for measuring this deviation, hence the electron momentum distribution is known as angular correlation of annihilation radiation (ACAR) technique. Similarly, since the annihilation gamma rays are emitted from the positron-electron pair in-flight, there is Doppler broadening of the measured gamma lines. The extent of the Doppler broadening, therefore, is a measure of the momentum of the electrons in the material. This technique is known as Doppler broadened annihilation radiation (DBAR) measurement technique. The resolution of ACAR is certainly superior to DBAR. However, if the Doppler spectrum is measured in coincidence mode, known as 2D-DBAR, there is considerable improvement in resolution in addition to several other advantages in extracting information especially the chemical surrounding

at the annihilation site. The annihilation rate is proportional to electron density. The life-time of the positron or how long the positron survives in a medium gives direct information about the electron density. A suitable tag following the birth of the positron (typically 1275 keV gamma line in ^{22}Na) is recorded. The annihilation photon (511 keV) signals the decay of the positron. The time difference between the birth and death of the positron is measured electronically and its distribution is the life-time spectrum. This technique is known as Positron life-time spectroscopic technique. Positron trapped in an open volume defect would experience lower electron density compared to the one in the bulk of the material altering (increasing) its life-time. The momentum distributions also get modified in the case of positron trapping in defects. This is the basic principle of defect spectroscopy and applicable for both the free positron as well as Ps atom (in molecular solids)

Globally the major areas of research using positron technique are as follows. First, condensed matter physicists dealing with electronic structure of materials used ACAR (one or two dimensional) extensively to elucidate the Fermi surface. The second major area is the understanding of material properties through defect characterization in virtually all type of materials. The third major area is positronium chemistry that deals with understanding the formation systematics of Ps atom and its reactivity under different physico-chemical conditions. Once the behaviour of Ps is understood in a given medium, it can be utilized to probe several other aspects of that medium. These media have been polymers, catalysts, porous materials, micelles and many other chemical systems. The fourth area is monoenergetic slow positron accelerators and associated developments. Positrons from radioisotope sources have a broad energy distribution and it is difficult to obtain depth dependent information. Also study of thin films (nanoscale) is not possible with isotope source. Monoenergetic beam of positrons can be used to depth profile the defects in a given material, thick or ultrathin film, as the case may be. Development of positron beam has also led to substitution of conventional electron spectroscopies with positrons e.g. scanning positron microscope, positron induced Auger electron spectroscopy (PAES), positron energy loss spectroscopy (PELS) are now realities. Intense positron beam has helped in the discovery of dipositronium atom and attempts at producing antihydrogen [1-4].

In Radiochemistry Division, the main area of research has been defect spectroscopy, Ps chemistry especially elucidation of nanostructure in polymers and its correlation with physico-chemical properties, studies in porous materials, positron dynamics in nanomaterials as well as
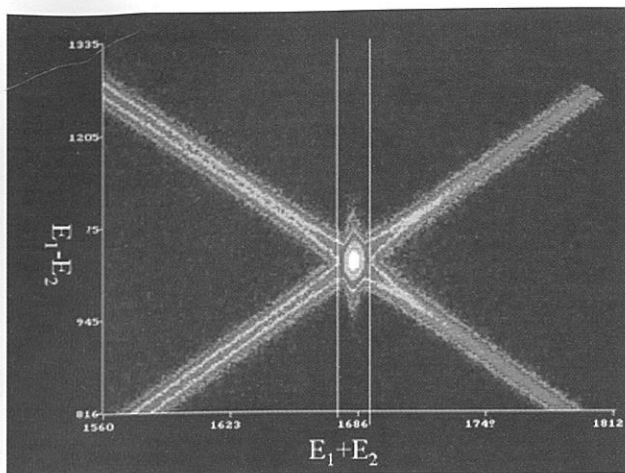
Fig. 1   A typical 2D-Doppler or CDB spectrum showing the sum and difference in the energy of annihilation gamma-rays. The y-projection of the bracketed region provides near background free Doppler spectrum

Fig. 2   A typical 3D-AMOC spectrum in polymer.

Fig. 3   The Slow Positron Accelerator at Radiochemistry Division (SPARC). Positrons are moderated by W(100) film and focused by a electrostatic lens. Transport to target is by a solenoid and pair of Helmholtz coils. Acceleration is achieved by floating the target ladder

nanostructures using slow positron beam. While nanostructures (ultrathin films) can be studied by slow positron beam, volumetric assay of defects in thicker (few inches) samples cannot be studied by conventional techniques using radioisotope source or positron beam. This is because of the fact that the penetrability of the available positrons is limited to millimeters range. Therefore, we have developed a technique called Photon Induced Positron Annihilation Spectroscopy (PIPA) that utilizes in situ positron formation through pair production using high energy gamma rays. These high energy gamma rays are produced through suitable nuclear reaction at FOTIA, BARC. A description of facilities built over the years and some highlights of our work is given in the following.

Facilities

Over the years, various facilities pertaining to positron annihilation spectroscopy (PAS) have been developed at BARC. The neutron deficient radioisotope ^{22}Na is the most commonly used source of positrons for laboratory studies. Conventional facilities include positron lifetime and Doppler broadened spectrometers. The two detector coincidence Doppler broadening (CDB) facility, which reduces the background in the higher momentum region of the annihilation spectra and thereby enables the identification of elements around the annihilation site of positron, has been developed and utilised. A typical photograph of the CDB spectrum is shown in Fig.1. Positron Age-Momemntum Correlation (AMOC) technique provides correlated information on positron age and corresponding momentum distribution. AMOC instrument has been developed that involves three detector coincidence measurement of two annihilation photons and 1275 keV gamma line from the positron source. It helps in unambiguous interpretation of positron/Ps states and helps in elucidating Ps reac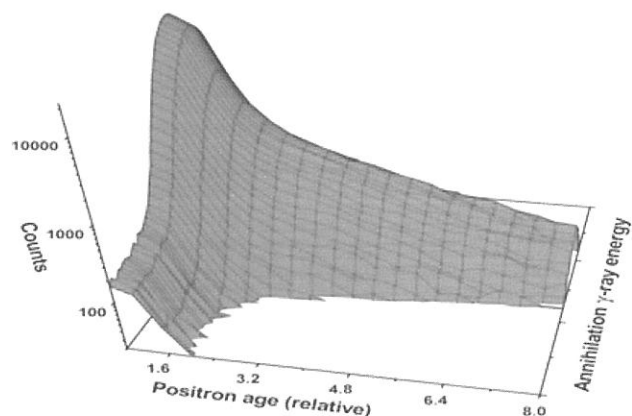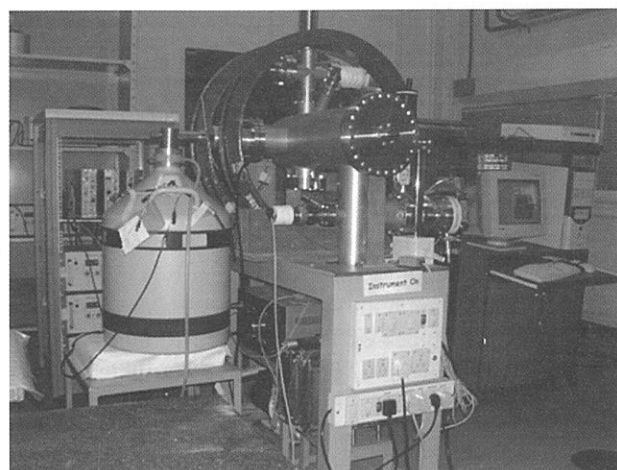tion mechanism in chemical media. A typical three dimensional AMOC data in polymer is shown in Fig. 2. A slow positron beam based on moderation, extraction using Einzel lens, transport using a solenoid and acceleration by floating the target is developed for depth profiling studies especially in nanostructured materials. The photograph of the slow positron accelerator at Radiochemistry (SPARC) Division is shown in Fig. 3. A pulsed positron beam with radio-frequency based chopper, prebucher and buncher is under development. To extend our scope of studies from nanostructures to non-destructive assay of defects in large engineering materials photon induced positron annihilation spectroscopy system (PIPA) has been set up at FOTIA. A photograph of the PIPA facility at FOTIA is given as Fig. 4. MIKA-DOPPLER and Vienna ab initio Simulation Package (VASP) are routinely used to complement the experimental results.

Fig. 4 Photograph of Photon Induced Positron Annihilation (PIPA) facility at FOTIA for volumetric assay of defects in large engineering materials

Research

Positron Annihilation in High T_c Superconductors (HTSCs)

The initial studies using PAS were carried out on the HTSCs [5-11]. The studies in YBCO have revealed electronic-structural changes at the onset of superconductivity and the possible presence of oxygen dimmers, and, electron density change in copper-oxygen planes. In BSCO, evidence for local charge-transfer process from CuO_2 to Bi-O planes at the onset of the superconductivity has been seen. In MgB_2 superconductors, the studies have revealed for the first time that the boron layer is electronically active at the onset of superconductivity and the nature of superconducting transition has a striking resemblance to HTSCs [5].

Positron Annihilation Studies in Polymers

The intrinsic lifetime of o-Ps is reduced from 142 ns in a medium by a process called pick-off annihilation. The pick-off annihilation rate depends on the free volume hole radius/pore size in polymers and porous materials. Hence, the positron annihilation lifetime technique has been the most successful technique for studying the free volume holes in polymers. The positron annihilation lifetime studies have been carried out on Nafion-117 to understand the microstructure under different conditions such as water content, counter ion, solvent, temperature etc. The free volumes in Nafion were found to be in hydrophobic region. The changes in the free volumes with the solvent and extent of solvation, quantitative correlations between cluster volume and free volume fraction in the Nafion with different counter ions have been obtained. There was unique correspondence between gas diffusion and the free volume hole fraction in dry state. The temperature dependent relaxation studies revealed a new transition at 140K for the

first time [12-14]. N-Isopropyl acrylamide gels (NIPA) polymerized using electron beam, gamma irradiation and UV radiation with different cross linkers etc. have been studied. NIPA with inhomogeneous cross linking or broader distribution of free volumes was found to show faster swelling kinetics and higher water uptake [15-17]. The free volumes in the fluorinated ethylene propylene copolymer grafted with polystyrene reduced the free volumes and increased the gas separation factors. The free volumes were also found to be directly correlated with other physico-chemical properties in these membranes [18,19]. The free volume parameters in poly ethylene tere phthalate (PET) –g-acrylic acid copolymer were observed to follow a simple mixture rule and showed a direct correlation with structural transitions as studied using dynamical mechanical analysis [20]. A comprehensive study of structural relaxations of epoxy poly-ether amine networks using varieties of techniques including PALS confirmed the fluctuational nature of networks influenced by sub T_g transitions [21]. Slow positron beam based depth profiling study of track etched PET membranes prepared using low fluence irradiation has confirmed the sensitivity of positron based techniques over other techniques for the characterization of microstructure at sub surface regions [22].

Positron Annihilation Studies in Polymer Nanocomposites

Polymer nanocomposites are multiphase materials having one or more nanocrystalline phases dispersed in a polymer matrix. The sub nano level structure of polymer phase changes as a result of dispersion of nanocrystalline phases and mainly depends on the interaction between polymer molecules and the nanocrystalline phase. Positron/positronium have been used as an efficient probe to investigate such changes in polymer nanocomposites and efforts have been made to correlate these changes with the evolved properties of nanocomposites. The studies on phenolformaldehyde–multi wall carbon nanotubes (MWCNTs) and epoxy-clay composites showed the increase in free volume fraction due to weak interaction between polymer molecules and nanofillers. These studies also confirmed that positron/positronium systematics is altered in the presence of nanocrystalline phases in polymer matrix [23,24]. Positron annihilation studies in chitosan-NiO nanocomposites indicated the creation of an interphase region which has a different nanostructure compared to bulk chitosan [25]. PALS measurements showed that an ordered arrangement of poly-vinylalcohol (PVA) molecules is formed at the surface of amino functionalized MWCNTs leading to efficient load transfer from PVA matrix to MWCNTs which results into superior mechanical properties of the nanocomposites [26].

Studies in Porous Materials

Positron is an in situ probe in porous materials. The o-Ps lifetime is directly related to the pore size and it can probe open as well as hidden (blocked) pores. The intensity

of the o-Ps is directly proportional to the surface area. Ps is the smallest probe and provide information on pore sizes in the range of 2-5 Å where the techniques like BET fail due to the dimension of the adsorbates used. The positronium lifetimes in mesoporous materials have been measured. It has been established that the pore size distributions, three photon detection probabilities in the positronium lifetime measurement and quenching of Ps in air could be some of the reasons for the differences in o-Ps lifetimes [27-30]. A model to relate the o-Ps lifetimes with pore size in the mesoporous materials has been given [27]. In a recent study, a direct evidence of formation of NiO/MgO solid solution layer over MgO grains has been provided by AMOC measurements on MgO-NiO catalyst samples [31].

Defect Studies in Zr Based Alloys

It is well established that in Zr alloys, secondary phase precipitates (SPP) have a major influence on the corrosion and mechanical properties. Thus it is important to understand the kinetics and growth of precipitates under thermal treatments. In our study, secondary phase precipitates were generated by suitable heat treatment at 800°C and 840°C for different duration (1-1440 minutes). Positron lifetime spectroscopy and Doppler broadening measurements were carried out to examine the nucleation and growth aspects of the precipitates. The variation in lifetime and S-parameter were seen to be consistent. Grain coarsening reduces the life-time and S-parameter while nucleation enhances these parameters due to generation of interfaces. Annealing at 800°C revealed smaller precipitates and continuous nucleation at least up to 5 h. On the other hand, annealing at 840°C produces small number of precipitates with larger size. The nucleation is predominant between 1 to 2 h following which coarsening and nucleation coexist. In both the temperatures, the 24 h annealed sample shows formation of incoherent precipitates. The defects and/or interfaces between the precipitate and matrix were seen to be different in samples treated at 800 and 840°C. Recrystallization behavior in Zr 2.5%Nb alloy was studied using positron spectroscopy supplemented by Orientation Imaging Microscopy (OIM) and Transmission Electron Microscopy (TEM). The two phase alloy consists of α-fcc and β-bcc. The recrystallization behavior of Zr2.5Nb strongly depends on morphology and distribution of second phase. In this study, the material was deformed to 60% and then was recrystallized in α + β region for different duration (i.e. 2 minutes to 14 days at 700°C). The recrystallized microstructure was characterized by OIM. Results from positron annihilation studies and other microstructural examination have been used to rationalize the recrystallization aspects, defects and β-phase distribution. In early stage of annealing, positron technique is seen to be very sensitive to microstructural changes vis-a-vis OIM. It is also seen to be sensitive to grain growth and phase transformation. 2D-Doppler data unequivocally suggests that the defects are predominantly present in β-phase following deformation [32,33]. In another study on the deformation of Zircaloy-2 using positron and OIM, it was shown that twins greatly influence the dislocation density concentration [34]. Defect studies pertaining to order-disorder transition in CuZnAl have also been reported from our laboratory [35].

In a recent study we have observed a very interesting positron systematics in U-Zr alloys with Zr content varying from 0-10%. CDB measurement shows that all the positrons annihilate with Zr in as-cast alloys. On annealing, the Zr signature vanishes completely despite the fact that both sets of samples have embedded Zr precipitates. We have measured the positron diffusion length using S(E) profile from slow positron beam measurement on these alloys and conjectured the presence of Zr nanoagglomerates (in addition to phase separated Zr precipitates) that act as preferential trapping sites for positrons [36].

Positron Dynamics in Nanomaterials

Nanomaterials like metal, metal oxide nanoparticles and embedded nanocrystals have a large number of applications in different fields such as light emitting diodes, catalysis, gas sensors etc. Opto-electronic, catalytic and mechanical properties of nanomaterials differ from the bulk properties due to large surface to volume ratio and the defects present at the surface as well as bulk of the nanomaterials. Hence, it is very important to characterize the nanomaterials for the defects and examine their role in various properties. For unequivocal interpretation of data, it is essential to simulate the positron behavior in nanomaterials which is being done using MIKA DOPPLER and VASP packages. The former is based on two component density functional theory to calculate the positron lifetime and electron momentum distribution in the bulk lattice and in the presence of defects. For these calculations, the electron density is approximated by the non-self consistent superposition of free atom density i.e. atomic superposition model (ATSUP) under generalized gradient approximation (GGA) scheme. The Schrödinger equation is then solved for the positron Eigen energy and positron wave function using a three dimension real space solver. The Positron lifetime is calculated using the electron density, positron density and the enhancement factor between positron and electron. The defect formation energy and the relaxation of atoms around the defect are calculated using VASP which employs pseudopotential DFT projector augmented wave method.

The PAS studies have been carried out in ZnO nanoparticles having size in the range of 4 – 40 nm [37]. A schematic of ZnO lattice with monovacancy of Zn is shown in Fig. 5. The experimental and the calculated positron lifetimes in ZnO showed that multi-vacancies of Zn and (Zn,O) are the defects produced at the time of synthesis. With the increase in size, these defects first agglomerate and then anneal out of the nanoparticles. CDB measurements also confirmed the presence of multi-vacancies of Zn and (Zn,O) in the nanoparticles. The CDB measurements have been carried out in CdSe nanoparticles. The ratio curves showed a peak having contribution from Cd (4d) and Se (3d) states and
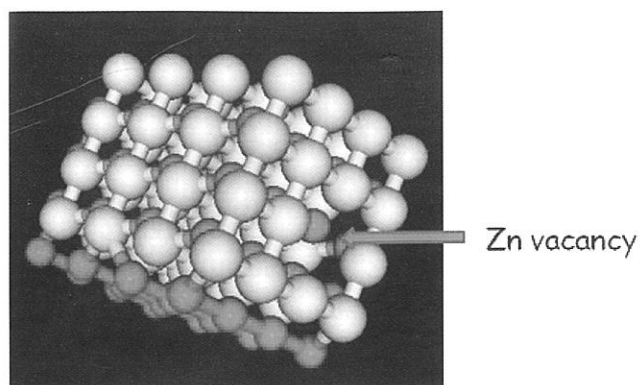
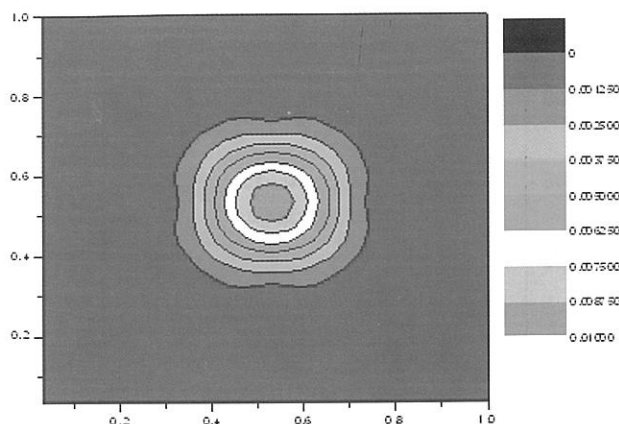Fig. 5   ZnO lattice with monovacancy of Zn

Fig. 6   Calculated Positron density profile in [0 0 1]
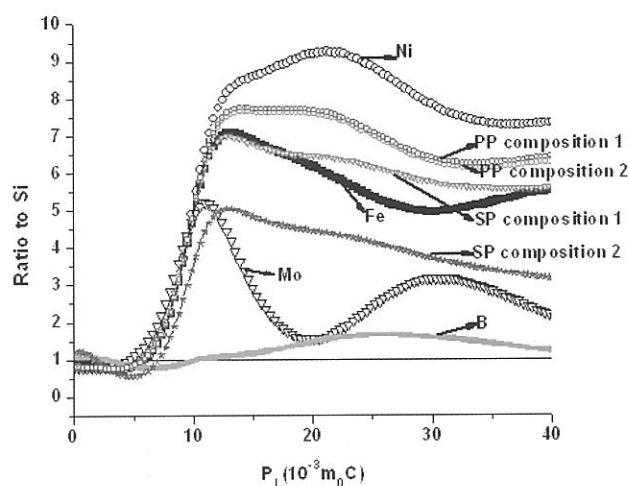

Fig. 7   Theoretically generated momentum distribution of Fe, Ni, Mo, B, and PP, with composition 1 as c-$(Fe_{0.5}Ni_{0.5})$ and composition 2 as c-$(Fe_{0.6}Ni_{0.4})$, and SP with composition 1 as $(Fe_{0.5}Ni_{0.5})_{23}B_6$ and composition 2 as $(Fe_{0.4}Ni_{0.4}Mo_{0.2})_{23}B_6$.[29]

a large fraction of positrons are localized at the surface of the nanoparticles. This also showed that the smallest size nanoparticle has Se rich surface which can be due to the outward relaxation of Se [38].

Gold nanoparticles having average size ~6 nm have been synthesized by one pot synthesis. Two positron lifetime components were observed in the nanoparticles. These two lifetime components are attributed to the defect states as both are higher than the bulk positron lifetime in gold. The theoretically calculated positron lifetimes showed that the first lifetime component corresponds to the Au monovacancy and the second lifetime component arises from a large vacancy cluster. For a vacancy cluster the defect geometry is very important regarding the stability of the defects in the lattice. The positron density profile in [001] plane of Au FCC lattice having Au vacancy at (0.5, 0.5, 1) position is shown in Fig. 6. In the present case, it is seen that the vacancy cluster can be either octavacancy or hexavacancy depending on the geometry. The defect formation energy decides the stability of a defect in the lattice. VASP was used to calculate the formation energy of different defects in Au lattice.

The nanocrystallization behavior of soft magnetic materials such as Metglas 2826MB, $Fe_{68.5}Cu_1Nb_3Si_{18.5}B_9$, $Co_{64.5}Fe_{3.5}Si_{16}B_{14}Ni_2$ and $Zr_{52}Ti1_6Al_{10}Cu_{18}Ni_{14}$ has been studied using PAS [39-43]. The calculated electron momentum distribution (the ratio curve with respect to Si) of the two phases and the Ni, Fe, Mo, and B are shown in Fig. 7 [40,41]. In the case of nanocrystallized samples, it has been demonstrated that small and large lifetime components correspond to positron annihilation with crystalline nanophase and with amorphous-crystalline interface, respectively. Positron lifetime and electron momentum distribution in crystalline phase calculated using MIKA DOPPLER helped in the unambiguous interpretation of the experimental data. The PALS results helped in optimization of the preparation parameters of metallic glasses with the best possible magnetic properties [42].

Phase Transition behavior of Nanodroplets

The freezing/melting behavior of fluids confined in nano pores are significantly altered from their bulk behavior. This phenomenon has great relevance in fundamental research as well as applications in nanotribology, nanofabrication, membrane separation, interfacial adhesion and lubrication. The unusual feature in freezing/melting behavior is mainly due to the contribution of the interfacial surface free energy associated with the interface between the pore wall and liquid or solid in the confinement. The freezing/melting temperature of a liquid inside the pore increases from the normal equilibrium temperature, when the liquid-wall interfacial free energy is higher than the free energy associated with solid-wall interface, and vice versa. The magnitude of the change in the freezing/melting temperature of a confined liquid/solid in a pore is generally obtained by using classical thermodynamics (well-known Gibbs-Thomson equation). However, in the limit of a small and highly inhomogeneous system (nano-pores), where the concept of surface energy is not well defined, a deviation is expected from the classical thermodynamics. Hence, the aim of our study was to investigate the dependence of freezing/melting temperature of liquid on the size of the
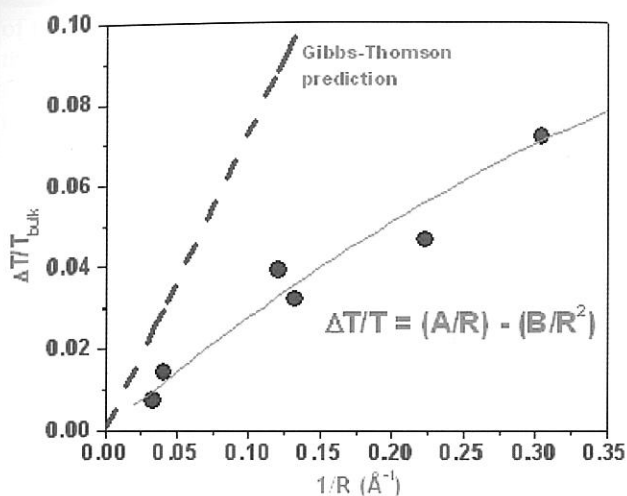
Fig. 8 *Shift in freezing point vs inverse of pore radius. The dashed line shows the calculated shift in freezing point using Gibbs-Thomson equation. The solid circles are obtained experimentally and the solid line is the fit to the experimental data using molecular cluster theory for microcrystal growth.*

Fig. 9 *S-parameter vs temperature for water confined in slit like geometry between clay platelete. The arrow indicates the presence of a high temperature phase transition above bulk freezing temperature*

nano-pore, as well as on the interfacial surface free energy, using PAS.

To explore the effect of pore size, we have studied the freezing/ melting behavior of benzene confined in the nano pores of ZSM5 zeolite and silica powder [44-46]. Benzene molecules feel repulsive/weakly attractive interaction with the surface of the pore, hence a depression in the freezing/melting temperature was observed. The pore sizes were in the range of 0.5-4.0 nm. In this nano domain, it is important to consider the interfacial effects through a description of the confined phase at the molecular level. We have shown that the obtained experimental results were better described by considering the benzene molecules to form small molecular clusters after being frozen in the nanopores. Thus, for the first time, a correlation between the nano pore size and the shifting in freezing/melting point of benzene is obtained, which satisfies molecular cluster theory for microcrystal growth in confined region [Fig. 8].

The effect of interfacial energy has been explored by studying the freezing/melting behavior of two organic liquids namely ethylene glycol and isopropanol confined in nanopores of ZSM5 zeolite [47]. Both the liquids have intermolecular hydrogen bonding and feel attractive interaction towards the surface of the confining wall, resulting in an elevation in the freezing/melting temperature while confined in nanopores. However, the profile of the measured positron annihilation parameters (i.e. Doppler broadening S-parameter, ortho-positronium lifetime and intensity) show quite different behavior across the freezing point in these two confined liquids. This is because the ethylene glycol has strong intra-molecular hydrogen bonding, unlike isopropanol, which causes the difference in the fluid-wall interfacial interaction among these two liquids
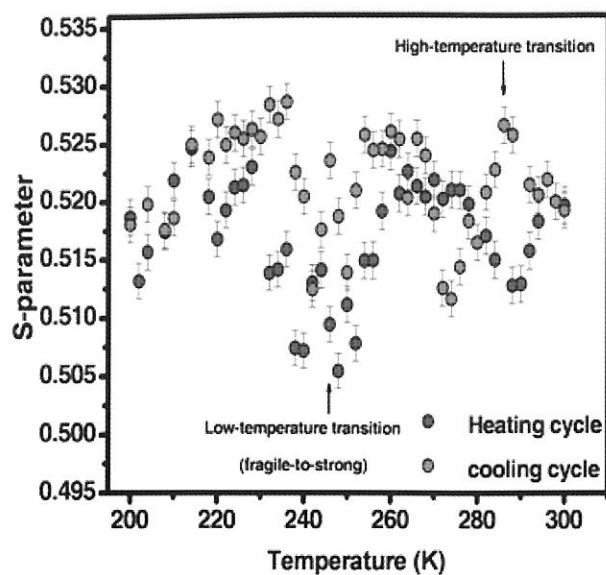
within the confinement. The liquid with both intra and inter-molecular hydrogen bonding (ethylene glycol) showed smaller relative increase in freezing point due to weaker interaction with the pore surface, as compared to the case in isopropanol. The phase transition behavior of these two confined liquids was also complemented using NMR technique by studying the spin-spin relaxation time. The oxygen atoms present on the surface of the void space of ZSM-5 enhances the effect of the interfacial hydrogen bonding, which provides a strong spatial correlation and supports the propagation of surface induced order to the molecules at the centre of the pore. The fluid molecules having strong interaction with the surface of the pore are generally arranged in a layer structure. Hence, the layer like configuration is facilitated in the strongly hydrogen bonded molecules like isopropanol. The ethylene glycol, on the other hand, shows comparatively weaker interfacial attraction due to strong intra-molecular hydrogen bonding and expected to have inhomogeneous phases with globular structure as observed in case of benzene in ZSM5 and silica pores.

The role of interfacial interactions and geometry of confinement has been extended to nanoconfined water. The nanoscale confinement of water and its behaviour has attracted considerable attention due to its relevance to fundamental physics, biological and geological processes as well as technological developments. Nanoconfined water can be supercooled below its freezing temperature and exhibit anomalous properties, which are attributed to the effect of surface interactions that modify the hydrogen-bonded network resulting in the formation of new phases. We have probed structural and dynamical features associated with the phase behaviour of water confined in slit-like pores of clay (2D confined water) using positron
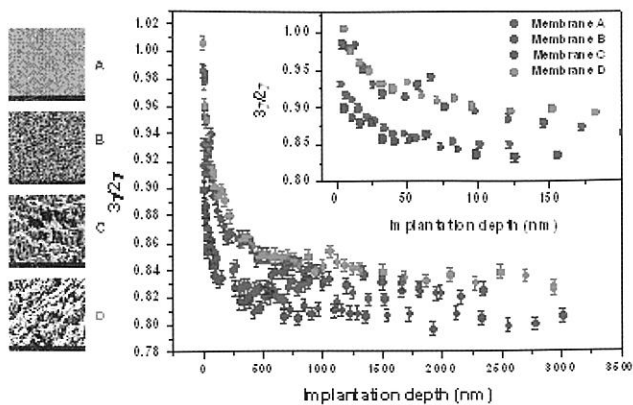
Fig. 10 Sensitivity of 3γ/2γ ratio profiles to open porosity and pore interconnectivity in PTFE membrane and their SEM images.
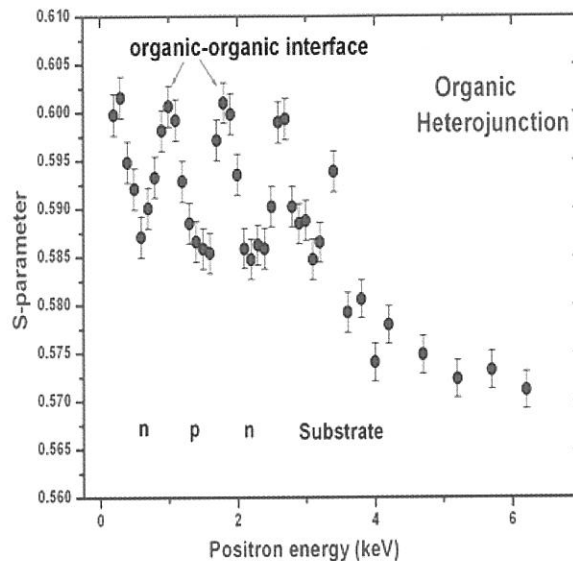

Fig. 11 S-parameter vs depth in a p-n-p organic heterojunction of 30 nm thickness (each layer). Data clearly reveals defects/disorder at the organic-organic and organic-inorganic interfaces

annihilation spectroscopy, NMR and dielectric relaxation spectroscopy techniques. We have reported for the first time, the experimental evidence of a new phase transition (above the bulk freezing point of water) in nanoconfined water, in addition to a low-temperature transition in supercooled water [Fig 9]. The study reveals the high temperature transition to be a structural rearrangement of water molecules associated with modification of hydrogen-bonded network. We have also suggested that the dynamical arrest/immobilization of water layer near the clay platelet surface (bound water molecules) to be associated with this transition. This transition is a manifestation of the role of surface interaction on the phase behaviour of confined liquids [48].

Slow Positron Beam Studies on Nanostructured Films

PAS using monoenergetic positrons has emerged as a sensitive technique to probe atomic level disorders as a function of depth unlike the conventional techniques which give information averaged over the bulk of the material due to the distribution of energy of the emitted positrons. Number of studies ranging from microstructure of membranes in terms of pore architecture to the morphology and defect structure at interfaces have been carried out using slow positron accelerator at Radiochemistry Division (SPARC), BARC. The microstructure of supported liquid membranes has been studied using Doppler broadening spectroscopy wherein, S-parameter and 3γ/2γ ratio have been utilized to calculate the diffusion of positron/ Positronium inside the membrane [Fig. 10]. The variation in S-parameter and 3γ/2γ ratio as a function of depth manifests the pore architecture in terms of pore interconnectivity and tortuosity in the membrane. Pore architecture of the membrane has been correlated to transport properties of the membrane wherein, it has been observed that high pore interconnectivity reflects high tortuosity and this leads to lower permeability through the membranes [49].

Depth profiling by monoenergetic positrons has also been utilized to probe defects especially structural disorder

at the bulk layers and buried interfaces in organic semiconductor (OSC) thin films with thickness ranging from 30-100 nm on a variety of substrates. The performance of organic semiconductors (OSC) is directly related to molecular packing, crystallinity and growth mode. The efficiency and stability of organic devices (organic field-effect transistors (OFETs), organic photovoltaic cells, organic light emitting diodes etc.) critically depend on the structural properties of OSCs as well as interfaces. Defect profiling has been carried out in single and multilayer OSC (heterojunction) films of p and n-type OSCs. Doppler broadening S-parameter revealed the presence of structural defects at the interface between p and n-type OSC (Fig. 11) due to the lattice mismatch between different OSCs. The study has also shown that positron mobility obtained in organic layers as calculated from fitted positron diffusion length is comparable to effective mobility of charge carrier measured from J–V characteristics and can be used to evaluate trap density as well as charge conductivity in organic layers [50]. Depth profiling study on annealed films has shown the presence of inhomogeneity in the nanostructure of the film after post deposition thermal annealing indicating the sensitivity and depth resolution of the technique for buried defects/structural disorder in OSC films [51]. We have also probed buried interfaces between OSC and dielectric substrate which are responsible for the conduction of charge carriers in OFETs. The study on OSC film grown on unmodified and self-assembled monolayer (SAM) modified dielectrics has shown the presence of more disorder at the interface in the former owing to the high surface roughness. Our studies on defect depth profiling in OSC thin films opens an avenue for non-destructive characterization of defect/disorder in actual organic devices.
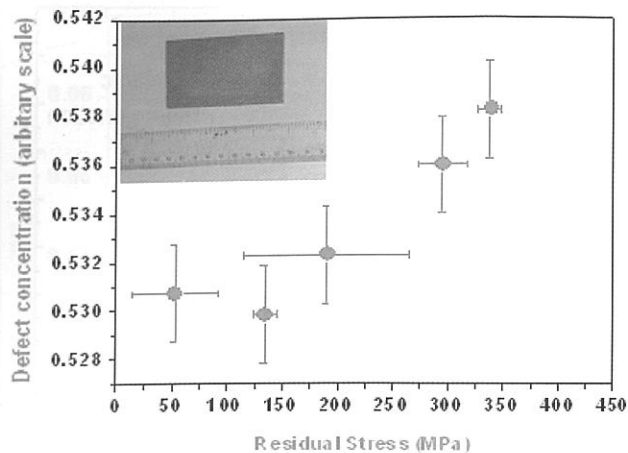
Fig. 12 Correlation between residual stress and defect concentration measured using PIPA facility at FOTIA in zircaloy plates (inset)

PIPA for Volumetric Assay of Defects in Large Engineering Samples

The energy of the positrons from isotopic sources is low making the implantation depths very small and hence the information derived corresponds to surfaces or shallow regions. This is a serious shortcoming for defect characterization of materials of industrial importance which are much thicker than the implantation depth of the positrons from isotope sources. Volumetric assay of defects produced at early stage of operation in engineering materials is important to predict the fatigue and failure of the material. In situ production of positrons in larger volume of samples has been achieved through pair production using the 4 MeV proton beam on fluorine target at FOTIA. The high energy gamma rays have high penetrability and produce positrons throughout the volume of the materials. The annihilation photons are then monitored to derive information on the defects present in the material.

Cold worked Zircaloy plates have been studied using PIPA and a nice correlation between the defect concentration and residual stress (measured using X-ray technique) has been obtained [Fig.12]. The results have also been corroborated by PALS measurements carried out using ELBE LINAC based GiPS facility (Dresden, Germany) [52]. The sensitivity of PIPA to regions of high defect concentration (strained region) in pipes used in ratcheting studies has also been demonstrated [Fig.13]. We have scanned a section of the pressure tube (PHWR) to investigate the imhomogeneity in defect profile (axial) following anomalous eddy current probe response. It was found that a particular section had lower defect concentration that coincides with the origin of anomalous eddy-current probe response. A detailed pulsed eddy-current probe study in the same section revealed higher conductivity consistent with decrease in the defect concentration observed from PIPA measurements.
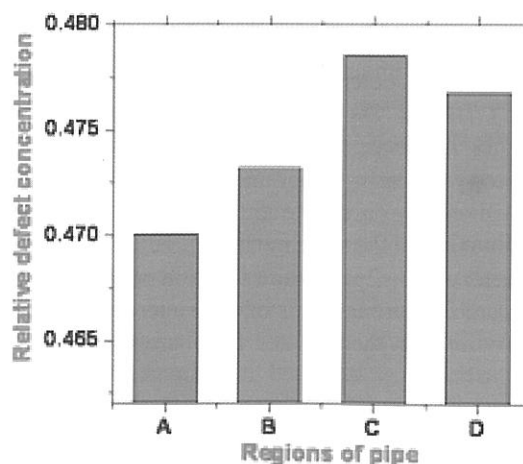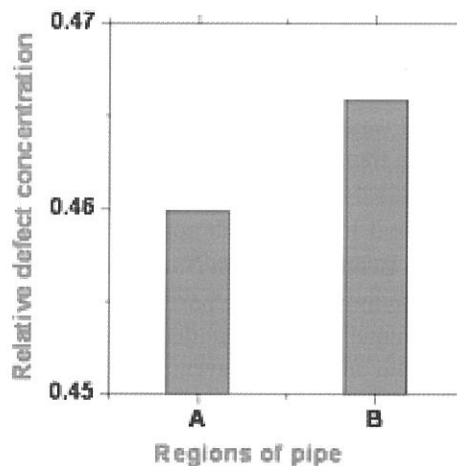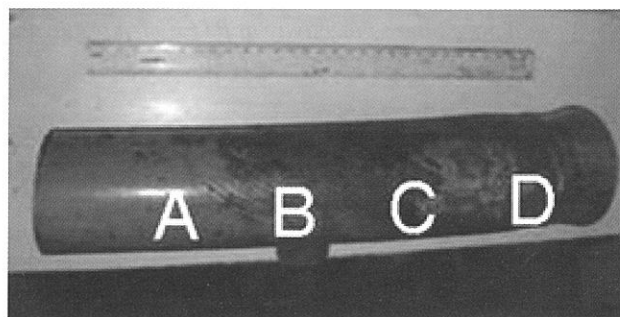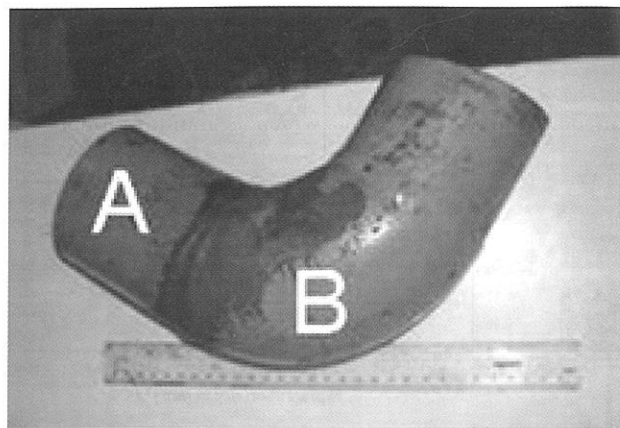

Fig. 13 The photographs of ratcheted pipe samples and relative defect concentrations in different regions of the pipe.(Sample courtesy: RSD, BARC)

Acknowledgements

References

[1] Schrader, D.M., and Jean, Y.C., (Ed) 1988. Positron and Positronium chemistry Elseivier, New York.

[2] Brandt W., and Dupasquier, A., (Eds.) 1981. Positron Solid State Physics: Proceedings of the International School of Physics "Enrico Fremi", Course LXXXIII, July 1981.

[3] Dupasquier, A., and Mills, Jr., A.P., (Ed), 1995. Positron Spectroscopy of Solids, Proc. Internat. School of Physics «Enrico Fermi», Course CXXV, Varenna 1993, IOS Press, Amsterdam.

[4] Jean, Y.C.; Mallon, P.E., and Schrader, D.M., (Eds.) 2003. Principles and Applications of Positron and Positronium Chemistry, World Scientific, London.

[5] Positron annihilation studies in MgB_2 superconductor, P.K. Pujari, K. Sudarshan, A. Goswami, S.B. Manohar, D.K. Aswal, A. Singh, S. Sen and S.K. Gupta, Phys. Rev. B 66(2002)012518.

[6] Positron annihilation spectroscopy in $YBa_2Cu_3O_{7-x}$. P.K. Pujari, S.B. Manohar, T. Datta, Satya Prakash, I.K. Gopalakrishnan, P.V.P.S.S. Sastry, G.M. Phatak and R.M. Iyer, Physica C 156(1988)769.

[7] Temperature dependence of positron annihilation parameters in $Bi_{2-x}Pb_xCa_2Sr_2Cu_3Oy$ and $Bi_2CaSr_2Cu_2O_y$ superconductors. P.K. Pujari, T. Datta, Udayan De and B. Ghosh, Phys. Rev. B 50(5)(1994)3438.

[8] Nature of superconducting transition in high Tc Tl-Ca-Ba-Cu-O compounds. P.K. Pujari, T. Datta, Satya Prakash, S.B. Manohar, I.K. Gopalakrishnan, G.M. Phatak, J.V. Yakhmi, P.V.P.S.S. Sastry and R.M. Iyer, Physica C 159 (1989)75.

[9] Positron annihilation studies of $Bi_2CaSr_2Cu_2O_x$ and $Bi_{1.6}Pb_{0.4}Ca_2Sr_2Cu_3O_y$ in the region of superconducting transition.P.K. Pujari, T.Datta, S.B. Manohar, Satya Prakash, P.V.P.S.S. Sastry, J.V. Yakhmi and R.M. Iyer, Solid State Commun. 73(9) (1990)623.

[10] Ddoppler broadened positron annihilation studies in Y-Ba-Cu-O, Tl-Ca-Ba-Cu-O and Bi(Pb)-Ca-Sr- Cu-O superconductors. P.K. Pujari, T. Datta, Satya Prakash, S.B. Manohar, I.K. Gopalakrishnan, G.M. Phatak, J.V. Yakhmi, P.V.P.S.S. Sastry and R.M. Iyer, Bull. Mat. Sci. 14(3)(1991)681.

[11] Positron annihilation studies on tetragonal $CaLaBaCu_3O_{6.85}$ superconductor, P.K. Pujari, R.A. Gunasekaran and J.V. Yakhmi, Phys. Lett. A 219 (1996)117.

[12] Probing the microstructure of Nafion-117 using positron annihilation spectroscopy, H. Sodaye, P.K. Pujari, A. Goswami and S.B. Manohar, J. Polym. Sci. Polym. Phys. B 35(5) (1997)771.

[13] Measurement of free-volume hole size distribution in Nafion-117 using positron annihilation spectroscopy, H. Sodaye, P.K. Pujari, A. Goswami and S.B. Manohar, J. Polym. Sci.: Polym. Phys. B36 (1998) 983.

[14] Temperature dependent positron annihilation studies in Nafion-117 membrane, H. Sodaye, P.K. Pujari, A. Goswami and S.B. Manohar, Rad. Phys. Chem. 58(2000)567.

[15] Positron annihilation studies on radiation-crosslinked Poly(N-isopropylacrylamide) hydrogel, A. Panda, H.S. Sodaye, R.N. Acharya, A. Goswami, P.K. Pujari, S. Sabharwal and S.B. Manohar, J. Polym. Sci: Polym. Chem. A 38(2000)3462.

[16] Positron annihilation studies of poly(N-isopropyl Acrylamide) gel in mixed solvents. A. Acharya, A. Goswami, P.K. Pujari, S. Sabharwal and S.B. Manohar, J. Polym. Sci.: Polym. Chem. A 40(2002)1028.

[17] Understanding the swelling of poly (N-isopropyl acrylamide) gels through the study of free volume hole size distributions using positron annihilation spectroscopy; P. N. Patil, K. Sudarshan, D. Dutta, P. K. Pujari, Polym. Bull. 65 (2010)577.

[18] Free volume and micro structural investigation of poly (ethylene terephthalate)-g-acrylic acid (PET-g-AA) co polymer films. S.K. Rath, M. Patri, S.K. Sharma, K. Sudarshan, P.K. Pujari. Rad. Phys. Chem. 79(2010)745.

[19] Positron annihilation spectroscopic studies of Fluorinated ethylene propylene copolymer-g-polystyrene, K. Sudarshan, S.K. Rath, M. Patri, A. Sachdeva and P.K. Pujari, Polymer 48(2007)6434.

[20] Free volume and microstructural investigation of poly ethylene tere phthalate –g-acrylic acid (PET-g-AA) copolymer films, S.K.Rath, M. Patri, S. K. Sharma, K. Sudarshan, P. K. Pujari, Rad. Phys. Chem. 79 (2010) 745.

[21] Free volumes and structural relaxations in diglycidyl ether of bisphenol-A based epoxy polyether amine networks, P. N. Patil, S. K. Rath, S. K. Sharma, K. Sudarshan, P. Maheshwari, M. Patri, S. Praveen, P. Khandelwal and P. K. Pujari, Soft Matter, 9 (2013) 3589.

[22] Modification of microstructure of the surface and in the bulk of ion irradiated membranes studied using positron annihilation spectroscopy, S. K. Sharma, P. Maheshwari, D. Dutta, K. Sudarshan and P. K. Pujari, Rad. Phys. Chem. 79, 2010, 1115.

[23] Effect on interfacial interaction on free volumes in phenol formaldehyde resin-carbon nanotube composites: positron annihilation lifetime and age momentum correlation studies, S. K. Sharma, J. Prakash, K. Sudarshan, P. Maheshwari, D. Sathiyamoorthy and P. K. Pujari, Phys. Chem. Chem. Phys. 14 (2012) 10972.

[24] Investigation of nanoscopic free volumes and interfacial interaction in epoxy resin/modified clay nanocomposite using positron annihilation spectroscopy, P. N. Patil, K. Sudarshan, S. K. Sharma, P. Maheshwari, S. K. Rath, M. Patri and P. K. Pujari, Chem. Phys. Chem. 13 (2012) 3916.

[25] Revealing the nanolevel molecular packing in chitosan-NiO nanocomposites using positron annihilation spectroscopy and small angle X-ray scattering, S. K. Sharma, J. Bahadur, P. N. Patil, P. Maheshwari, K. Sudarshan, S. Mazumder and P. K. Pujari, Chem. Phys. Chem., 14 (2013) 1055.

[26] Investigation of nanolevel molecular packing and its role in thermo-mechanical properties of PVA-MWCNTs nanocomposites: positron annihilation and small angle X-ray scattering studies, S. K. Sharma, J. Prakash, J. Bahadur, K. Sudarshan, P. Maheshwari, S. Mazumder and P. K. Pujari, Phys. Chem. Chem. Phys. 16 (2014) 1399.

[27] Positron annihilation studies in supported nickel carbo nate system, G.P. Babu and V. Manohar, K. Sudarshan, P.K. Pujari, S.B. Manohar and A. Goswami, J. Phys. Chem. B 106(2002)6902.

[28] Pore structure of silica gel: a comparative study through BET and PALS, D. Dutta, S. Chatterjee, K.T. Pillai, P.K. Pujari and B.N. Ganguly, Chem. Phys. 312(2005)319.

[29] Influence of 3γ-annihilation events on o-Ps lifetime and intensities in mesoporous materials, K. Sudarshan, S.K. Sharma, A. Goswami, P.K. Pujari, K.T. Pillai, Phys. Stat. Solidi C 6(11)(2009)2546.

[30] Air Quenching of Positronium in Mesoporous Materials: Positron Porosimetry, K. Sudarshan, D. Dutta, S.K. Sharma, A. Goswami and P.K. Pujari, J. Phys. Condensed Matter. 19(2007)386204.

[31] Unraveling the surface chemical characteristics and nanostructure of MgO/NiO catalyst using positronium probe: positron annihilation lifetime and age momentum correlation study, S. K. Sharma, K. Sudarshan and P. K. Pujari, RSC Advances, 4 (2014) 14733.

[32] Positron annihilation study of recrystallization behaviour in Zr2.5%Nb alloy, S. Mulki, P.K. Pujari, D. Srivastava, I. Samajdar, G.K. Dey, V.D. Hiwarkar and S. Sharma, Phys. Stat. Solidi C 6(2009)2352.

[33] Study on secondary phase precipitate behavior in Zircaloy-2 by positron annihilation spectroscopy, S. Mulki, P.K. Pujari, D. Srivastava, I. Samajdar, G.K. Dey, and S. Sharma, Phys. Stat. Solidi C 6 (2009)2370.

[34] Grain fragmentation and twinning in deformed Zircaloy 2: Response to positron lifetime measurements, S.K. Sahoo, V.D. Hiwarkar, K.V. Mani Krishna, I. Samajdar, P. Pant, P.K. Pujari, G.K. Dey, D. Srivastava, R. Tiwari, S. Banerjee, Materials Science and Engineering A 527(2010)1427.

[35] Probing the ordering transformation in $Cu_{69}Zn_{14}Al_{17}$ alloy with positron, P.K. Pujari, T. Datta, K. Madangopal and J. Singh, Phys. Rev. B47(18)(1993)11677.

[36] Evidence of zirconium nano-agglomeration in as-cast dilute U-Zr alloys Mukherjee S., Kaity S., Saify M.T., Jha S.K., Pujari P.K., J. Nuclear Mater. 452 (1-3)(2014)1.

[37] Positron annihilation studies in ZnO nanoparticles, S.K. Sharma, P.K. Pujari, and K. Sudarshan. D. Dutta, M. Mahapatra, S.V. Godbole, O.D. Jayakumar, A.K. Tyagi, Solid State Commun. 149(2009)550.

[38] Direct evidence of Cd vacancies in CdSe nanoparticles: Positron annihilation studies, S. K. Sharma, K. Sudarshan, P. Maheshwari, D. Dutta, P. K. Pujari, C. P. Shah , M. Kumar and P. N. Bajaj, Eur. Phys. J B, 82 (2011) 335.

[39] Probing phase evolution behavior during nano crystallization of metallic glass using positron annihilation spectroscopy, A.P. Srivastava, D. Srivastava, G.K. Dey, K. Sudarshan and P.K. Pujari, Metallurgical and Material Transaction 40(2009)1757.

[40] Positron annihilation spectroscopy of nanocrystallized Iron based metallic glass, A.P. Srivastva, M. Srinivas, S. Sharma, D. Srivstva, B. Mazumdar, P.K. Pujari, G.K. Dey and K.G. Suresh, Advanced Materials Research 67(2009)19.

[41] Understanding of microstructural evolution and soft magnetic properties in nanocrystallized metallic glass $Fe_{68.5}Cu_1Nb_3Si_{18.5}B_9$. A. P. Srivastava, D. Srivastava, S. K. Sharma,P. K. Pujari, K. G. Suresh and G. K. Dey, J. Nanoparticle Res. 15 (2013) 1-14.

[42] Correlation of soft magnetic properties with free volume and medium range ordering in metallic glasses probed by fluctuation microscopy and positron annihilation techniques, A. P. Srivastava, D. Srivastava, K. Sudarshan, S. K. Sharma, P. K. Pujari, K. G. Suresh and G. K. Dey, J. Mag. Mag. Mater. 324 (2012) 2476.

[43] Influence of free volume and medium range order on the deformation response of rapidly solidified and bulk Zr- based $(Zr_{52}Ti_{16}Al_{10}Cu_{18}Ni_{14})$ metallic glass, B. Vishwanath, S. K. Sharma, P. K. Pujari, R. Kishore, G. K. Dey and R. Tewari, Phil. Magazine 93 (2013) 3442.

[44] Positron annihilation studies on the phase transition of benzene and reactivity of nitrobenzene in confined framework of ZSM-5 zeolite, D. Dutta, A. Sachdeva, P.K. Pujari, Chem. Phys. Lett. 432(2006)116.

[45] Effect of confinement on the phase transition of benzene in nanoporous silica: A positron annihilation study, D. Dutta, P.K. Pujari, K. Sudarshan, and S.K. Sharma, J. Phys. Chem. C 112(2008)19055.

[46] Freezing of Nanodroplets: Phase Transition of Organic Liquids Confined in Nanopores Studied by Positron Annihilation Spectroscopy, D. Dutta, S.K. Sharma, P. Maheshwari, K. Sudarshan, P.K. Pujari, Mat. Sci. For. 607(2009)218.

[47] Effect of interfacial hydrogen bonding on the freezing/melting behavior of nanoconfined liquid, P. Maheshwari, D. Dutta, S.K. Sharma, K. Sudarshan, P.K. Pujari, M. Majumder, B. Pahari, B. Bandyopadhyay, K. Ghoshray, and A. Ghoshray, J. Phys. Chem. C 114(2010)4966.

[48] Phase Transition of Nanoconfined Water in Clay: Positron Annihilation, Nuclear Magnetic Resonance, and Dielectric Relaxation Studies, P Maheshwari, PK Pujari, SK Sharma, D Dutta, K Sudarshan, VS Mithu, P. K. Madhu, S. Deshpande, P. N. Patil, and N. Raje, The Journal of Physical Chemistry C 117 (27) (2013) 14313.

[49] Microstructural study of supported liquid membranes using slow positron beam, P.K. Pujari, P. Maheshwari, S.K. Sharma, D. Dutta, K. Sudarshan and A.V.R. Reddy, Phys. Stat. Solidi C 6(2009)2417.

[50] Defect profiling in organic semiconductor multilayers, P Maheshwari, PK Pujari, SK Sharma, K Sudarshan, D Dutta, S Samanta, A Singh, D K Aswal, R Ajay Kumar and I Samajdar, Organic Electronics 13 (8) (2012) 1409.

[51] Probing inhomogeneities in nanoscale organic semiconductor films: Depth profiling using slow positron beam and X-ray reflectivity techniques Priya Maheshwari, D. Bhattacharya, S.K. Sharma, S. Mukherjee, S. Samanta, S. Basu, D.K. Aswal, P.K. Pujari, Solid State Communications (2014) doi.org/10.1016/j.ssc.2014.09.001i

[52] Photon induced positron annihilation spectroscopy: A nondestructive method for assay of defects in large engineering samples, P. K. Pujari, K. Sudarshan, R. Tripathi, D. Dutta, P. Maheshwari, S. K. Sharma, D. Srivastava, R. Krause-Rehberg, M. Butterling, W. Anwand and A. Wagner, Nucl. Instr. Meth. Phys. Res. B 270 (2012) 128.

Dr. P.K. Pujari, *a post-graduate in Chemistry from IIT, Delhi joined the Radiochemistry Division, BARC after completing the 28th batch of BARC Training School and bagging the Homi Bhabha Prize as topper of the Chemistry Discipline in 1985. He has been specialising in positron annihilation spectroscopy and its applications. He has developed a state of the art positron laboratory at BARC. Currently he is the Head of the Nuclear Chemistry Section of Radiochemistry Division and Professor at the Homi Bhabha National Institute. Dr. Pujari is the recipient of several awards: Dr. Tarun Data Memorial Young Scientist Award of IANCAS (1997); DAE-SRC Outstanding Research Investigator Award (2008); DAE Homi Bhabha Science and Technology Award (2008). Presently he is the Chairman of the International Scientific Committee on Positron and Positronium Chemistry.*

For Limited Circulation Only